Structural studies and characterisation of Kir7.1 and its role in retinal disease

STRUCTURAL STUDIES AND CHARACTERISATION OF KIR7.1 AND ITS ROLE IN RETINAL DISEASE

Thesis submitted to **Birkbeck, University of London,**
for the degree of **Doctor of Philosophy**, 2023

Niamh O'Malley
Birkbeck, University of London

Declaration of originality

Initial protein expression in HEK293 cells was conducted by Belinda Faust and Ashton Churchill. Protein stability detergent screening was carried out by Belinda Faust. Initial cryo-EM grid preparation and collection of high-resolution cryo-EM data was performed by Natasha Lukyanova. Cryo-EM grid preparation for screening was at times conducted by Chady Nasrallah.

The work presented in this thesis is my own. When information has been derived from other sources, I confirm that this has been indicated in the text.

Niamh O'Malley, 2023.

Acknowledgements

There are several people that I would like to thank for their support and advice throughout my PhD. Firstly, I would like to thank my supervisor Bonnie Wallace for her unwavering support and dedication throughout these four years. She was always available and willing to offer guidance and motivation when it was needed, and I feel lucky to have been one of her students.
I would also like to thank my industrial supervisors Belinda Faust and Chady Nasrallah (Vertex Pharmaceuticals). They both went above and beyond to help, teach, and guide me. They were always there for support, both scientific and moral.

In the Wallace group, I would like to thank Fran and Dave for their scientific discussions, interesting conversations, and funny moments. In tough times they were always there to make me laugh or listen to my worries.
I would like to express my gratitude to Natasha, Shu, Dave, and Claire for their training and technical support. Their expertise, encouragement and willingness to help was imperative to the success of my work and contributed to making Birkbeck a special place to undertake a PhD.

I would like to thank the BBSRC and Vertex for funding my research and LIDo for organising a wonderful doctoral training programme. LIDo provided me with a cohort of PhD students that have become some of my closest friends and have kept me sane and happy throughout these four years. In particular, I thank Laurel and Becky for consistently listening to my struggles, empathising, offering advice and ultimately making me laugh.

Finally, I need to thank my family whose support has never wavered even when they didn't understand what I was saying. You have always believed in me, and you have been there every time I needed you.
And lastly, to my wonderful partner Bill, thank you for everything. This thesis is fuelled by your incredible cooking and was made possible by your constant love and understanding.

Abstract

Inward rectifying potassium channel 7.1 (Kir7.1) is a vital ion channel involved in maintaining cellular homeostasis and electrical signalling across various tissues and organs. Dysfunctions in Kir7.1 have been linked to rare retinal diseases, including Snowflake Vitreoretinal Degeneration (SVD) and Leber Congenital Amaurosis. Here, we resolved three cryo-EM structures of Kir7.1 that elucidate channel activation and how a R162W mutation contributes to SVD. While PIP_2 is known to activate all human Kir channels by inducing conformational changes, the observed structures of Kir7.1 did not exhibit docking of the cytoplasmic domain as seen in other Kir channels. However, upon PIP_2 binding to Kir7.1, the helix bundle crossing widens producing an open channel pore. The opening of the channel without docking of the cytoplasmic domain represents a novel mechanism for Kir channel activation. Cryo-EM analysis of the R162W mutation, responsible for SVD, revealed a structure with a more constricted pore compared to the wild type structure. The presence of the tryptophan residue at position 162 appears to impede potassium ion flow, contributing to the loss of Kir7.1 function and the pathology of SVD, providing a possible mechanism for the basis of the disease. By providing detailed insights into Kir7.1's overall architecture, channel gating, and involvement in retinal diseases, this thesis significantly contributes to our understanding of Kir7.1's structure-function relationship and regulatory mechanisms.

Table of Contents

List of Figures

List of Tables

List of Abbreviations

α-MSH: α-melanocyte stimulating hormone

3D: Three-dimensional

Å: Angstrom

AgRP: Agouti-related peptide

APA: Aldosterone-producing adenoma

ATP: Adenosine triphosphate

ATS: Andersen-Tawil syndrome

Au: Gold

Ba^{2+}: Barium ions

BS: Bartter's syndrome

C8-PIP_2: Octanoyl-phosphatidylinositol 4,5-bisphosphate

CCDs: Charge-coupled devices

CF: Carbon film

CHO: Chinese hamster ovary

CHS: Cholesteryl hemisuccinate

Cryo-EM: Cryogenic electron microscopy

CTD: Cytoplasmic domain

CTF: Contrast transfer function

Cy5: Cymal-5

Cy7: Cymal-7

DDM: N-dodecyl β-D-maltoside

DEDs: Direct electron detectors

DEND: Developmental delay, epilepsy, and neonatal diabetes

DM: N-Decyl β-D-Maltopyranoside

DNA: Deoxyribonucleic acid

DQE: Detective quantum efficiency

EAST: Epilepsy, ataxia, sensorineural deafness, tubulopathy

ECL: Enhanced chemiluminescence

EDTA: Ethylenediaminetetraacetic acid

eV: Electron volts

FC12: Foscholine12

FEG: Field emission gun

FHH: Familial hyper insulinemic hypoglycaemia

FSC: Fourier shell correlation

FT: Flow-through

G-proteins: GTP binding proteins

GDN: Glyco-diosgenin

GFP: Green fluorescent protein

GIRK: G-protein regulated Kir channel

GnTI: N-acetylglucosaminyltransferase I

GO: Graphene oxide

GPCR: G-protein coupled receptors

GSFSC: Gold-standard Fourier shell correlation

GUI: Graphical user interface

Gβγ: G-protein βγ

HBC: Helix bundle crossing

HEK293: Human embryonic kidney 293

Hsp70: Heat shock protein 70

IH: Interfacial helix

IMZ: Imidazole

iPSC: Induced pluripotent stem cells

IPTG: Isopropyl ß-D-1-thiogalactopyranoside

K^+: Potassium

K_{ATP}: ATP-sensitive potassium channel

KCl: Potassium chloride

Kir: Inward rectifying potassium channels

KPLBS: Keppen-Lubinsky syndrome

Kv: Voltage-gated potassium channels

LB: Luria-Bertani

LCA: Leber congenital amaurosis

LMNG: Lauryl Maltose Neopentyl Glycol

LQT13: Long WT syndrome type 13

M1: Transmembrane spanning helix 1

M2: Transmembrane spanning helix 2

MC4R: Melanocortin-4 receptor

MD: Molecular dynamics

mRNA: Messenger ribonucleic acid

MS: Mass spectrometry

Na^+: Sodium ions

NanoDSF: Nanoscale differential scanning fluorimetry

NDM: N-dodecyl-β-d-maltoside

Ni-NTA: Nickel-nitrilotriacetic acid

NMD: Nonsense-mediated mRNA decay

NMR: Nuclear magnetic resonance

NS: Negative staining

O/N: Overnight

OGNG: Octyl Glucose Neopentyl Glycol

OXTR: Oxytocin receptor

P-loop: Pore loop

PH: Pore helix

PIP_2: Phosphatidylinositol 4,5-biphosphate

PNDM: Permanent neonatal diabetes mellitus

POSs: Photoreceptor outer segments

PrDOS: Protein DisOrder prediction

PVN: Paraventricular nucleus of the hypothalamus

ROMK: Kir1.1

RPE: Retinal pigment epithelium

rRNA: Ribosomal-RNA

SDS-PAGE: Sodium dodecyl-sulfate polyacrylamide gel electrophoresis

SEC: Size exclusion chromatography

SeSAME: Seizures, sensorineural deafness, ataxia, mental retardation, and electrolyte imbalance

SF: Selectivity filter

SVD: Snowflake vitreoretinal degeneration

SNR: Signal-to-noise ratio

SPP: Sporadic periodic paralysis

SQT3: Short WT syndrome type 3

SUR: Sulfonylurea receptor

Ta: Recommended annealing temperature

TAE: Tris acetate EDTA

TAL: Thick ascending limb

TBST: Tris buffered saline + 0.1% Tween 20

TDM: N-Tridecyl-Beta-Maltoside

TEM: Transmission electron microscope

TEV: Tobacco Etch virus

Tm: Melting temperature

TMD: Transmembrane domain

TNDM: Transient neonatal diabetes mellitus

TPP: Thyrotoxic periodic paralysis

UV: Ultraviolet

WB: Western blot

WT: Wild type

ΔTm: Change in melting temperature

Chapter 1

1. Introduction

1.1 Potassium channels

Potassium channels are the key proteins in controlling potassium ion concentration across the cell membrane. They do this by mediating the flow of potassium (K^+) ions into and out of the cell. This process allows the alteration of the membrane potential and cell excitation. This conduction of potassium is central to many cellular processes, such as secretion of hormones and the formation of electrical impulses (MacKinnon, 2003).

To achieve specific conduction of potassium ions, all K^+ channels share important characteristics, including a water-filled permeation pathway, a selectivity filter containing the TVGYG signature sequence and a gating mechanism. The permeation pathway (the pore) facilitates K^+ crossing the membrane. The selectivity filter is responsible for potassium ion selectivity and a gating mechanism allows switching between the open and closed states (Hille, 1992). Initially, the classification of potassium channels into families was based on the primary amino acid sequence of the pore region only. This method of classification resulted in three main groups containing, six, four and two-transmembrane domains (Shieh et al., 2000). These can be further described as the voltage-gated potassium (Kv) channels with six transmembrane spanning domains and a single pore, inward rectifying potassium channels which contain two transmembrane spanning regions and one pore and also two-pore K^+ channels that consist of four transmembrane domains with two pore regions (Shieh et al., 2000). **Fig. 1.1** represents the difference in structure between the subunits for voltage-gated and inward rectifying potassium channels, but it also highlights the highly conserved similar transmembrane region.

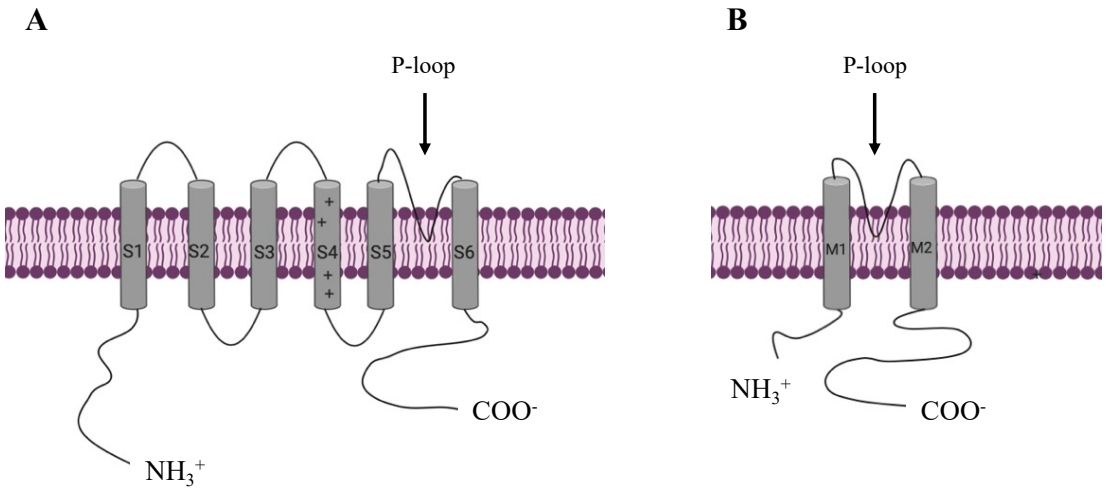

Figure 1.1. Schematic representation of two classes of potassium channels. **A.** A voltage-gated potassium channel single subunit. Six transmembrane domains are denoted as S1-S6 with S4 highlighted as the voltage sensor domain. The pore loop (P-loop) region is identifiable between S5 and S6 as a small loop protruding into the membrane. **B.** A subunit of an inward rectifying potassium channel with only two transmembrane domains known as M1 and M2. These domains are structurally similar to S5 and S6 of the voltage-gated channels with the pore loop structure between them being highly conserved.

1.1.1 History of potassium channel research

Initial work investigating potassium channels was conducted in 1987, on the Shaker K^+ channel gene from *Drosophila melanogaster,* which revealed the first amino acid sequence of a K^+ channel (Tempel et al., 1987). MacKinnon et al. (1989) used charybdotoxin binding and site-directed mutagenesis to identify the amino acids present in the pore region of the Shaker channel (MacKinnon and Miller, 1989). Further work carried out by MacKinnon contributed significant discoveries to the field of potassium channel research, including identifying the pore loop region and highlighting the signature TXXTXGYG sequence present in the selectivity filter (MacKinnon, 1995). Inspired by these advancements, MacKinnon focused on solving the first crystal structure of a potassium channel, concentrating on a bacterial channel named KcsA from *Streptomyces lividans* consisting of two transmembrane spanning domains. By removing the disordered C-terminus of KcsA, MacKinnon

successfully solved the first crystal structure of a potassium channel at 3.2 Å resolution (**Fig. 1.2**) (Doyle et al., 1998). This structure began the journey into potassium channels that won Robert MacKinnon the Nobel Prize in Chemistry in 2003.

1.1.2 General structure and properties of the ion pore and selectivity filter

The transmembrane-spanning subunits (**Fig. 1.1**) form a tetramer that encircles the central ion conduction pathway (Zhou et al., 2001). As S5 and S6 of the voltage-gated potassium channels and M1 and M2 from the inward rectifying potassium channels hold a similar structure, the ion conduction pore will be described concerning two transmembrane domains and the conserved P-loop, which is common in both. These two transmembrane α-helices can be referred to as the inner and outer helices, with the inner helix being nearest the ion pathway and the outer helix nearer the membrane. The P-loop is a tilted pore helix which exists partway through the membrane facing its negative C-terminus towards the ion pathway (MacKinnon, 2003). Halfway through the membrane, a central cavity of water is found with a diameter of almost 10 Å (Doyle et al., 1998). The pointing of the negatively charged end of the titled pore helix towards the central cavity aids the stabilisation of the positively charged potassium ions in the central cavity.

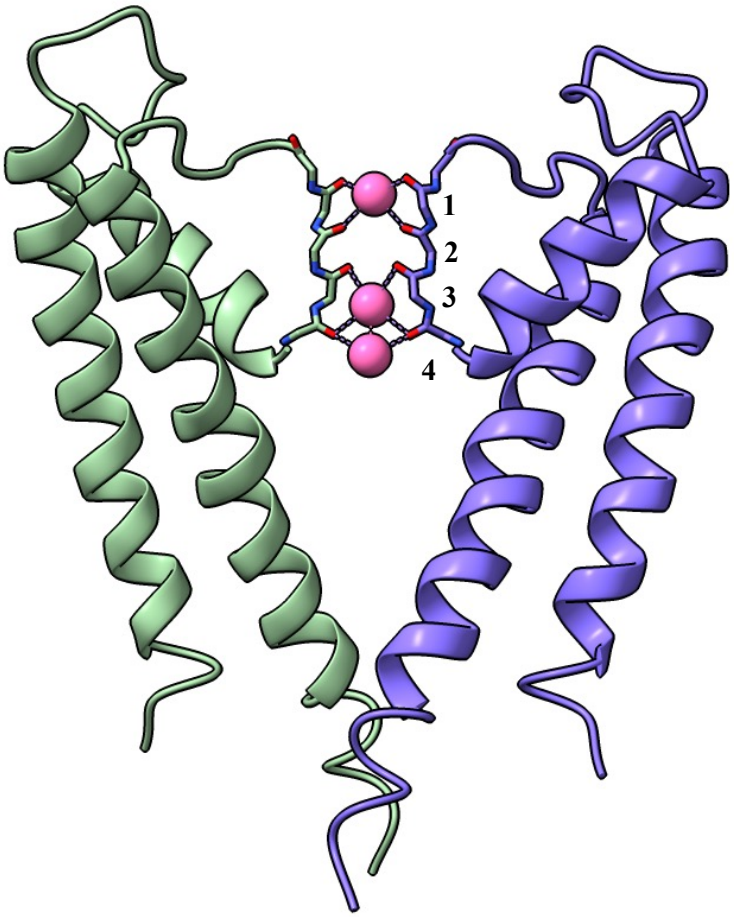

Figure 1.2. KcsA crystal structure. Two monomers from the KcsA structure (PDB: 1BL8) showcasing the ion conduction pore and selectivity filter. Only two of the four subunits are shown to allow interpretation, with the extracellular surface at the top. Potassium ions are represented by pink spheres. Binding sites are number 1-4 beginning on the extracellular side. Figure adapted from Doyle et al. (1998).

A hydrated potassium ion has a radius of 3.15 Å and can travel through most of the ion conduction pathway remaining hydrated. However, it is the selectivity filter that is so narrow that potassium ions must lose their water molecules in order to pass through (Doyle et al., 1998). This signature sequence creates four layers of carbonyl oxygen atoms and a single layer of threonine hydroxyl oxygen atoms which forms four sites for K^+ binding (MacKinnon, 2003). It is possible to number these sites 1-4 beginning at the extracellular side of the channel (**Fig. 1.2**). Binding to these sites requires dehydration of the potassium ions, which is mediated by the presence of eight oxygen atoms, four above and four below, two from each subunit. This

interaction is similar to what is observed in the central cavity when the K^+ ions are hydrated. The presence of the oxygen atoms in the selectivity filter compensates for the dehydration necessary for the potassium ion to enter and permits high conduction rates.

Having appreciated the intricate method of high selectivity in potassium channels, it is worth realising that this does not hinder the conduction rates. One aspect to consider is the fact that K^+ channels form multi-ion pores (4 binding sites), therefore, there is repulsion between adjacent ions which reduces the affinity of each ion for the binding site (Roux and MacKinnon, 1999; Zhou et al., 2001). Even though there are four potential binding sites for K^+ ions (**Fig. 1.2**), usually only two sites are occupied at any time and they can be found in two possible configurations; consisting of binding site 1 and 3 or binding site 2 and 4 being occupied (Roux and MacKinnon, 1999). When either configuration is adopted, the K^+ ions are separated by a water molecule. A configuration cycle has been proposed by Roux et al. (1999) that represents an ion successfully crossing the selectivity filter: as an ion enters the filter from one side, an ion leaves the filter on the other side and therefore configurations alter from 1,3 to 2,4. The actual direction of the ion entering and leaving the filter depends on both the electrochemical gradient and the type of K^+ channel. This idea of K^+ selectivity has been deduced from crystallographic experiments and reinforces the mechanism proposed by Hodgkin and Keynes in 1955; that ion conduction occurs in a single-file movement of several ions across the membrane (Hodgkin and Keynes, 1955).

Interestingly, the essential structure of the selectivity filter relies heavily on the presence of K^+ ions (Zhou et al., 2001). This binding mechanism requires two K^+ ions in the selectivity filter and experiments have demonstrated that a reduction in K^+ concentration, to below intracellular levels, resulting in a single potassium ion in the selectivity filter induces a significant conformational change (Zhou et al., 2001). The addition of a second ion into the selectivity filter is what causes the necessary change in the structure to allow the passage of ions. Therefore, it has been concluded that the energy from ion binding contributes to changing the selectivity filter structure and so a weakened binding of the ion occurs (Zhou et al., 2001). This reduction in binding affinity is pivotal for high conduction rates and could not happen without the

conformation change caused by the entrance of a second K^+ ion into the filter (MacKinnon, 2003).

1.2 Inward rectifying potassium channels

Inward rectifying K^+ (Kir) channels are one of the most prominent ion channel families found in mammalian cells. The 15 members of the Kir family of potassium channels can be further divided into seven subfamilies and these subfamilies share common molecular architecture but differ by means of regulation. Members are annotated Kirx.y where 'x' represents the subfamily and 'y' shows the subtype within the subfamily (Doupnik et al., 1995). Kir channels form tetramers of either four identical subunits (homotetrameric) or related subunits (heterotetrameric) with each subunit consisting of two transmembrane domains connected by the P-loop (**Fig. 1.1**). An additional feature of Kir channels is the formation of a cytoplasmic pore, which extends the ion conduction pathway from the selectivity filter through this large cytoplasmic pore and into the cell. It is thought that this cytoplasmic pore contains an additional gating mechanism, referred to as the G-loop. Therefore, potassium ions must pass through two gating regions to successfully enter the cell.

Functionally, the seven Kir channel subfamilies may be organised into four categories: 1 - classical Kir channels (Kir2.x), better known as 'strong rectifiers' and play a role in shaping the initial depolarisation and final repolarisation of the action potential; 2 - G protein-activated Kir channels (Kir3.x), found forming macro-complexes with G-protein coupled receptors (GPCR), and are activated by the binding of the G-protein βγ (Gβγ) subunits (Kano et al., 2019); 3 - ATP-sensitive Kir channels (Kir6.x), negatively regulated by ATP binding and are activated through the sulfonylurea receptor (SUR1, SUR2A, and SUR2B) with which it forms octameric complexes (Martin et al., 2017; Zhao and MacKinnon, 2021) and 4 - K^+ transport channels (Kir1.x, Kir4.x, Kir5.x and Kir7.x), with moderate to weak rectification and often responsible for maintaining the resting membrane potential (**Table 1.1**) (O'Donnell et al., 2017; Pattnaik et al., 2015).

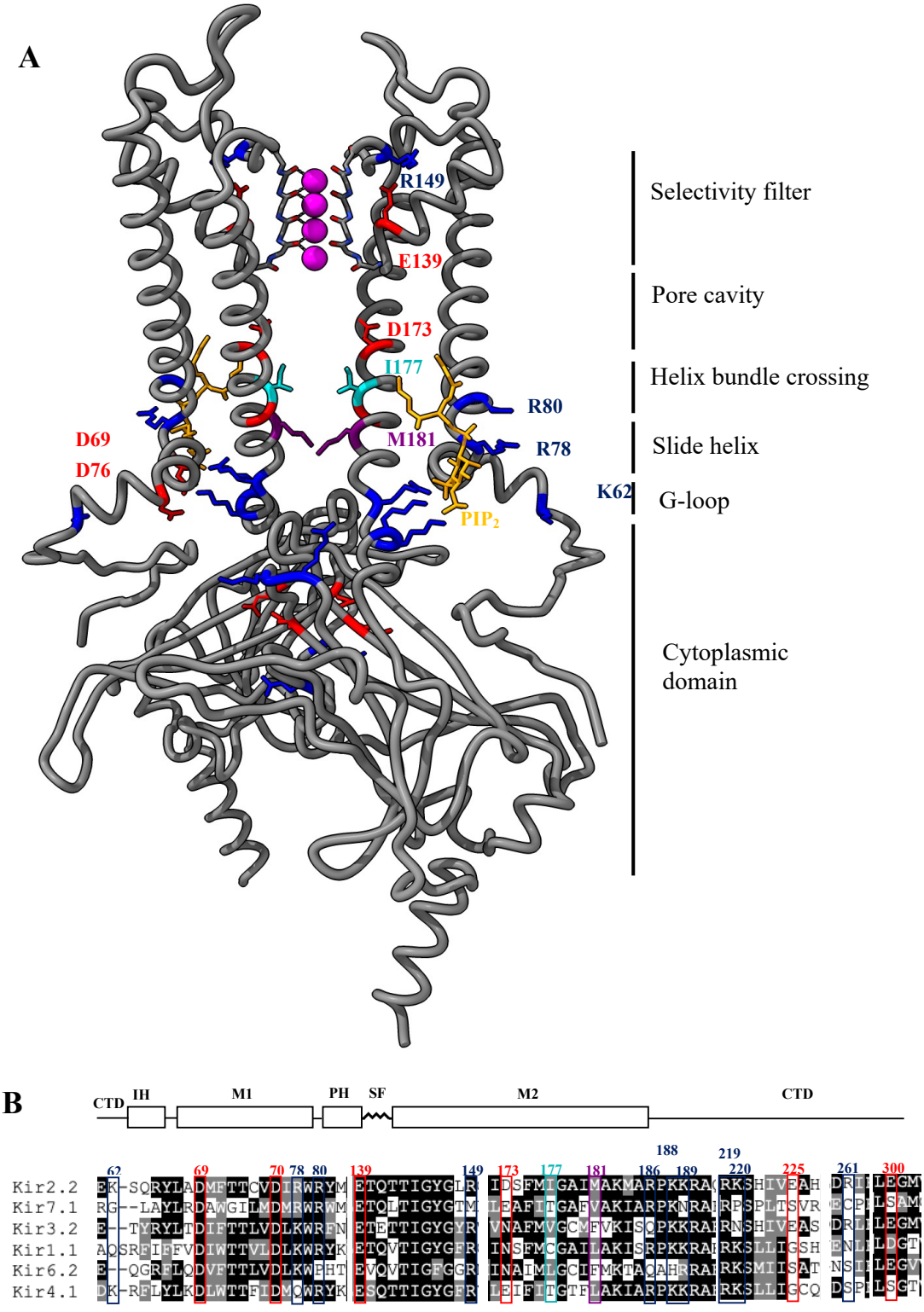

Figure 1.3. Key structural features of Kir channels. A. Two subunits of Kir2.2 crystal structure (PDB: 3SPI). Side chains that are involved in the inner helix bundle crossing, rectification, or lipid-binding are represented as sticks and are labelled. PIP_2 molecules bound to the channel are shown in orange. Selectivity filter residues are displayed as sticks, with potassium ions bound and coloured magenta. **B.**

Sequence alignment of key functional regions in Kir channels. Key residues, known to be involved in gating and/or rectification, are coloured red, cyan, or blue. Schematic representation of one Kir subunit is aligned above the sequences. Figure adapted from (Jogini et al., 2022). Abbreviations: *CTD* Cytoplasmic domain, *IH* interfacial helix, *M1* transmembrane spanning helix 1, *PH* pore helix, *SF* selectivity filter, *M2* transmembrane spanning helix 2.

1.3 Gating and modulation of inward rectifying potassium channels

1.3.1 PIP_2

All Kir channels are comprised of a transmembrane domain (TMD) and a cytoplasmic domain (CTD). The distance between these two domains is determined by the swing of the CTD towards the TMD, described as docking or bending. This is a structural change thought to be involved in the activation of Kir channels and the transition to a conductive state (Hansen et al., 2011; Niu et al., 2020). The open state of Kir channels is modulated by several molecules, ligands, and ions at sites throughout the CTD and TMD. One universal regulator of human Kir channels is the membrane-bound phospholipid phosphatidylinositol 4,5-biphosphate (PIP_2). PIP_2 has a net negative charge caused by three phosphates in the head group, and therefore binds to regions with several positively charged residues. Kir channels possess a conserved PIP_2 binding motif comprised of sites located in the N-terminus and regions of the TMD/CTD (**Fig. 1.4**). The structural representation of this binding site can be observed in the Kir2.2 structures with and without a short-chain (dioctanoyl) PIP_2 derivative present (**Fig. 1.4**). PIP_2 is identified in the binding region between the TMD and CTD and is thought to trap the channel in a conformation that facilitates the opening of the inner helix bundle and G-loop. When PIP_2 is present and bound, docking of the CTD to the TMD is observed. Whereas, without PIP_2 no docking and a more extended channel exists (**Fig. 1.4**). This docking is structurally observed in Kir3.2 (GIRK2), Kir3.4 (GIRK4), Kir6.2 and Kir2.2 channels (Hansen et al., 2011; Niu et al., 2020).

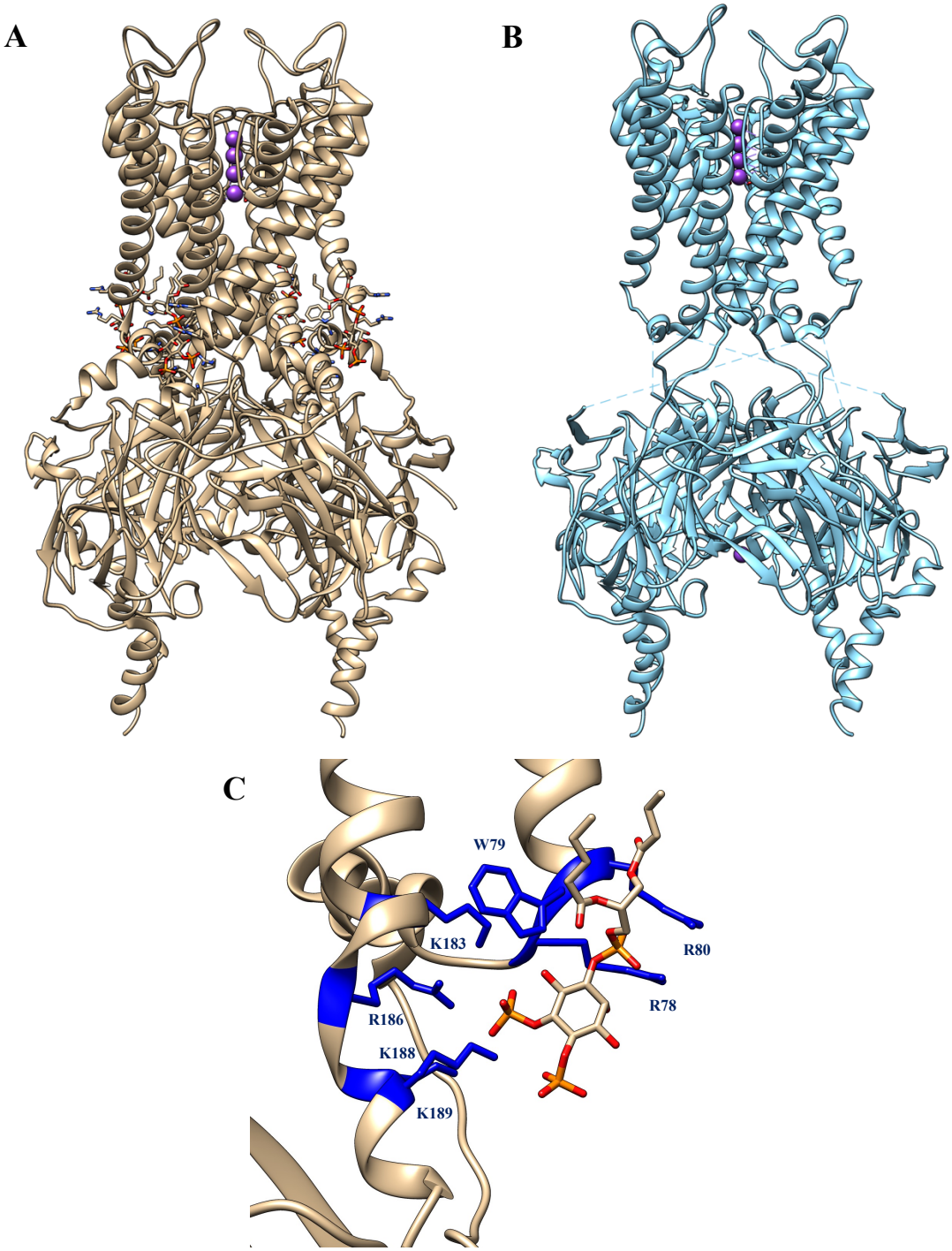
A
B
C
W79
K183
R80
R78
R186
K188
K189
D
79
78
80
188
183
186
189
Kir2.2
Kir7.1
Kir3.2
Kir1.1
Kir6.2
Kir4.1

Figure 1.4. Crystal structure of Kir2.2 with and without PIP_2. A. Kir2.2 channel structure (PDB: 3SPI) complexed with PIP_2. One PIP_2 molecule is bound to each subunit of Kir2.2. PIP_2 is coloured by atom type and is bound at the interface between the TMD and the CTD. **B.** Kir2.2 channel structure (PDB:3JYC) in the absence of PIP_2. Channel adopts an extended conformation. **C.** Close up view of the PIP_2 binding site and the Kir2.2 residues that are interacting with the lipid. Side chains of interacting residues are shown in blue. **D.** Sequence alignment of Kir channels from different subfamilies showing conserved PIP_2 binding residues in blue. Residues are number according to Kir2.2.

1.3.2 G-loop and helix bundle crossing

The presence of an activation gate and its role in ion conduction has been a complex and controversial topic in Kir channel research. PIP_2 activation is found in all human Kir channels but other means of regulation vary amongst channels, from pH and ATP sensitivity to G-protein regulation. There are two regions of interest in Kir channels that are implicated in gating: the G-loop and the helix bundle crossing (**Fig. 1.3**). A chimeric bacterial/mammalian Kir3.1 channel was reconstituted into planar lipid bilayers and shown to behave as a typical Kir channel, requiring PIP_2 for activation (Leal-Pinto et al., 2010; Nishida et al., 2007). The structure of this channel was solved with the G-loop in two states, dilated and constricted. Molecular dynamics (MD) simulations demonstrated PIP_2 mediating the opening of this G-loop gate but the helix bundle crossing remaining closed, suggesting the channel did not fully open (Meng et al., 2012). A conserved glycine residue in M2 is implicated in channel gating by providing flexibility to the helix (Jin et al., 2002). Substituting the following residue with a proline in Kir3.x (GIRK) channels resulted in a constitutively active channel (Sadja et al., 2001). MD simulations used proline mutant chimera structures to create ‘open’ channels and demonstrated the transition from the closed to the open state of the helix bundle crossing gate (Meng et al., 2016). This work sheds light on the mechanistic opening and closing of the helix bundle crossing in relation to PIP_2 binding. The proline mutation increased the bending of the M2 helices in all structures, but only the structure with PIP_2 also bound achieved helix bundle crossing opening (Meng et al., 2016).

Conversely, MD simulations carried out on the Kirbac3.1 structure demonstrated that potassium ion conduction was not impeded by the constriction at the helix bundle crossing (Black et al., 2020). This suggests that the helix bundle crossing does not need to dilate or widen for potassium conduction to occur. Potassium ions must transiently lose water from its hydration shell and pass through the constricted site (Black et al., 2020). In Kirbac3.1 there is a tyrosine residue at position 132 that forms a constriction at the bottom of the M2 helices. MD simulations showed K^+ ions passing through this tyrosine collar in a partially hydrated state (Black et al., 2020). However, Kirbac3.1 is a prokaryotic potassium channel and therefore, this leaves questions to be answered about how exactly human Kir channels are gated and whether the helix bundle crossing plays a role in this gating process or not.

1.4 Summary of Kir channels and associated channelopathies

Malfunctions in ion channels, due to mutations in genes encoding the proteins, have been connected to a number of growing diseases, known as channelopathies. The Kir channel family serve diverse and important roles in the body and are therefore implicated in several diseases (**Table 1.1**). It is also conceivable that additional clinical conditions will be revealed in the future due to dysfunctions in one or several members of this family. A comprehensive understanding of the disease mechanisms is necessary for accurate diagnosis, therapeutic strategy, and drug development.

Sub family	Gene	Channel/ name	Main tissue	Function	Disease	Functional group
Kir1.x	*KCNJ 1*	Kir1.1/ ROMK	Kidney	K^+ Secretion	BS, type II	K^+ transport channels
Kir4.x	*KCNJ 10*	Kir4.1	Brain	K^+ Secretion in neurons/main tenance of basolateral membrane	SeSAME (EAST)	
	KCNJ 15	Kir4.2	Retina Cochlea Kidney			

				potential in renal tubules		
Kir5.x	*KCNJ 16*	Kir5.1	Kidney	Heterotetramises with Kir4.x and maintains resting membrane potential		
Kir7.x	*KCNJ 13*	Kir7.1	Retina Kidney Brain Uterine muscle	K^+ Secretion	SVD, LCA	
Kir2.x	*KCNJ 2*	Kir2.1/ IRK1	Brain Heart Smooth and skeletal muscles	Maintenance of membrane potential and K^+ homeostasis	ATS, TPP/SPP LQT7 SQT3, Atrial fibrillation	Classical K^+ channels
	KCNJ 12	Kir2.2/ IRK2				
	KCNJ 4	Kir2.3/ IRK3	Brain Heart			
	KCNJ 14	Kir2.4/ IRK4	Brain			
	KCNJ 18	Kir2.6/ IRK6	Skeletal muscles		TPP/SPP	
Kir3.x	*KCNJ 3*	Kir3.1/ GIRK1	Brain Heart	Regulating electrical activity		G-protein gated K^+ channels
	KCNJ 6	Kir3.2/ GIRK2	Thyroid		KPLBS	

	KCNJ 9	Kir3.3/ GIRK3	Pancreas			
	KCNJ 5	Kir3.4/ GIRK4	Adrenal gland		APA, LQT13	
Kir6.x	*KCNJ 8*	Kir6.1	Pancreas Heart Smooth muscles Neurons	Regulating electrical activity	DEND PNDM TNDM FHH	ATP-sensitive K^+ channels
	KCNJ 11	Kir6.2				

Table 1.1. Classification of Kir channels by phylogeny and functionality. Summary of all known human Kir channels, their expression locations, functions, and associated diseases. Table adapted from Cheng et al. (2015).

Disease abbreviations: APA aldosterone-producing adenoma, *ATS* Andersen-Tawil syndrome, *BS* Bartter's syndrome, *DEND* Developmental delay, epilepsy, and neonatal diabetes, *EAST* Epilepsy, ataxia, sensorineural deafness, tubulopathy, *FHH* Familial hyper insulinemic hypoglycaemia, *KPLBS* Keppen-Lubinsky syndrome, *LCA* Leber congenital amaurosis, *LQT13* Long QT syndrome type 13, *SQT3* Short QT syndrome type 3, *PNDM* Permanent neonatal diabetes mellitus, *SPP* Sporadic periodic paralysis, *SeSAME* Seizures, Sensorineural deafness, Ataxia, Mental retardation, and Electrolyte imbalance, *SVD* Snowflake vitreoretinal degeneration, *TNDM* Transient neonatal diabetes mellitus, *TPP* Thyrotoxic periodic paralysis.

1.4.1 Kir1.x

Kir1.1/ROMK was the original Kir channel cloned and is principally expressed in the kidney (Ho et al., 1993). ROMK plays a vital role in regulation of salt and potassium homeostasis. Different isoforms of ROMK are expressed along the thick ascending limb (TAL) and distal nephron, where they form apical, weak Kir channels (Welling and Ho, 2009). Bartter's syndrome is a disease in which the kidneys cannot reabsorb sodium and chloride in the TAL of the loop of Henle. Type II of Bartter's syndrome is caused by mutations in ROMK that result in inactivation of the channel. Over 35 different mutations have been identified in ROMK, with some introducing nonsense codons or frameshifts resulting in truncated proteins with loss of function consequences. Over half of the missense mutations reduce or eliminate surface expression, likely caused by insufficient folding or trafficking of

ROMK (Peters et al., 2003). Whereas other mutations alter the opening of the channel by disrupting regulatory pathways, such as, phosphorylation or PIP_2 binding.

1.4.2 Kir2.x

Kir2 channels are constitutively active and have a strong inward K^+ rectification that is required for establishing a stable, negative resting membrane potential in excitable cell types (de Boer et al., 2010). Blockage of the channel with polyamines at positive membrane potentials prevents potassium efflux, thus delaying new action potential firing and ensuring appropriate QT interval (Hager et al., 2022). This is a key role in excitable cells, which means, defective Kir2 channels have damaging results. Mutations impairing Kir2.1 trafficking to the membrane causes Andersen-Tawil syndrome (ATS) which is described by periodic paralysis, repolarisation changes in electrocardiograms, and developmental abnormalities (Pini et al., 2018). Whereas, hypermorphic mutations produce excess potassium flux resulting in short QT syndrome and increased risk of sudden cardiac death (Ambrosini et al., 2014).

1.4.3 Kir3.x

Kir3 channels are known as GIRK channels and are gated by GTP binding proteins (G-proteins). GIRK channels are predominantly expressed in the brain and the heart and are strong inward rectifiers that can form homo- and hetero- tetramers. Kir3.1 can co-assemble with Kir3.4 to form the receptor-gated Kir channels, known as K_{Ach} channels (Mesirca et al., 2013). This channel is important for regulating heart rate variability and knock out mice, lacking Kir3.4, were unable to adjust heart rate on a rapid time scale (Wickman et al., 1998). Additionally, in the nervous system, GIRK channels (GIRK1 and GIRK3) play a key role in regulating neurotransmission. GIRK channels hyperpolarise neurons, reducing membrane excitability. Loss of GIRK functions may lead to excessive neuronal excitability, contributing to epileptic seizures (Lüscher and Slesinger, 2010). GIRK channels are also implicated in addiction, with exposure to addictive drugs altering the expression level of GIRK channels in the brains reward circuitry (Rifkin et al., 2017).

1.4.4 Kir4.x and Kir5.x

Kir4 channels are expressed in the kidney and brain with the ability to form homotetramers with intermediate inward rectification properties. Kir4.1 can heteromerize with Kir5.1 producing a channel with stronger inward rectification and higher conductance states. Kir4.2 also forms heterotetramers with Kir5.1in the basolateral membrane of renal epithelial cells (Lourdel et al., 2002). Kir4.1 is implicated in SeSAME syndrome, which affects the brain, ear, and kidney. People affected with SeSAME syndrome suffer from seizures, sensorineural deafness, ataxia, mental retardation, and electrolyte imbalance (Bockenhauer et al., 2009; Scholl et al., 2009). Mutations R65P and G77R result in a large reduction in Kir4.1 current with R65P being located in the PIP_2 binding site and therefore may be affecting activation of the channel (Bockenhauer et al., 2009; Scholl et al., 2009). Kir5 channels do not form homotetramers with itself.

1.4.5 Kir6.x

Kir6.1 and Kir6.2 assemble with an ATP binding cassette protein, known as the sulfonylurea-receptor or SUR (Inagaki et al., 1995; Martin et al., 2017). Kir6.2 and SUR1 combine to form the pancreatic ATP-sensitive potassium (K_{ATP}) channel involved in glucose-mediated insulin secretion (Inagaki et al., 1995). The K_{ATP} channel senses metabolic changes in the pancreatic beta-cell, coupling metabolism to electrical activity and subsequently, insulin secretion (Koster et al., 2005). Opening of K_{ATP} channels hyperpolarises beta-cells and suppresses insulin secretion. Mutations in Kir6.2 underlie neonatal and type 2 diabetes by producing an overactive channel that decreases membrane excitability and affects glucose sensing by the beta-cell (Koster et al., 2005).

1.5 Kir7.1

Kir7.1 is the newest member of the Kir channel family and shares only 24 % sequence identity with Kir channels that lack G-protein activation but are ATP-sensitive, such as Kir1.1, 4.1, 4.2 and 5.1 (Döring et al., 1998; Krapivinsky et al., 1998). It is encoded by the *KCNJ13* gene in humans and is expressed in a variety of tissues (Cornejo et al., 2018; Nakamura et al., 1999; Papanikolaou et al., 2019). Kir7.1 is predicted to share the same molecular architecture as other Kir channels,

possessing two transmembrane spanning domains and a large cytoplasmic domain (**Fig. 1.5**). However, Kir7.1 is unique as it possesses a very low single-channel conductance. This has been linked to the replacement of arginine in most Kir channels with methionine in Kir7.1 within the pore region (Krapivinsky et al., 1998; Partiseti et al., 1998). An additional feature of note is that Kir7.1 has low sensitivity to blockage by external barium ions (Ba^{2+}) and other known potent inhibitory cations of inward rectifying channels (Krapivinsky et al., 1998).

Kir7.1 channels have been localised to epithelial tissues where they have been shown to functionally couple to Na^+-K^+-ATPases contributing to the transepithelial transport of K^+ (Nakamura et al., 1999; Yang et al., 2003). Irrespective of the location, the main function of Kir7.1 appears to be providing a constant background K^+ current. This current contributes to establishing the necessary membrane potential required for transepithelial ion transport driving force.

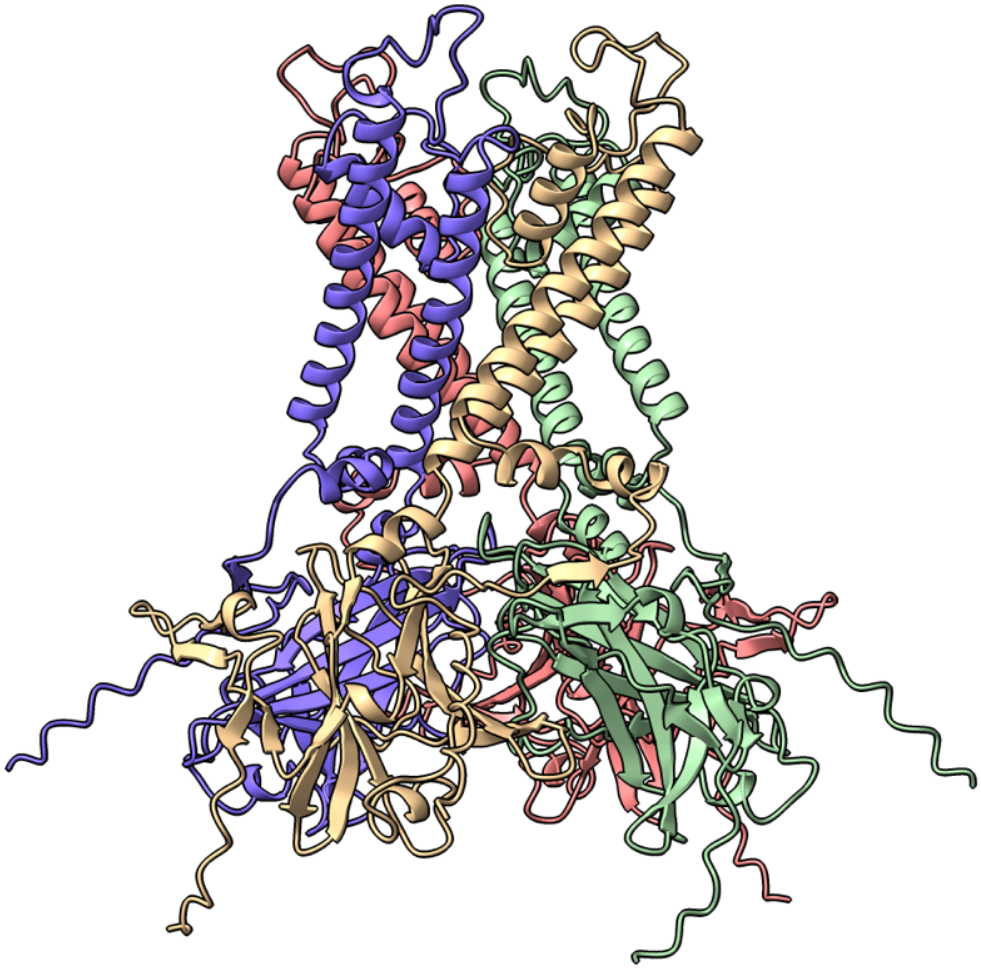

Figure 1.5. Alphafold predicted structure of Kir7.1. Residues 1-7 and 332-360 are hidden due to disorder. The four subunits are coloured differently. Alphafold multimer software was used for structure prediction (Evans et al., 2022; Jumper et al., 2021).

1.5.1 Kir7.1 in the RPE

The retinal pigment epithelium (RPE) is a monolayer of polarised cells that provide a physical and protective blood-retina barrier and facilitates phototransduction in the photoreceptor cells (Strauss, 2005). RPE cells are located between the photoreceptor cells of the retina and the underlying choroid. The apical membrane of the polarised RPE cells face the photoreceptor outer segments and interactions between both the RPE and the photoreceptor cells are vital for visual function (**Fig. 1.6**) (Marmorstein et al., 1998; Thumann, 2001). The photoreceptor cells have no direct vascular supply, therefore, RPE cells must manage molecules and ions flowing in and out of

the retina. The RPE is responsible for several key visual processes and various ion channels and transporters are involved in these functions.

Kir7.1 is located in the apical membrane of the RPE, where it is responsible for maintaining the ionic homeostasis of the subretinal space by transporting ions, metabolites, and fluid between the subretinal space and the choroid (**Fig. 1.6**) (Yang et al., 2008). As the retina is illuminated, K^+ concentration in the subretinal space decreases from 5 mM to 2 mM, whilst the volume in the subretinal space increases (Dornonville de la Cour, 1993). This hyperpolarises the apical RPE membrane and requires tight regulation of subretinal space K^+ ion concentration (la Cour et al., 1986). The inward rectifying ability of Kir7.1 provides a compensatory pathway for the RPE to respond by either rapidly decreasing or increasing the subretinal K^+ concentration. Hejtmancik et al. (2022) identified that *KCNJ13* expression is not necessary for RPE survival, but it is required for RPE maintenance of the photoreceptors.

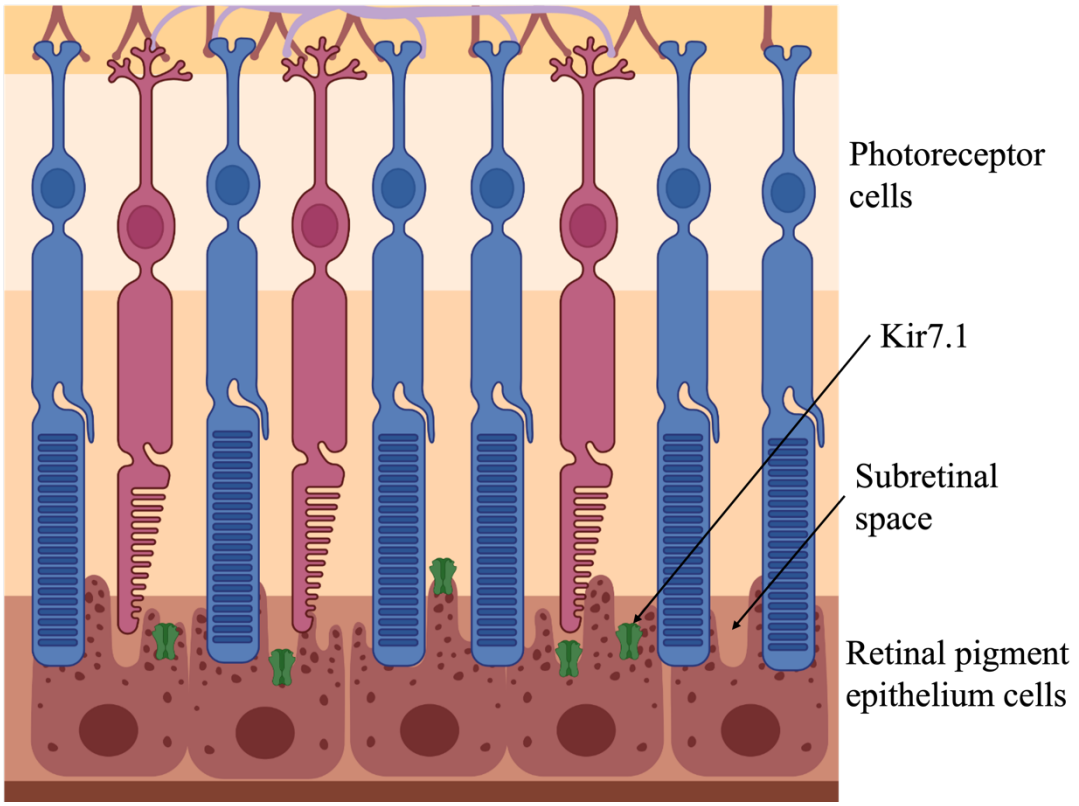

Figure 1.6. Schematic representation of Kir7.1 localisation in the retina. Retinal pigment epithelium cells, photoreceptor cells and the subretinal space are labelled. Kir7.1 exists at the apical process of the RPE. Image created with BioRender.com.

1.5.2 Oxytocin signalling

Oxytocin is a neuropeptide that stimulates the oxytocin receptor (OXTR), a G-protein coupled receptor, and is involved in a wide variety of processes including social bonding, reproduction, and stress response. The OXTR has been localised to the RPE in mice and oxytocin signalling is active in the retina (Halbach et al., 2015). Since OXTR is a G-protein couple receptor, it activates a phospholipase C-mediated signalling pathway and causes hydrolysis of PIP_2. This has a downstream effect of regulating the activation of Kir7.1 in the RPE by depleting PIP_2. York et al. (2018) demonstrated that activation of OXTR causes an inhibition of Kir7.1 channel function and may play a role in regulating retina function.

1.5.3 Kir7.1 in the uterine muscle

The uterine muscle (myometrium) is the muscular layer of the uterus responsible for contractions during labour. Many conditions arise as a result of abnormal uterine activity such as preterm birth, dysfunctional labour, and post-partum haemorrhage. Kir7.1 has been identified as a crucial regulator of membrane potential in uterine myocytes during pregnancy (McCloskey et al., 2014). During gestation, Kir7.1 is highly expressed and maintains the resting potential and dampens excitability of the cell, preventing action potential firing (McCloskey et al., 2014). At the end of pregnancy, this dampening of excitability is removed by a reduction but not complete loss of Kir7.1 expression. Knockdown of Kir7.1, *in vitro*, increased the contractile activity, whereas, over-expression of Kir7.1 decreased contractile activity (McCloskey et al., 2014). This offers a novel pharmacological target to investigate for possible treatment for abnormal uterine activity such as post-partum haemorrhage.

1.5.4 Kir7.1 and energy homeostasis

The melanocortin-4 receptor (MC4R) is a G-protein couple receptor found in the paraventricular nucleus of the hypothalamus (PVN), where it controls food intake (Balthasar et al., 2005). MC4R binds two peptides, α-melanocyte stimulating hormone (α-MSH), which is an agonist that couples the receptor to the Gα signalling pathway, and Agouti-related peptide (AgRP) which binds competitively to block α-MSH binding (Mountjoy et al., 1994; Ollmann et al., 1997). Ghamari-Langroudi et

al. (2015) showed that regulation of neuron firing from the PVN by both peptides can be facilitated by ligand-induced coupling of MC4R to Kir7.1, independently of Gα signalling (Ghamari-Langroudi et al., 2015). This appears to be Kir7.1-specific coupling, as Kir2.3 and Kir4.1 channels did not couple to MC4R when heterologously expressed in HEK293 cells (Ghamari-Langroudi et al., 2015). When Kir7.1 was specifically deleted in the PVN, α-MSH was unable to induce depolarisation, highlighting the physiological role of this coupling (Anderson et al., 2019). Obesity and other eating disorders are a widespread and serious issue. The MC4R has been a central target of drug-discovery research for treating obesity (Ogden et al., 2015). Due to a lack of potency or side effects, melanocortin agonists have yet to be successful in treating dietary obesity. Further research and exploitation of the MC4R-Kir7.1 coupling complex as a new pharmacological target could offer new opportunities in drug discovery.

1.6 Kir7.1 channelopathies

Kir7.1 has been linked to retinal neurodegenerative diseases due its expression in the RPE. Mutations in the gene encoding Kir7.1, *KCNJ13*, are currently associated with three retinal disorders (Hejtmancik et al., 2008; Sergouniotis et al., 2011). Kir7.1 retinopathies are inherited genetic heterogenous disorders caused by either missense or nonsense mutations resulting in loss-of-function of the channel. Eight mutations in Kir7.1 have been linked to retinal diseases (**Table 1.2**). Missense mutations are currently the most common structural mutation. A full characterisation and understanding of these mutations has not been reported to date.

Mutation	Protein Location	Disease	References
T153I	Transmembrane domain	Leber congenital amaurosis	(Beverley et al., 2022)
R166*	PIP_2 binding site/TMD-CTD linker		(Sergouniotis et al., 2011)
L241P	Cytoplasmic domain		
W53*	N-terminus		(Pattnaik et al., 2015)
S105I	Transmembrane domain		(Perez-Roustit et al., 2017)
Q219*	Cytoplasmic domain		

R162W	PIP_2 binding site/ TMD-CTD linker	Snowflake vitreoretinal degeneration	(Hejtmancik et al., 2008; Lee et al., 2003)
R162Q	PIP_2 binding site/ TMD-CTD linker	Retinitis pigmentosa	(Sergouniotis et al., 2011)
I120T	Selectivity filter	Other vitreoretinal dystrophy	(Khan et al., 2015)

Table 1.2. Kir7.1 mutations identified in retinopathies. Summary of all disease-associated mutations in Kir7.1 and their location within the channel.

1.6.1 Snowflake vitreoretinal degeneration

Snowflake vitreoretinal degeneration (SVD; MIM #193230) is a disease characterised by small crystalline deposits resembling snowflakes in the retina, as well as fibrillary vitreous degeneration, and cataracts. It is a rare disease with an occurrence of less than one in one million, with exact figures unknown. From a study conducted on an American family of 31 individuals, the inheritance pattern of the disease was identified as autosomal dominant and the gene involved in the disease was identified as *KCNJ13*, the gene responsible for encoding Kir7.1 (Hirose et al., 1974). When *KCNJ13* from both an affected and an unaffected individual was sequenced, a C > T transition was identified, mutating a CGG codon to TGG, causing an R162W change in the amino acid sequence of Kir7.1 (**Fig. 1.7**) (Hejtmancik et al., 2008). This one nucleotide change was only found in patients with SVD and never identified in any unaffected individual with over 200 people tested (Hejtmancik et al., 2008). Substituting an arginine residue to a tryptophan residue results in a positive hydrophilic arginine being replaced by an aromatic, hydrophobic tryptophan.

As previously described, Kir7.1 plays an important role in the apical processes of the RPE. It is unclear exactly how the R162W mutation affects these processes, but loss of channel activity could drastically impact RPE physiology and cause the clinical pathology of SVD. The C-terminal sequence of Kir7.1 possesses a conserved cluster of basic residues that are crucial for electrostatic interactions and are responsible for the flexibility of the linker sequence (Pattnaik et al., 2013). This specific cluster contains the R162 residue and is part of the regulatory PIP_2 binding site (Pattnaik et al., 2013). Arginine and tryptophan are similar in size but different in charge and this

could impact channel functionality. The arginine residue in the PIP_2 binding site is providing a positively charged residue which the negatively charged PIP_2 likely interacts with. This arginine at residue 162 corresponds to arginine at residue 186 in the Kir2.2 structure solved with PIP_2 present (**Fig. 1.4**). In the Kir2.2-PIP_2 structure R186 directly interacts with the 4' and 5' phosphates of PIP_2. A Kir2.2 variant, replacing the arginine with an alanine was also solved with PIP_2 bound and the CTD was shown in the docked, open position (Hansen et al., 2011). This shows that the arginine is not crucial for PIP_2 to bind to Kir2.2 and induce the conformational change. The impact of different mutations at position 162 in Kir7.1 was investigated using smaller neutral residues (Sergouniotis et al., 2011). Mutating the arginine to a glutamine decreases but does not abolish channel activity and causes late onset retinitis pigmentosa, a milder pathology than R162W-associated SVD (Sergouniotis et al., 2011). However, when the arginine was replaced with a cysteine, channel activity was actually enhanced compared to the wild type (WT) channel (Vera et al., 2021). This suggests that rather than a loss of a charge it is the size of the residue side chain that is exerting the effect. An R162W mutation removes a positive charge but it is the large residue size that exerts the dominant negative effect.

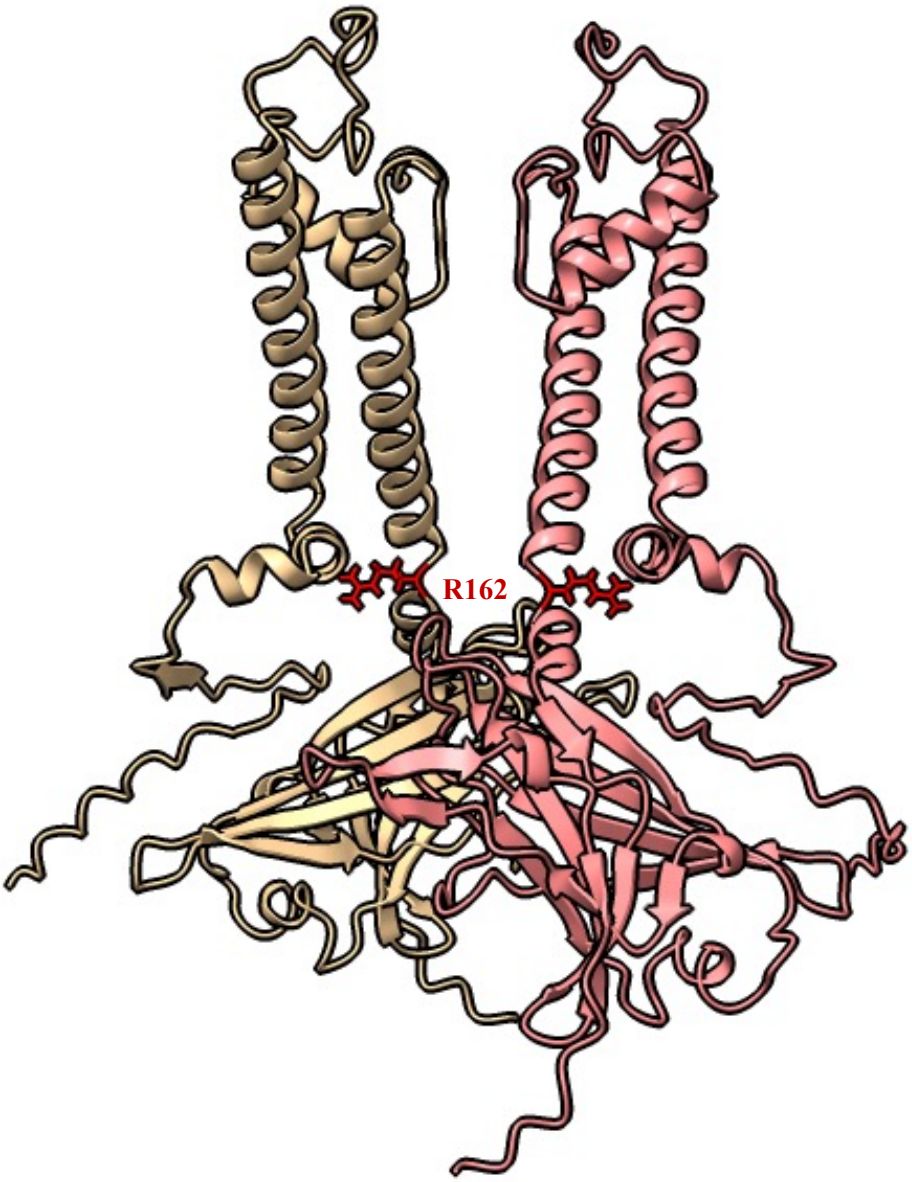

Figure 1.7. SVD-associated residue in Kir7.1. Alphafold predicted model of Kir7.1 with the SVD-associated residue 162 shown in red. Arginine in unaffected individuals is mutated to a tryptophan in SVD-affected individuals at position 162.

A flexible TMD-CTD linker sequence is located between the TMD and CTD of Kir channels and it is predicted to be responsible for the docking motion seen post PIP_2 activation (**Fig. 1.4**) (Hansen et al., 2011). The R162W mutation in this linker sequence could result in a loss of flexibility, as tryptophan is a bulky non-polar amino acid, which would stiffen the structure and impede the opening and closing of the channel (Pattnaik et al., 2013).

Another possibility is that the structural changes from this mutation could affect Golgi-to-membrane trafficking. Experiments by Pattnaik et al. (2013), using Kir7.1-R162W mutant channels expressed in Chinese hamster ovary (CHO) cells, demonstrated that mutant channels failed to traffic to the membrane. However, similar work carried out by Zhang et al. (2013) using an oocyte expression system, demonstrated non-functional Kir7.1 mutant channels. In this instance, the mutant channels were capable of successfully localising to the membrane but were non-functional once there (Zhang et al., 2013). This is an interesting comparison of a CHO and an oocyte expression system. It is possible that the difference in culture temperature for the oocyte expression system, which is ideal for studying ion channel physiology, may not be representative of membrane trafficking (Leduc-Nadeau et al., 2010). Trafficking of Kir7.1 may be mediated by signals from the cytoplasmic domain, however, this mechanism is yet to be fully evaluated and additionally how the 162 residue is involved in this process (Tateno et al., 2006). This leaves the Kir7.1-R162W channel and its involvement in SVD not fully understood.

1.6.2 Leber Congenital Amaurosis

Leber congenital amaurosis (LCA; MIM #204000) is a rare congenital autosomal-recessive retinal blindness depicted by serious vision impairment, nystagmus, and photophobia (Fazzi et al., 2003). Mutations in at least twenty genes have been linked to LCA, affecting either the photoreceptors or the RPE (den Hollander et al., 2008). *KCNJ13*, encoding Kir7.1, is the sixteenth gene implicated in LCA (LCA16; MIM #614186). Various mutations at different locations in Kir7.1 have been associated with LCA16 (**Table 1.2**). A full characterisation of all mutations in Kir7.1 and the mechanism for how they cause the disease is not understood. Some mutations have been studied and will be summarised.

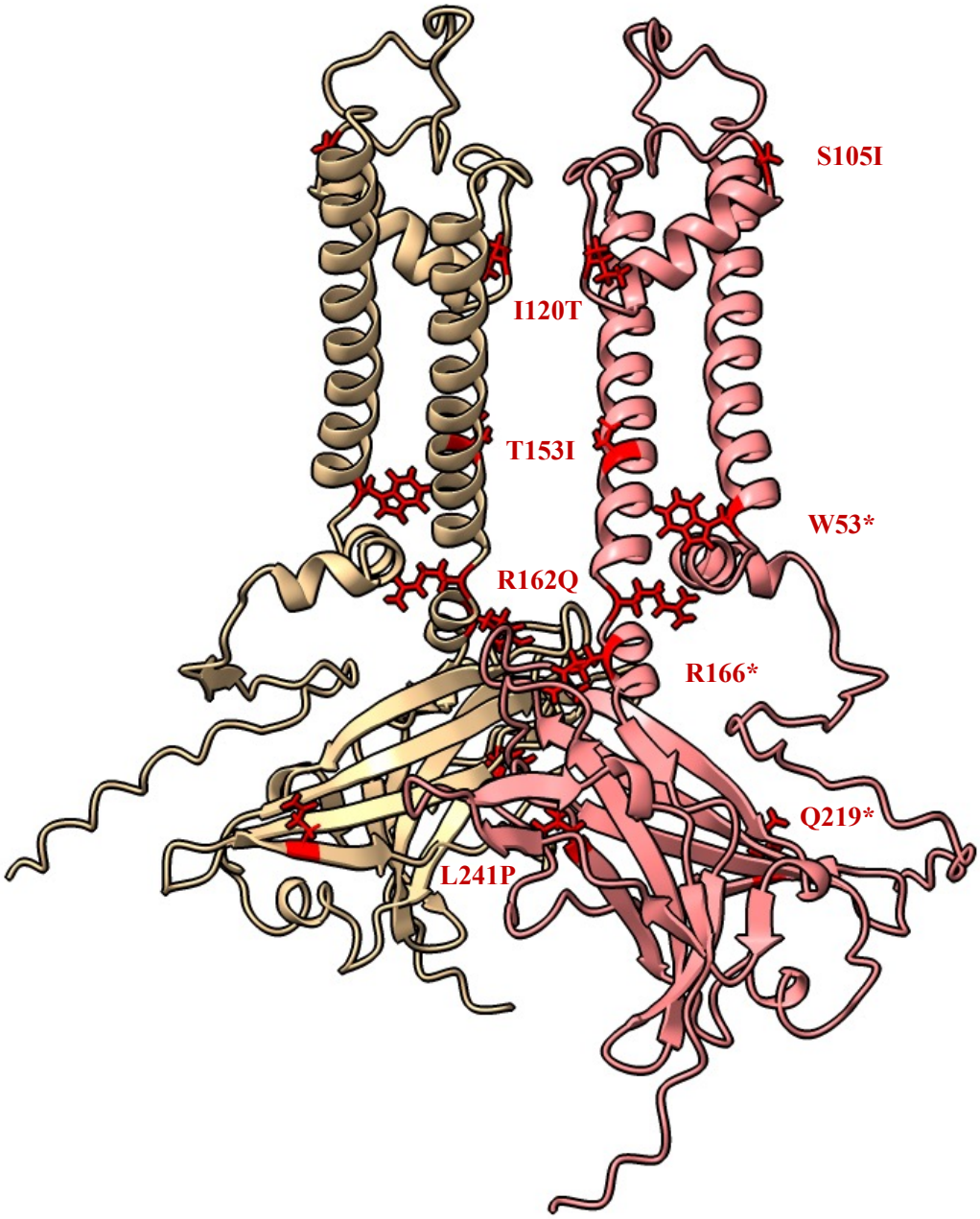

Figure 1.8. LCA associated residues in Kir7.1. An Alphafold predicted model of Kir7.1 with LCA associated residues shown in red. Two chains of the channel are shown for clarity. All labelled residues have been independently identified in an individual affected with LCA.

1.6.2.1 T153I

A missense mutation at residue position 153, located in the transmembrane domain, replaces a hydrophilic threonine with a hydrophobic isoleucine (**Fig. 1.7**). This variant causes the LCA16 phenotype in humans and zebrafish (Toms et al., 2019). T153I is positioned in the inner pore region where regulation of the channel is

unclear (Kumar and Pattnaik, 2014). In strong inward rectifier channels this residue is hydrophobic, whereas in weak inward rectifiers this residue is hydrophilic. Beverley et al. (2022) tested the effect of mutating residue 153 to either polar, non-polar or short-chain amino acids. The T153I variant produced a full-length protein and successfully localised to the membrane (Beverley et al., 2022). However, when the functionality of the T153I variant was tested, the channel was non-functional and showed no current, concluding that it does not permeate any potassium ions (Beverley et al., 2022). Mutating the threonine to a small-chain amino acid (glycine or alanine) also produced non-functional ion channels. T153C mutant channels exhibited a functional channel similar to WT Kir7.1, whereas T153S channels were active but with reduced or altered function. This amino acid site has an impact on the pore radius, and from the mutants tested, larger pores and smaller pores were analysed. Therefore, the specific size of the pore is important for channel function, it needs to be narrow but not too narrow. Along with the influence of pore size, the presence of a polar side chain is also required for channel function (Beverley et al., 2022). This work highlights the impact of the T153I mutation on channel function and how it may cause LCA.

1.6.2.2 L241P and glycosylation

Carrington et al. (2018) demonstrated the importance of Kir7.1 glycosylation on channel function. It was shown that GPCRs (β2-, β1-, and β3- adrenergic receptor) mediate reduction in Kir7.1 glycosylation and therefore channel activity. This lack of glycosylation did not affect surface expression of the channel but whole cell currents were reduced when Kir7.1 was co-expressed with the β2-adrenergic receptor (Carrington et al., 2018). The asparagine at position 95 in Kir7.1 is positioned in the extracellular turrets and is a known glycosylation site (Döring et al., 1998). Carrington et al. (2018) showed that mutating this residue, preventing glycosylation, showed similar results to when the WT channel is expressed alongside the β2-adrenergic receptor. It is worth noting that MC4R, the GPCR shown to couple to Kir7.1 (**Section 1.5.4**), did not have an effect on the glycosylation of the channel. The role of the glycans and their mechanism for facilitating channel functionality is not clear. The L241P variant, associated with LCA (**Table 1.2**), showed almost a complete loss in channel glycosylation (Carrington et al., 2018). This mutation has

not been fully investigated but this may suggest that a loss of channel activity is due to a lack of glycosylation.

1.6.2.3 W53* and gene therapy

The *KCNJ13* loss-of-function phenotype is a good candidate for gene-therapy. Shahi et al. (2019) used induced pluripotent stem cells (iPSC)-RPE derived from a LCA16-affected individual for modelling and exploring novel approaches to variant-specific treatments. The W53* variant, causing an early termination of protein expression, was investigated in this study (**Table 1.2**). An evaluation of iPSC-RPE cells derived from an LCA16 affected individual and an unaffected family member showed normal RPE morphology in both cells and no difference in RPE-specific genes between cell types (Shahi et al., 2019). Kir7.1 expression was found in the apical membrane of the control iPSC-RPE cells but not in the affected LCA16 cells, suggesting a failure of expression or trafficking of the Kir7.1-W53* variant. Additionally, RPE cells play an important role in phagocytosis of the photoreceptor outer segments (POSs) and the impact of Kir7.1 absence on this process was tested. Treating the iPSC-RPE cells with POSs showed that the affected cells failed to process phagosomes, and this may result in a build-up of POSs overtime. This is consistent with the slow progression toward blindness in LCA16-affected individuals (Shahi et al., 2019). Additionally, no Kir7.1 activity could be detected in the LCA16 iPSC-RPE cells, and the membrane potential was more depolarised compared to control cells. This reinforces the hypothesis that LCA blindness is a result of a non-functional Kir7.1 channel that depolarises RPE cells.

Recent studies have shown the usefulness of readthrough therapy as a treatment that could improve vision (Goldmann et al., 2012, 2011; Schwarz et al., 2015). This technique uses designer aminoglycosides that bind to the ribosomal-RNA decoding site which promotes the transition of the 16S rRNA decoding centre from a tRNA binding conformation to a productive state, resulting in an increase rate of readthrough at a stop codon (Pape et al., 2000). Shahi et al. (2019) demonstrated that the W53* variant is suppressed by the incorporation of a near-cognate aminoacyl tRNA in the presence of the small-molecule readthrough NB84 (Goldmann et al., 2012; Nudelman et al., 2010; Ramsden et al., 2017). Both membrane potential and current deficits were corrected using NB84 to treat W53* variant cells along with

identification and newly expressed full-length Kir7.1 at the apical membrane (Shahi et al., 2019). This is a promising proof of concept for readthrough and gene augmentation therapies with further research and testing necessary.

1.7 Aims of the project

The structure of Kir7.1 remains to be determined, and the homologous structures currently published share little sequence identity with Kir7.1. Given the channel's novel characteristics and diverse functions, it is important to conduct structural investigations to enhance our understanding of this channel. Functional studies have demonstrated that Kir7.1, like other human Kir channels, is activated by PIP_2. Our objective is to unravel the native structure of Kir7.1 and explore how PIP_2 activation triggers conformational changes in the channel.

Additionally, Kir7.1's role in rare retinal diseases is a motivation for this work. We aim to interpret how these mutations hamper channel activity and cause such diseases. By understanding the structural implications of any of these mutations, we hope to aid further research into Kir7.1 and retinal diseases.

Chapter 2

2. Cryo-EM and single-particle analysis

2.1. Introduction

This chapter focuses on cryogenic electron microscopy (cryo-EM) and single-particle analysis providing a summary of the main experimental and computational principles underlying the technique. It is based on the LMB 2017 cryo-EM course and references (Orlova and Saibil, 2011; Passmore and Russo, 2016; Scheres, 2012; Scheres and Chen, 2012; Sigworth, 2016; Zivanov et al., 2018).

For a comprehensive understanding of biological processes, it is useful to obtain the three-dimensional (3D) arrangement and dynamics of molecules and molecular complexes. The structural biology techniques of X-ray crystallography and nuclear magnetic resonance (NMR) are powerful approaches for determining detailed high-resolution information. On a larger scale, optical microscopy unveils the spatial arrangement and movement of molecules labelled with fluorophores within cells, offering valuable insights into their behaviour.

Cryo-EM emerges as a versatile tool capable of elucidating structural details across various scales, ranging from the entire cell (tomography) to individual molecules and complexes (single-particle analysis).

2.2 Transmission EM for imaging biological samples

Biological samples used for transmission electron microscopy are limited by their susceptibility to radiation damage. Organic matter primarily comprises atoms with relatively low atomic weights, and the covalent bonds between these atoms exhibit energies typically in the range of a few electron volts (eV) (Baker and Rubinstein, 2010). However, electron microscopes employ electron energies ranging from 200 to 300 keV, which can result in the breakage of chemical bonds within biological samples upon irradiation. The rupture of these bonds results in the generation of free radicals, which have the ability to migrate throughout the specimen and induce additional chemical damage (Baker and Rubinstein, 2010). To overcome this issue, imaging is conducted under ‘low-dose’ conditions.

2.3 Sample preparation

2.3.1 Biochemistry

Single-particle EM relies on the summation of thousands of images of identical particles. While sample heterogeneity does not necessarily impede structural analysis, it is highly recommended to prioritise efforts in homogenising the sample. Protein purity is measured by sodium dodecyl-sulfate polyacrylamide gel electrophoresis (SDS-PAGE) using either Coomassie or silver-staining. However, it is important to note that a sample that appears pure based on SDS-PAGE and size exclusion chromatography may still not be suitable for EM analysis. Complexes that appear intact using these methods may actually consist of a mixture of sub-complexes with different compositions or homogenous complexes capable of adopting various conformations.

2.3.2 Negative stain EM

A common approach for assessing whether the sample is appropriate for EM analysis or not is visualising it by negative stain EM. Negative staining (NS) is a quick and simple method. This method involves adding a droplet of sample onto an EM grid and then embedding it in a heavy metal salt solution, usually uranyl acetate (**Fig. 2.1**). This is blotted to a thin film and allowed to dry. The use of a heavy metal stain provides increased specimen contrast and a higher electron dose limit that the sample can withstand. NS-EM is capable of providing information for 3D reconstruction, but it is limited by the grain size of the stain used, e.g., for uranyl acetate this is ~20 Å. There is also a lack of internal feature resolution due to the inability of the stain to penetrate the structure. The benefit of NS-EM is the little time it takes to prepare grids which allows many conditions to be screened in a single day.

2.3.3 Cryo-EM

To achieve high-resolution imaging of biological samples, it is essential to image them in a stain-free and hydrated state under native conditions. This requires maintaining the sample at low temperatures to preserve its integrity, minimise contamination, and reduce radiation damage. Cryo-EM involves embedding the sample in a thin layer of amorphous ice and ensuring rapid cooling to prevent the

formation of ice crystals. This rapid freezing enables the preservation of the sample's hydration without dehydration.

2.3.4 Plunge-freezing

Plunge-freezing involves the application of a sample onto an EM grid, blotting to remove excess solution, before immediately plunging into liquid ethane or propane (-182 °C) (**Fig. 2.1**). Ethane is cooled by liquid nitrogen and has a high thermal conductivity. Liquid ethane is more effective than liquid nitrogen for rapid cooling of samples due to its proximity to the freezing point, enabling faster heat transfer and minimising the formation of insulating gas layers. Rapid freezing captures the sample in a native, hydrated state in vitreous ice. Grids are stored in liquid nitrogen and kept at temperatures low enough to maintain vitreous conditions. Samples will be devitrified at temperatures above -137 °C allowing crystalline ice formation that can damage the sample and interfere with imaging (Dubochet et al., 1988). Furthermore, the low temperatures necessary for maintaining vitrification also contribute to slowing down the damaging effects of the electron beam (Baker and Rubinstein, 2010).

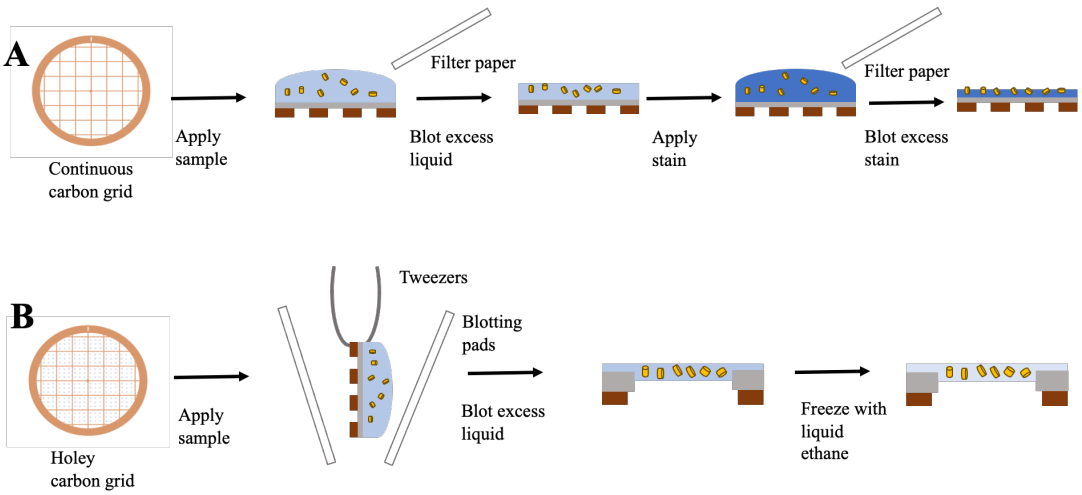

Figure 2.1. Grid preparation for negative stain EM and cryo-EM. A. Negative stain EM involves applying the sample onto a carbon grid, followed by staining with a heavy metal salt. Excess liquid is removed through blotting, and the stain is then dried. **B.** In cryo-EM, the sample is applied to a holey carbon grid. After blotting to remove excess solution, it undergoes plunge freezing, where the biological

specimens are suspended within a layer of vitreous ice. Adapted from Orlova and Saibil (2011).

2.3.5 Parameter optimisation

Grid type

Small amounts of purified sample (~3 μL) are applied to EM grids consisting of a copper mesh supporting a thin film. This type of support can differ depending on the needs of the user and the application. For NS-EM a continuous layer of amorphous carbon is used. Whereas, for cryo-EM, perforated films are used with the sample being imaged in ice suspended over holes in the film. Commonly used grid types for electron microscopy include Quantifoil and C-flat grids, which feature regularly arranged holes that facilitate both automated and manual data collection processes. One limitation associated with EM supports is that thin carbon films can exhibit instability and poor conductivity when exposed to low temperatures (Y. Cheng et al., 2015). This has a significant impact on beam-induced movement, which ultimately contributes to the degradation of image quality. To counteract this and make the grids more mechanically stable, different designs have been tested, such as using gold support (Russo and Passmore, 2016). Prior to the addition of the sample to these grids, it is essential to subject them to glow discharge, a process that renders the grids hydrophilic. This facilitates a small volume of sample being distributed evenly across the whole grid. Grid support and glow discharge conditions can be adjusted and optimised per sample.

Ice thickness

Automated plunge-freezing is facilitated by commercially available instruments like the Vitrobot (Thermo Fisher Scientific). Adjusting various parameters is crucial for obtaining suitable ice and well-distributed particles. The desired vitrified grid should consist of amorphous ice with an adequate thickness to encapsulate particles while maintaining their visibility in different orientations across the field of view.
If the ice is excessively thick, image contrast decreases, and particle overlap may occur. Conversely, overly thin ice can exclude particles from the holes and lead to denaturation at the air-water interface. In practice, grids typically exhibit an ice gradient due to variations in blotting. Insufficient blotting can result in thick ice,

while excessive blotting leads to thinner ice. It is possible for users to selectively choose grid squares and holes from this gradient that are ideal for imaging. By adjusting parameters like blotting time and force, researchers can optimise plunge freezing for their samples, ensuring the production of consistent grids suitable for data collection.

Particle stability and distribution

Optimising freezing conditions is crucial as it directly impacts particle behaviour. Increasing the duration between sample addition, blotting, and freezing results in greater water evaporation, leading to solute concentration. This concentration can induce pH or salt level changes, thereby affecting particle stability. Other parameters that need to be considered for optimisation include protein concentration, buffer composition, grid type and grid treatments. Obtaining monodisperse, randomly orientated particles on a grid can be a difficult task.

In theory, protein particles would live within the EM grid holes in a thin layer of ice. However, in practice, particles may exhibit a preference for adsorption to the support film, resulting in a lower concentration of protein observed within the holes. Often, increasing protein concentration or using additional continuous support layers (e.g., graphene oxide) can help overcome this issue. The utilisation of a graphene oxide (GO) layer provides the grid with a physical surface to which the particle can adhere. This additional layer means a lower protein concentration can be used which may be advantageous for more challenging proteins. However, it can reduce image contrast and may cause the molecules to adopt preferred orientations.

Particle orientation

Ideally, particles should adopt a wide variety of orientations away from the air-water interface. However, most particles favour some orientations over others, displaying a degree of preferred orientation. This phenomenon can be attributed to the surface properties of the molecules, such as hydrophobic patches that tend to interact more strongly with specific interfaces. Preferred orientation can result in a lack of views of the protein, meaning high-resolution structural determination is limited.

Additionally, if the particle is interacting with the air-water interface it may be partially or fully denatured (Noble et al., 2018). Various approaches can be employed to mitigate preferred orientation, such as the addition of detergents, which

can modify the surface tension of water and prevent particle interaction with the air-water interface (Chen et al., 2019). However, this process involves screening multiple additives and conditions to achieve optimal results, which can be time-consuming and labour-intensive.

Sample preparation in cryo-EM represents a significant bottleneck, often requiring extensive time for screening and optimising conditions to obtain ideal grids. Consistently achieving high-quality grids in a reliable manner presents challenges that can prolong and complicate the overall process. However, the upcoming generation of cryo-EM instruments aims to automate this process, offering enhanced consistency, reliability, efficiency, and cost-effectiveness.

2.4 Image formation and detection in the electron microscope

Electron microscopy is comparable to light microscopy, as both instruments consist of a radiation source, a series of lenses, and a detector. The resolution limit of a microscope is approximately half the wavelength of the radiation source employed. In the case of light microscopy, the resolution is limited to around 200 nm due to the wavelength of visible light ranging from 400-700 nm (Penczek, 2010). However, when electrons are accelerated at a voltage of 300keV they have a wavelength of approximately 2 pm (0.02 Å) (Penczek, 2010). In theory, the resolution of electron microscopes for biological samples is considered to be unlimited. However, in reality, the achievable resolution is limited by factors such as the properties of the microscope itself and the nature of the sample being observed.

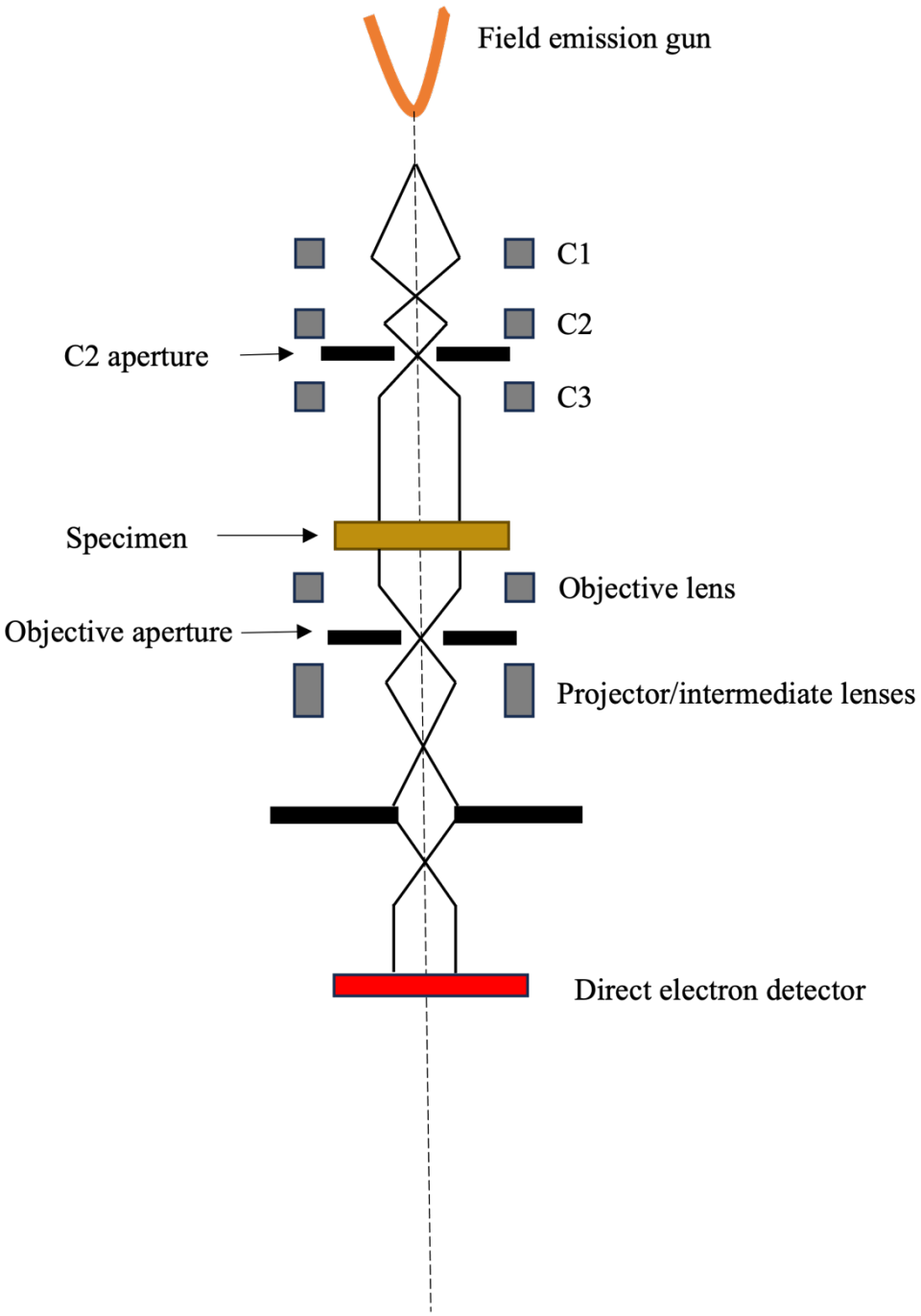

Figure 2.2. A schematic representation of a transmission electron microscope. Reproduced from Orlova and Saibil (2011).

2.4.1 Electron sources

The transmission electron microscope (TEM) comprises a column containing multiple electromagnetic lenses and apertures (**Fig. 2.2**). The system operates under vacuum to enable the unobstructed flow of electrons. Acceleration voltages ranging from 80-300 keV are employed to emit electrons. Microscopes utilise various

electron sources, including tungsten filaments and LaB_6 crystals in lower-end instruments, and field emission guns (FEG) in higher-end microscopes. FEGs feature a smaller source size, resulting in a brighter and more coherent electron beam.

2.4.2 Lenses

Lenses in a TEM are essential for manipulating the electron beam to achieve high-resolution imaging of the specimen. Similar to optical lenses in light microscopy, electromagnetic lenses in a TEM focus and control the path of electrons to form a coherent beam. The primary objective lens in a TEM focuses the scattered electron beam onto the back-focal plane, allowing for fine-tuning of image sharpness and contrast. The insertion of the objective aperture restricts high angle scattered electrons, enhancing image contrast, and reducing background noise. Intermediate and projector lenses further magnify the image, contributing to overall magnification and resolution. Lenses in a TEM play a vital role in manipulating the electron beam, controlling focus, improving contrast, and magnifying the image.

2.4.3 Interaction of electrons with the sample

The majority of electrons (~80 %) pass through biological samples, due to their composition of low atomic number elements. Among the electrons that do interact with the sample, their interactions can be classified as either destructive (inelastic scattering) or non-destructive (elastic scattering). Approximately 5 % of electrons are elastically scattered where they interact with the sample without transferring energy to the sample (**Case 2 Fig. 2.3**). The electron's wavelength is unchanged, but it undergoes a phase shift. The scattering angle and phase shift in cryo-EM are influenced by the sample, with molecules containing higher atomic numbers exhibiting larger deflections and phase shifts.

Inelastic scattering (~15 % of electrons) happens when an electron interacts with the sample and transfers energy to the specimen (**Cases 3 and 4 Fig. 2.3**). This causes radiation damage by ionisation, X-ray emission, free-radical production, or chemical bond alterations. Due to the energy loss during scattering, the scattered electron undergoes a wavelength increase and converges at different planes compared to the elastically scattered or unscattered electrons. This phenomenon introduces chromatic aberration and contributes to additional noise in the image.

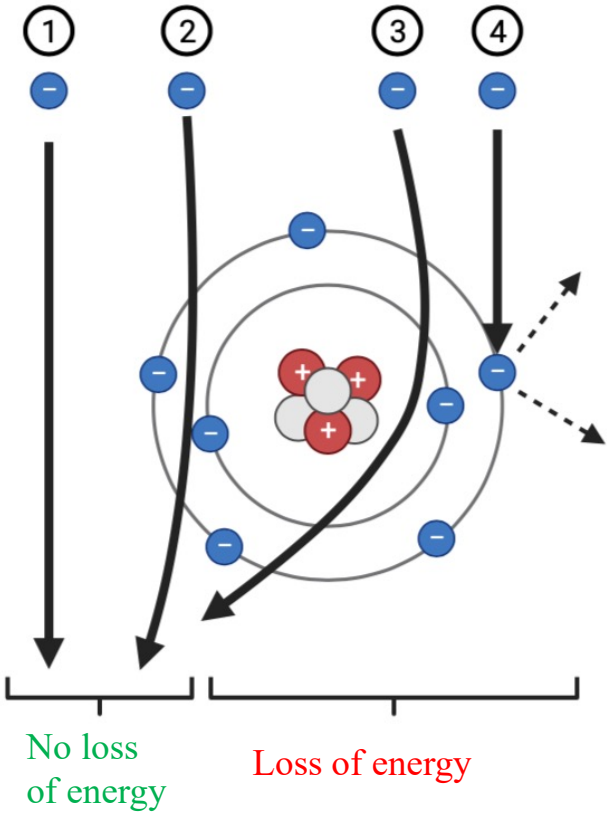

Figure 2.3. Interactions between the electron and the sample.
Cases 1 and 2 represent elastic scattering where no energy is lost. Cases 3 and 4 display inelastic scattering. Adapted from Orlova and Saibil (2011).

2.4.4. Contrast transfer

In cryo-EM, amplitude contrast arises when electrons are absorbed by the sample. To enhance this contrast, an objective aperture can be placed at the back focal plane, where the diffraction pattern forms. By selectively blocking electrons that scatter at high angles, the aperture reduces image noise and enhances clarity, resulting in improved visualisation of the sample.

Phase contrast arises from the interference between unscattered electrons and elastically scattered electrons as they pass through the sample. The phase shift of electrons occurs due to interactions with the specimen's atoms, which can cause a change in the direction and phase of the electron wave. This phase shift carries valuable information about the sample, such as its structure and composition. To detect phase contrast, specialised imaging methods and optical components are

employed in the electron microscope. Spherical aberrations in the microscope lenses cause variations in the path length of the electron waves passing through different regions of the sample. As a result, the phase of the scattered electrons differs from that of the unscattered electrons.
By manipulating the electron optics and detecting these phase differences, phase contrast can be visualised in the resulting images. This technique enhances the visibility of structures and details that may not be apparent in amplitude contrast alone, allowing for a more comprehensive analysis of the specimen.

2.4.5 Contrast transfer function

Enhancing image contrast in electron microscopy can be achieved through an effective technique known as microscope defocusing. By intentionally increasing the defocus, the path length of scattered electrons is extended due to the presence of spherical aberrations in the lenses. This conversion from phase contrast to visible amplitude contrast is described by the contrast transfer function (CTF). The CTF is a sinusoidal function in Fourier space that is dependent on the defocus parameter. It ranges between -1 and 1, representing the transfer of contrast at different spatial frequencies. Plotting the CTF allows for the visualisation of how contrast is transferred to the image at each specific spatial frequency.

2.4.6 Detectors

The final step in microscopy is image detection. Initially, photographic films were used, which were cost-effective but time-consuming to handle. The introduction of digital detectors like charge-coupled devices (CCDs) provided easier and automated usage. More recently, direct electron detectors (DEDs) have emerged, enabling the direct detection of electrons. They improve sensitivity and significantly enhance the signal-to-noise ratio. The lower dose rate and higher frame rate prevent coincidence loss, where multiple electrons hit the same detector area, preserving image quality. DEDs exhibit a higher Detective Quantum Efficiency (DQE) compared to CCD cameras, reaching values of 0.8 or higher, indicating improved signal-to-noise performance. The progression of DEDs, coupled with advancements in image processing software, has led to the "resolution revolution" in cryo-EM. The

significance of these advancements has been extensively reviewed (Bai et al., 2015; Glaeser, 2019; Nogales and Scheres, 2015).

2.5 Image processing

2.5.1 Motion correction

DEDs capture a series of sub-frames or movies instead of a single image. These sub-frames are aligned to correct for sample drift and beam-induced movement and then averaged to generate a final image for further processing. Optimising the overall signal-to-noise ratio (SNR) involves utilising early frames with a low electron dose, which capture high-resolution signals from less damaged sample regions. However, these early frames are affected by sample movement, reducing the clarity of high-resolution information. As sample movement decreases, the impact on later frames diminishes. However, the higher electron dose in these later frames leads to a loss of high-resolution information. To address this, movie frames are averaged with relative weighting to optimise the signal in the final image. This weighting ensures a balance between resolution and SNR (Campbell et al., 2012; Scheres, 2014).

2.5.2 CTF estimation

Cryo-EM images undergo modulation by the CTF. The CTF consists of known parameters determined by microscope settings, such as acceleration voltage and spherical aberration. However, the defocus, an unknown component of the CTF, must be determined for each experimental image. This is achieved by fitting a theoretical model to the power spectra of micrographs, enabling image correction using the established CTF. Initially, CTF estimation is performed on a per-micrograph basis. In later stages, the CTF can be further refined on a per-particle basis using an alternate method, resulting in more precise CTF estimation, and enabling higher-resolution reconstructions.

2.5.3 Particle picking and extraction

Most single-particle cryo-EM software packages offer automated or semi-automated particle picking tools. Automated particle picking eliminates the need for manual selection but may have limitations, such as picking high-contrast areas like ice crystals and carbon edges. Once particles are picked, they need to be extracted from

the micrographs using an image/box size. The box size parameter for particle extraction is adjustable and can benefit from optimisation, although starting with a size around 2.5 times the particle diameter is typically sufficient. Once extracted, the particles are prepared for classification and alignment steps.

2.5.4 2D classification

It is difficult to investigate the particles within an image due to the low SNR. 2D classification employs clustering techniques to group similar particle images and generate class-average images, enabling better evaluation of the dataset contents. Relion uses maximum likelihood 2D classification which starts with a set of random reference images (Scheres, 2012). For each particle image, the probability is calculated in relation to its rotation, translation and the degree of matching to each reference (Sigworth, 2016). A weighted average of the possible class assignments is used to determine a 2D class average. These 2D averages are then used for references in the next iteration of 2D classification. This process continues until each particle image converges to a single 2D class average.

2D classification reveals the heterogeneity in the dataset, showcasing different conformations and sizes of particles. Good class averages exhibit well-resolved protein features, while bad classes may have damaged or misaligned proteins, ice contamination, or film edges. Selected good classes are used for further processing and analysis.

2.5.5 3D reconstruction and refinement

Three-dimensional reconstruction focuses on seeking five orientation parameters (three Euler angles and two translations) for each projection image producing a final 3D structure. The success of the 3D orientation search is dependent on the data quality so only class averages of homogeneous particle groups should be used. The first step is to generate an initial map that is an estimate of the final 3D map. This map can be produced either experimentally, computationally or from existing cryo-EM or crystal structures. When incorporating pre-existing structures in 3D refinement in cryo-EM, it is crucial to filter them to a low resolution to prevent bias during the processing. The refinement process begins by projecting this initial map to generate reference images, which are then compared to each particle image. This

technique, known as projection matching, is a common feature in 3D refinement software.

To overcome errors in orientation assignment, maximum-likelihood and statistical approaches are employed, enabling the production of successful 3D reconstructions despite these challenges. This is achievable by avoiding the discrete assignment of particle orientation but instead using a 'fuzzy' assignment based on computed orientation probabilities. These computed probabilities for a particle image are then used as weights in applying the information from that image in the 3D reconstruction (Scheres, 2012). It is crucial to assign stronger weights to particle images that provide more signal or more reliable orientation information (Grigorieff, 2007). After reviewing all particle images and generating a 3D reconstruction, a new set of reference projections is created based on this model for the next iteration of 3D refinement. This iterative refinement process continues until convergence is achieved in the angular assignments of particles.
Refinement progress is measured by several indicators, one key measure is the Fourier shell correlation (FSC) curve which quantifies the agreement between two independently refined half-maps, revealing the level of resolution and signal-to-noise ratio (SNR) as a function of spatial frequency. (Penczek, 2010). The dataset is divided into two halves, and a volume is generated for each half through iterative refinement, with progress assessed after each iteration. By comparing the resulting 3D reconstructions from each half, an FSC curve can be obtained. The correlation coefficients for each resolution shell are calculated from the Fourier transforms of both maps. Known as the gold-standard FSC, this approach aims to mitigate overfitting in the refinement process (Scheres and Chen, 2012).

Gold-standard FSC curves play a crucial role in assessing the resolution and quality of cryo-EM maps. The map resolution is typically determined by identifying the spatial frequency value at which the FSC reaches 0.143. This threshold value is derived from comparisons between cryo-EM maps and high-resolution crystal structures (Rosenthal and Henderson, 2003). However, it's important to note that cryo-EM map resolution represents an average across the entire structure, and there may be variations in resolution within different regions due to heterogeneity and flexibility. To capture these differences, local resolution estimations can be

calculated for cryo-EM maps, providing insights into the varying resolution levels across the entire structure.

2.5.6 3D classification

Many samples exhibit varying degrees of heterogeneity, which can arise from subpopulations adopting different conformations or the inclusion of additional density from subunits, substrates, or ligands. During the initial "consensus" refinement step, where all particles from good 2D classes are utilised, these subtle details may not be apparent. To address this, 3D classification is employed to categorise particles into more homogeneous groups and attempt to resolve any existing differences.

In 3D classification, multiple reconstructions are simultaneously refined, with the user determining the number of classes. Each 3D refinement begins with an initial reference map. Inputted particles are randomly divided among the 3D classes and compared to projections generated from the reference map. The particles are assigned probabilities for orientation, translation, and 3D class. New 3D reference maps are then generated using the particles assigned to each class before the next iteration commences. This iterative process continues until the specified number of cycles is completed. The choice of the number of classes depends on the heterogeneity level in the dataset. Successful classification results in classes with minimal variability, enhancing subsequent refinement steps.

2.5.7 Non-uniform refinement

Non-uniform refinement, a more recent advancement in cryo-EM image processing, is specifically tailored to enhance the refinement of structures with disordered or flexible density (Punjani et al., 2020). By systematically eliminating noise from these regions while preserving the relevant signal for aligning particle images, this algorithm enables substantial improvements in resolution and the overall quality of the 3D map. This approach is particularly advantageous when studying membrane proteins that feature disordered micelles, as these can impede alignment and refinement processes. Non-uniform refinement offers a valuable solution to overcome such challenges and obtain higher-quality reconstructions, providing deeper insights into the structural characteristics of complex macromolecules.

Cryo-electron microscopy has experienced remarkable advancements in the past decade, establishing itself as a formidable tool for elucidating biological structures. It offers the capability to solve macromolecular complexes through two distinct approaches: fitting known structures into low-resolution maps and generating novel high-resolution reconstructions. This versatility has positioned cryo-EM as a powerful technique with wide-ranging applications in structural biology.

Chapter 3

3. Materials and Methods

3.1 Introduction

This chapter details the materials, general protocols and methods used to conduct the molecular biology, protein expression, protein purification and structural experiments used to characterise Kir7.1 and disease-associated variants. If not otherwise stated, materials were obtained from Sigma Aldrich.

3.2 Molecular biology

3.2.1 Plasmid design

In this study, we designed plasmids to express two variants of Kir7.1: the synthetic wild type Kir7.1 and a Kir7.1-KirBac1.3 chimera. The DNA for both proteins were obtained from GENEWIZ.

For the expression of these channels in different cell types, we employed two distinct plasmids: pET-15b for expression in *Escherichia coli* (*E. coli*) and pBAcmam for expression in HEK293 cells.

3.2.1.1 pET-15b plasmid

The synthetic wild type Kir7.1 and Kir7.1-KirBac1.3 chimera DNA sequences were cloned into the pET-15b vector. This plasmid enables protein expression in *E. coli*. The resulting proteins produced from this plasmid carried an N-terminal 6x-His tag and a thrombin cleavage site.

3.2.1.2 pBAcmam plasmid

The synthetic wild type Kir7.1 and Kir7.1-KirBac1.3 chimera DNA sequences were also cloned into the pBAcmam vector. This plasmid is suitable for protein expression in HEK293 cells. The resulting proteins produced from this plasmid were tagged with an N-terminal FLAG tag and a C-terminal GFP tag. Additionally, a 10x-His tag was present at the C-terminus. Between the Kir7.1 sequence and the GFP tag, a TEV cleavage site was included, providing a means to remove the GFP tag if desired.

3.2.2 Media and agar plate preparation

Luria-Bertani (LB) media powder (25 g) was dissolved in distilled water (1 L) to prepare the LB medium. Media were autoclaved at 121 °C, 15 psi for 15 minutes to sterilise before use. Ampicillin was added to the media to reach a concentration of 100 μg/mL (Melford).

LB agar plates were prepared by dissolving 5 g of LB agar powder in distilled water (200 mL) and sterilised as described above. When the solution was hand hot, ampicillin was added at 100 μg/mL. The solution (20 mL) was poured into a sterile plastic petri dish and dried in a sterile environment.

3.2.3 Transformation of plasmid DNA into *E. coli*

New England Biosciences® 5-alpha Competent *E. coli* cells (50 μL) were thawed on ice. A total of 1-100 ng of plasmid DNA was introduced to the cells, followed by a 30-minute incubation on ice and subsequent heat shock at 42 °C for 30 seconds. Cells were returned to ice for 5 minutes before the addition of 950 μL of SOC media. The cell suspension was incubated at 37 °C, 220 rpm for 1 hour. 50-100 μL of cell suspension was spread on LB agar plates in sterile conditions and incubated at 37 °C overnight. One colony was used to inoculate LB media in sufficient quantity for plasmid production.

3.2.4 Plasmid DNA purification

Depending on the application, different scales of plasmid preps were carried out. For 10 mL cultures, the Wizard™ Plus SV Minipreps DNA Purification System (Promega, UK) protocol was followed, providing sufficient DNA for sequencing and further plasmid amplification.

For 25 mL cultures, the QIAGEN® Plasmid Plus Midi Kit protocol was used, yielding up to 100 μg of DNA suitable for small-scale transient transfection experiments.

To purify large amounts of plasmid DNA from 2.4 L of culture, either the PureLink™ HiPure Expi Plasmid Gigaprep Kit (Invitrogen) or the GenElute™ HP Select Plasmid Gigaprep Kit was employed. The protocol for each kit was followed as recommended by the manufacturer.

3.2.5 DNA gel electrophoresis

1 % agarose was prepared in 40 mM tris, 20 mM acetic acid and 1 mM EDTA (TAE) buffer and heated to dissolve. Once cooled, SybrSafe DNA gel stain (Thermo Fisher Scientific) was added. The gel was prepared using either large or small combs, depending on the volume of the samples. 80 V was applied for 80 minutes, and the gel was visualised under ultraviolet illumination.

3.2.6 Site-directed mutagenesis

PCR was employed for site-directed mutagenesis, where custom primers were strategically designed to encompass the intended base change. The mutations were introduced using the Q5® Site-directed mutagenesis kit (New England Biolabs). The NEBaseChanger tool was utilised to create the relevant primers and the recommended Ta was applied for the PCR reaction (**Table 3.1**). The Q5 site-directed mutagenesis protocol was carried out as per the manufacturer's protocol (**Tables 3.2 and 3.3**). This method was also used to introduce truncations at the N- and C-termini of the protein.

Mutation	References	Disease	Forward	Reverse	Ta
T153I	**Toms et al. 2019**	LCA	AGCCTTCATCATT GGCGCCTTCGTG	TCCAGCATCAGTCCGAGC	63
R166*	**Sergouniotis et al. 2011**		GCCCAAGAATTAA GCCTTTAGCATTAG	CTAGCGATCT TGGCCACG	64
L241P			CATTTTCCCTCCC ACCTATTACCACAG	AAGAAGGGA CACTCGTCG	61
W53*	**Pattnaik et al. 2015**		GGACATGAGGTAG	ATGAGGATTCC CCAAGCAT	64

			AGGTGGATGA		
S105I	**Perez-Roustit et al. 2017**		GTACATCACAATC TTCACCGCTG	TTGACGCAGA TGGTATGG	59
Q219*			AAAGCTGTACTGA ACCAGCGTGG	CCGTTTTCCCTCTCTTGG	60
R162W	**Hejtmancik et al. 2008 Lee et al. 2003**	SVD	CAAGATCGCTTGGCCC AAGAATAGAGCCTTTAG	GCCACGAAGGCGCCGGTG	72
I120T	**Khan et al. 2015**	Other vitreoretinal dystrophy	ACAGCTGACAACC GGCTACGGCAC	GTCTCCAGAGAGAAGGAG	61

Table 3.1. Kir7.1 disease mutations and the Q5 site-directed mutagenesis PCR primers used. The recommended annealing temperatures (Ta) were calculated using the NEBaseChanger tool and were employed for PCR reactions. Forward and reverse primers are included.

Components	Final Concentration
Plasmid template	1-10 ng
Forward primer	10 μM
Reverse primer	10 μM
Q5® Hot start high-fidelity 2x master mix	12.5 μL
Nuclease-free water	Up to 12.5 μL

Table 3.2. Contents used for Q5 site-directed mutagenesis. Protocol supplied by the manufacturer was followed.

PCR Parameters
Number of cycles 25
Initial denaturation 98 °C for 30 sec
Denaturation 98 °C for 10 sec
Annealing Ta °C for 20-30 sec
Extension 72 °C for 4 min 24 sec
Final extension 72 °C for 2 min

Table 3.3. Q5 site-directed mutagenesis PCR parameters. Conditions used for PCR to introduce mutations into Kir7.1. The recommended Ta for each mutant was used for the annealing step.

3.2.7 DNA sequencing

To confirm the accuracy of the site-directed mutagenesis reactions, DNA sequencing was performed. The sequencing reactions were carried out by GATC (Eurofins Genomics), and the obtained sequencing results were analysed using the ExPASy translate tool and the EMBOSS needle pairwise sequence alignment (Gasteiger et al., 2003; Madeira et al., 2022).

3.3 Protein expression

3.3.1 Expression of Kir7.1 in *E. coli*

3.3.1.1 Small-scale expression trials

For small-scale expression trials, *E. coli* C41(DE3) cells (New England Biolabs) were utilised to express both WT and chimeric constructs. Protein expression was conducted in 10 mL of LB media supplemented with 100 µg/mL ampicillin. Cells were cultured at 37 °C until reaching an optical density of approximately 0.8 (measured at a wavelength of 600 nm). At this point, 0.5 µM of Isopropyl ß-D-1-

thiogalactopyranoside (IPTG, Generon) was added to induce expression. The cells were harvested under four distinct growth conditions: 4 hours at 37 °C, 5 hours at 30 °C, overnight incubation at 25 °C, and overnight incubation at 18 °C. After harvesting, the cells were frozen at -80 °C.

3.3.1.2 Large-scale expression

For large-scale expression, *E. coli* cells were transformed and used to inoculate 6.4 litres of LB medium, supplemented with 100 µg/mL ampicillin. The cells were cultivated in shaker flasks at 37 °C until reaching an optical density of approximately 0.8 (measured at a wavelength of 600 nm). Following this, the temperature was lowered to 30 °C, and 0.5 µM of IPTG was added to induce expression. After a 5-hour induction period, the cells were harvested.

3.3.2 Expression of Kir7.1 in HEK293 cells

Expi293F™ cells (Thermo Fisher Scientific) were maintained in FreeStyle™ 293 Expression Medium (Thermo Fisher Scientific) at 37 ℃, 8 % CO^2, 120 rpm in a 25-mm shaking diameter incubator. Once the cell density reached 4 $x10^6$ cells/mL, they were diluted to a density of 0.4 $x10^6$ cells/mL. Initial small-scale experiments were conducted using expi293F and expi293F GnTI- cells. All further experiments were conducted using expi293F cells. Expi293F cells are described as HEK293 cells or expi293 cells throughout this thesis.

To achieve protein expression, expi293F cells were cultured and transiently transfected using the ExpiFectamine™ 293 Transfection Kit (Thermo Fisher Scientific) when the cell density reached 3 $x10^6$ cells/mL. The protocol provided by the manufacturer was followed, including the addition of enhancer 1 and enhancer 2 on the morning following transfection. After 48 hours at 37 °C, cells were harvested by centrifugation at 500 x *g* for 10 minutes. Pellets were frozen at -80 ℃. For small-scale experiments, 24-well culture plates were used with 3 mL cell culture per well. Large-scale experiments were conducted in various quantities from 1-12 L.

3.4 Protein purification

3.4.1 *E. coli* small-scale purification

Cells were lysed with 400 µL of 20 mM Tris-HCl pH 7.5, 150 mM KCl, 10 mM imidazole (IMZ), 1% v/v Tween-20, 0.075 mg DNAse I (Roche), protease inhibitor cocktail (Roche), and 0.5 mg lysozyme. After incubation at 4 °C with agitation for 15 minutes, 1.2% n-dodecyl β-D-maltoside (DDM) (Solgrade, Anatrace) was added and samples were rotated for 1 hour at 4 ℃. Insoluble material was removed by centrifugation at 17,000 x *g* for 10 minutes. The supernatant was analysed for protein expression by SDS-PAGE and western blotting. Optimal constructs and conditions were investigated further in large-scale purification.

3.4.2 *E. coli* large-scale purification

The cells were resuspended in lysis buffer using a hand-held homogeniser and further lysed utilising the EmulsiFlex C3 homogeniser (ATA Scientific). Lysis was performed by passing the mixture through the homogeniser a minimum of three times, applying a minimum pressure of 15,000 pounds per square inch (psi). The lysate was centrifuged at 10,000 x *g* for 30 minutes to remove the cell debris. The membrane fraction was separated by centrifugation at 131,790 x *g* for two hours. Membranes were frozen at -20 °C and thawed when needed. Thawed membranes were solubilised in 20 mM Tris, 150 mM KCl, 20 mM imidazole, 1 % DDM, pH 7.5 and either incubated with nickel resin (Qiagen) overnight or loaded onto a 1 mL HisTrap HP column (GE Healthcare) for 1 hour. Nickel resin was washed with 20 mM Tris, 150 mM KCl, 1% DDM, pH 7.5 and IMZ from 0 mM -100 mM to remove weaker, non-specifically bound proteins. 100 mM - 500 mM IMZ was used to elute the protein of interest. The Histrap column was washed with 20 mM Tris, 150 mM KCl, 20 mM imidazole, 1 % DDM, pH 7.5 and the protein was eluted using 0 mM - 500 mM IMZ over a linear gradient. Eluted fractions were analysed by SDS-PAGE and western blot using both an anti-His monoclonal antibody and a polyclonal Kir7.1 antibody (Thermo Fisher Scientific) (**Table 3.5**). Where applicable, fractions were concentrated, and a final size exclusion chromatography step was applied using a Superdex 200 increase 10/300 column (GE Healthcare Life Sciences). Protein was frozen at -80 °C.

3.4.3 Materials used for HEK293 purification

Mammalian small-scale expression	NP-40 lysis buffer	10 mM Tris	10 mM NaCl	3 mM $MgCl_2$	0.5 % NP-40	pH 7.5	
	Pull-down lysis buffer	20 mM Tris	1 % DDM	150 mM KCl	1 mM β-mercapto-ethanol	pH 7.5	
	Small-scale wash buffer	20 mM Tris	0.15 % DDM	150 mM KCl	1 mM β-mercapto-ethanol	pH 7.5	
	Small-scale elution buffer	20 mM Tris	0.15 % DDM	150 mM KCl	1 mM β-mercapto-ethanol	0.2 g/mL FLAG Peptide	pH 7.5
Mammalian large-scale	Solubilisation buffer	20 mM Tris	1 % GDN	150 mM KCl	pH 7.5		
	Purification buffer	20 mM Tris	0.02 % GDN	150 mM KCl	pH 7.5		
	ATP wash buffer	20 mM Tris	0.02 % GDN	150 mM KCl	20 mM $MgCl_2$	2 mM ATP	pH 7.5
	Elution buffer	20 mM Tris	0.02 % GDN	150 mM KCl	0.2 mg/mL FLAG peptide	pH 7.5	
	SEC buffer	20 mM Tris	0.02 % GDN	150 mM KCl	pH 7.5		

Table 3.4. Buffers used in protein purification from HEK293 cells.

3.4.4 HEK293 small-scale purification

Kir7.1 was expressed in expi293F and expi293F GnTI- cells. 3 mL of cells were transfected in triplicate in a 24-well format evaluating several conditions including, cell type, temperature, and length of expression. Cells were grown at 30 °C or 37 °C and harvested after 48 hours or 72 hours.

Cells were resuspended in 150 µL NP-40 lysis buffer and rotated at 4 °C. After one hour of incubation, samples were centrifuged at 17,000 x *g* for 45 minutes. The supernatant was removed and analysed by western blot.

The second sample of the triplicate was resuspended in 1 mL of pull-down lysis buffer and incubated at 4 °C for 1 hour. Samples were centrifuged at 17,000 x *g* for 45 minutes. A sample of the supernatant was taken at this point for analysis by western blot. The remaining supernatant was incubated with 100 µL of ANTI-FLAG M2 affinity resin at 4 °C overnight. The sample was transferred to a micro bio-spin chromatography column (Bio-Rad) and the unbound fraction was removed by gravity flow. The column was washed with small-scale wash buffer for 30 column volumes. The final wash step was centrifuged at 200 x *g* to remove any remaining wash buffer. The sample was eluted by the addition of the small-scale elution buffer and centrifuged at 200 x *g*.

3.4.5 HEK293 large-scale purification

Cell pellets were resuspended in solubilisation buffer with protease inhibitor cocktail (Roche) and DNAse I. Two hours after solubilisation, lysed cells were centrifuged at 131,790 x *g* for 45 min to remove the insoluble portion. The supernatant was incubated with ANTI-FLAG M2 affinity resin overnight at 4 °C with gentle mixing. The resin was washed with twenty column volumes of purification buffer and subsequently washed with seven column volumes of ATP wash buffer. The protein was eluted with five column volumes of elution buffer and digested with TEV protease at 4 °C overnight to remove the C-terminal GFP-His_{10} tag. Following cleavage, 20 mM imidazole was added to the protein and the sample was incubated with Ni-NTa resin (Qiagen) for 1 hour at 4 °C with gentle agitation. Using a gravity column, the flow-through was collected and further purification was performed on a Superose 6 Increase 10/300 gel filtration column (GE Healthcare Life Sciences) in

purification buffer. Peak fractions containing protein were concentrated to ~6 mg/mL and either used immediately or flash-frozen in liquid nitrogen and stored at - 80 °C.

3.5 Analysis methods

3.5.1 SDS-PAGE

Protein sample composition and purity was analysed by SDS-PAGE. Protein samples were denatured using NuPAGE™ LDS sample buffer (Thermo Fisher Scientific). Samples were then loaded onto NuPAGE Bis-Tris precast 4-12% polyacrylamide gels (Thermo Fisher Scientific), soaked with NuPAGE MOPS SDS running buffer (Thermo Fisher Scientific), and separated by electrophoresis until the dye front ran out of the gel. The PageRuler™ Prestained Protein Ladder (Thermo Fisher Scientific) was run alongside protein samples for size reference. The protein was visualised by staining the gels with InstantBlue™ Coomassie Stain (Abcam).

3.5.2 Western blotting

Western blotting was performed to identify specific protein bands on the SDS-PAGE gels. Following the separation of protein samples by size using SDS-PAGE, they were transferred onto a polyvinylidene fluoride (PVDF) membrane (Thermo Fisher Scientific) using the iBlot™ 2 gel transfer device (Thermo Fisher Scientific). The transfer was conducted at 20 V for 1 minute, followed by 23 V for 4 minutes and 25 V for 2 minutes. Unspecific antibody binding to the membrane was prevented by blocking the membrane with 5 % semi-skimmed milk powder solution in TBS + 0.1 % Tween 20 (TBST) for 1 hour at room temperature. The membrane was then incubated with a Kir7.1 polyclonal antibody (Thermo Fisher Scientific) diluted in 5 % milk in TBST at 4 °C overnight (**Table 3.5**). Five 10-minute washes with TBST were conducted followed by incubation with the secondary antibody for 1 hour at room temperature. Subsequently, five 10-minute washes with TBST were carried out. The western blot was revealed by either applying ECL western blot detection reagent (Thermo Fisher Scientific) and imaging with a Chemi-Doc imager (Bio-Rad) or by the addition of SIGMAFAST™ 3,3’ -diaminobenzidine (DAB) tablets in 5 mL distilled water and imaged by eye.

Antibody target	Antibody	Concentration	Source
His-tag	Anti-polyHistidine−Peroxidase antibody, Mouse monoclonal	1:2000	Sigma Aldrich A7058
Kir7.1 residues 160-360	Rabbit anti-mouse/human IgG	1:1000	Thermo Fisher Scientific # PA5-109875
Rabbit IgG	Goat anti-Rabbit IgG (H+L) secondary antibody, HRP	1:10000	Thermo Fisher Scientific #31460

Table 3.5. Antibodies used in western blot detection.

3.6 Biophysical analysis

3.6.1 Nanoscale differential scanning fluorimetry

The Prometheus Panta (NanoTemper Technologies) was used to determine the melting temperature of protein samples. 0.4 mg/mL of protein was loaded into nanoDSF grade standard capillaries (NanoTemper Technologies). A temperature gradient of 1 °C per minute from 25 °C to 95 °C was applied and the intrinsic protein fluorescence at 330 and 350 nm was recorded. The fluorescence intensity ratio and its first derivative were calculated with the manufacturer's software (PR. ThermControl).

3.6.2 Detergent thermal stability screening

25 mL of expi293F cells were used to express WT Kir7.1 protein for 48 hours at 37 °C. The cell pellet was reconstituted in 1.5 mL of HEPES buffer (pH 7.5) containing 200 mM NaCl and cOmplete™ mini protease inhibitor (Roche). A total of 90 µL of cells were dispensed into each well of a 96-well plate, followed by the addition of 10 µL of a 10 % detergent stock to each well. The following detergents were used:

NDM, DM, DDM, TDM, OGNG, LMNG, Cy5, Cy7, GDN and FC12. 1 % CHS was added to all detergent stocks except GDN. This gave a final concentration of 1 % detergent and 0.1 % CHS. Samples were incubated with detergent for 2 hours on a shaker platform at 500 rpm. Cell debris was removed by spinning samples at 17,000 x *g* for 10 minutes.

The supernatant was carefully transferred to a fresh plate. The lysate was incubated on ice for 1 hour with 1 nM of pico-RED dye from NanoTemper, which was prepared as a 250 µM stock in buffer. Thermal unfolding was measured using the Andromeda machinery (NanoTemper Technologies).

3.7 Electron Microscopy

3.7.1 Negative stain EM

CF-300 grids with an amorphous carbon support layer were glow discharged at 30 mA for 60 seconds using a Pelco easiGlow system (Ted Pella, Inc). Three microlitres of sample was applied to grids and allowed to absorb for 30 seconds. The grid was submerged in distilled water for five seconds twice followed by 2 % uranyl acetate for five seconds and thirty seconds. Excess solution was blotted, and the grid was left to air dry. Negative stain images were collected on a Tecnai T12 operated at 120 keV (Thermo Fisher Scientific).

3.7.2 Cryo-EM sample preparation

For this thesis, a total of eight cryo-EM data sets were collected. These were: (**1**) Initial-apo-Kir7.1, (**2** and **3**) Initial-apo-Kir7.1-GO, (**4** and **5**) Kir7.1-PIP_2, (**6** and **7**) Apo Kir7.1, (**8**) Kir7.1-R162W.

3.7.2.1 Initial cryo-EM work

Three initial cryo-EM data sets were collected investigating Kir7.1. Sample preparation and data collection was conducted by Dr. Natasha Lukoyanova. One data set used unsupported ice and two data sets were collected on graphene oxide supported ice.

C-Flat R2.0/2.0 grids were glow discharged at 30 mA for 60 seconds using a Pelco easiGlow system. A monolayer of graphene oxide was added as previously described (Esmaeili et al., 2020). 3 µL of Kir7.1 (0.2 mg/mL) was pipetted onto the grids and

waited 20 seconds before blotting for 20 seconds. For unsupported ice, no graphene oxide was added and 3 µL of 0.5 mg/mL Kir7.1 was pipetted onto grids and immediately blotted for 10-12 seconds.

3.7.2.2 Optimised cryo-EM work

Samples of Kir7.1 were defrosted and centrifuged at 100,000 x *g* at 4 °C to remove any aggregation. For samples investigating PIP_2 binding, C8-PIP_2 was added to Kir7.1 at a final concentration of 1 mM (Echelon Biosciences). This was incubated for ~30 minutes before vitrification. Prior to sample application, grids were plasma treated for 45 seconds at high (Harrick Plasma Cleaner PDC-32G-2). A protein sample of 3.5 µL, either at a concentration of 6.6 mg/mL or 7 mg/mL, was pipetted onto Quantifoil R1.2/1.3 300 mesh Au grids (Agar Scientific). The grids were then blotted for 4 seconds at 4 °C with a blotting force of 0, followed by plunge-freezing in liquid ethane using a Vitrobot Mark IV. Grids were stored in liquid nitrogen.

3.7.3 Data collection

Grids were initially screened by acquiring images on a Tecnai T12 operated at 120 keV (Thermo Fisher Scientific). Subsequent grid screening was conducted using a Titan Krios microscope using the EPU software. The grid support, protein concentration and Vitrobot parameters were assessed by particle distribution and ice thickness. Optimised conditions were subsequently used to generate grids that were used directly for data collection. Movies of Kir7.1 with and without the addition of PIP_2 were collected at Birkbeck College, Institute of Structural and Molecular Biology by Dr Natalya Lukoyanova. The imaging parameters used for the movie collections are found in **Tables 3.6, 3.7 and 3.8**.

Sample	Initial Apo Kir7.1	Initial Apo Kir7.1 (graphene oxide supported)	Initial Apo Kir7.1 (graphene oxide supported)
Microscope	FEI Titan Krios	FEI Titan Krios	FEI Titan Krios
Acceleration voltage (kV)	300	300	300
Camera	K3 detector with BioQuantum energy filter	K3 detector with BioQuantum energy filter	K3 detector with BioQuantum energy filter
Energy filter slit width (eV)	20	20	20
Pixel size (Å)	0.325	0.325	0.325
Frames/movie	50	50	50
Total dose (e^-/Å)	28.17	27.9	27.69
Defocus range (μM)	1.5 - 3	1.5 - 3	1.5 - 2.7
Number of movies	6034	7119	11664

Table 3.6. Data collection parameters used for data acquisition of initial Kir7.1 samples.

Sample	Apo Kir7.1_1	Apo Kir7.1_2	Kir7.1-PIP_2_1	Kir7.1-PIP_2_2
Microscope	FEI Titan Krios	FEI Titan Krios	FEI Titan Krios	FEI Titan Krios
Acceleration voltage (kV)	300	300	300	300
Camera	K3 detector with BioQuantum energy filter	K3 detector with BioQuantum energy filter	K3 detector with BioQuantum energy filter	K3 detector with BioQuantum energy filter
Energy filter slit width (eV)	10	20	10	20

Pixel size (Å)	0.65	0.65	0.65	0.65
Frames/movie	50	50	50	50
Total dose (e^-/Å)	29.11	31.9	29.11	31.9
Defocus range (μM)	1.5 -2.7	1.2 - 2.7	1.5 - 2.7	1.2 - 2.7
Number of movies	12558	22098	13312	23114

Table 3.7. Data collection parameters used for data acquisition of optimised Kir7.1 samples with and without the addition of PIP_2.

Sample	Kir7.1 - R162W
Microscope	FEI Titan Krios
Acceleration voltage (kV)	300
Camera	K3 detector with BioQuantum energy filter
Energy filter slit width (eV)	20
Pixel size (Å)	0.65
Frames/movie	50
Total dose (e^-/Å)	31.89
Defocus range (μM)	1.2 - 2.4
Number of movies	23110

Table 3.8. Data collection parameters used for data acquisition of Kir7.1-R162W.

3.7.4 Image processing

The overall image processing strategy, including the programmes used, was similar between data sets and is fully explained in the relevant chapters.

All data sets were collected in super-resolution mode with a Gatan K3 camera and movies were downsampled by a factor of 2. Down-sampled movies were imported into cryoSPARC (Punjani et al., 2017) and corrected for global and beam-induced motion using patch-based motion correction. The motion-corrected micrographs were used to estimate the CTF parameters by patch-based CTF estimation. Micrographs with a maximum resolution estimation exceeding 6-8 Å were excluded. Initially, particle selection was performed using the blob picker, followed by the application of the template picker once high-quality 2D classes had been established. Particles were extracted from micrographs within 400-pixel boxes and subsequently binned by a factor of 2, resulting in 200-pixel boxes. These particles then underwent reference-free 2D classification, where those originating from featureless, noisy, or poorly resolved classes were excluded. The selected high-quality 2D classes were employed for *ab initio* reconstruction, leading to the generation of a consensus map. Subsequent heterogeneous refinement was carried out with 4 classes, using the consensus map and three poorly resolved maps to separate any remaining 'bad' particles. Non-uniform refinement was used to improve the consensus map. These two jobs were carried out iteratively until no more 'bad' particles remained and the consensus map was at the best resolution. At this point, C4 symmetry was applied. Particles were re-extracted in 440 pixels without binning. 3D variability analysis was carried out on each data set to evaluate flexibility within the protein and results were analysed in simple, cluster and intermediate mode. Using UCSF Chimera, three masks were generated to encompass either the transmembrane domain, the cytoplasmic domain, or the whole protein excluding the micelle (Pettersen et al., 2004). Local refinement with C4 symmetry was used with each of these masks but no significant improvement was observed. Local resolution estimation was calculated on cryoSPARC, and this was used to colour the EM map by local resolution. Maps were sharpened using DeepEMhancer for visualisation and manual fitting (Sanchez-Garcia et al., 2021).

3.7.5 Model building

The final EM maps were locally sharpened using the autosharpen tool in Phenix (Liebschner et al., 2019). ModelAngelo was used to generate starting structures using the Kir7.1 amino acid sequence and the EM sharpened maps (Kiarash Jamali, Dari Kimanius, 2023). ModelAngelo produced a model that fit most areas of the EM density and Coot was used for manual building of flexible regions (Emsley et al., 2010). Maps and models were loaded into ChimeraX (Pettersen et al., 2021) and associated using the tool in the Isolde GUI (Croll, 2018). Hydrogens were incorporated using the "addh" command. Initial validation involved the use of the clashes validation tool to systematically address challenging residues. This was achieved by simulating small regions and adjusting the model to match the surrounding density. Subsequently, the live Ramachandran plot was used to identify residues with unfavourable torsional angles, which were then corrected manually. Lastly, a similar iterative approach was employed to address instances of rotamer outliers.

Models were refined using real-space refinement in Phenix with default settings (secondary structure restraints, Ramachandran restraints, rotamer restraints and refinement of B-factors) (Liebschner et al., 2019). Map-model FSC and map quality were assessed using the cryo-EM validation tools in Phenix and Molprobity (Williams et al., 2018). Figures of cryo-EM maps and atomic models were generated using UCSF Chimera (Pettersen et al., 2004) and ChimeraX (Pettersen et al., 2021).

For the sample with PIP_2 present, unmodeled blobs were detected in Coot, and C8-PIP_2 (ligand code: PIO) was placed in the density at one ligand per subunit. The acyl chains were deleted until only the portion of PIP_2 within the density remained. Phenix eLBOW was used to generate ligand restraints.

Chapter 4

4. Expression and purification of human Kir7.1

The first aim of this research was to establish a protocol for the expression and purification of human Kir7.1. This protein had not been studied in the Wallace group previously, so all conditions had to be considered. Firstly, extensive molecular biology was conducted to generate a construct library with varying degrees of N and C terminal truncations. These truncations aim to remove regions of disorder in an attempt to improve expression levels. In addition to the human Kir7.1 protein, a bacterial-human chimeric protein was investigated. A Kir7.1- KirBac1.3 chimera was designed and created to encompass the bacterial transmembrane domain from KirBac1.3 and the cytoplasmic domain from human Kir7.1. All constructs were subjected to small-scale expression tests in *E. coli* and/or HEK293 cells. Full-length human Kir7.1 expressed in HEK293 cells was selected from these initial trials and protein purification was optimised. This was an extensive process involving several adjustments and improvements, including detergent screening, contaminant removal and tag cleavage. Overcoming these challenges resulted in a final protocol capable of producing sufficient quality and quantity of Kir7.1 for downstream structural and biophysical studies.

This chapter will outline the results from cloning, expressing, and purifying WT Kir7.1 and Kir7.1-KirBac1.3 chimera.

4.1 Production of Kir7.1-KirBac1.3 chimeric channel

To aid recombinant expression, a chimeric protein was designed to incorporate a region of prokaryotic sequence into the human protein. KirBac channels are prokaryotic homologs of mammalian Kir channels from *Burkholderia pseudomallei.* The chimera construct incorporates the prokaryotic sequence derived from KirBac1.3, which encodes the extracellular portion of the transmembrane domain. (**Fig. 4.1**). The remainder of the transmembrane domain and the entire cytoplasmic domain consists of human Kir7.1 (**Fig. 4.1**). The human component of the chimera includes the regulatory surfaces through which the channel is modulated by PIP_2 and where many disease-causing mutations are located.

Several Kir channel structures have been solved, but no full-length eukaryotic channel structures have been determined using an *E. coli* expression system (Martin et al., 2017; Tao et al., 2009; Whorton and MacKinnon, 2011). Prokaryotic KirBac channels and the cytoplasmic domain of eukaryotic Kir channels have been successfully expressed in *E. coli* for structural studies (Bavro et al., 2012; Kuo et al., 2003; Nishida and MacKinnon, 2002; Pegan et al., 2005). Human-bacterial chimeras have a proven track record in aiding structural studies of Kir channels (Nishida et al., 2007). Therefore, the strategy implemented involved combining the transmembrane domain of a KirBac channel with the cytoplasmic domain of the human Kir7.1 channel.

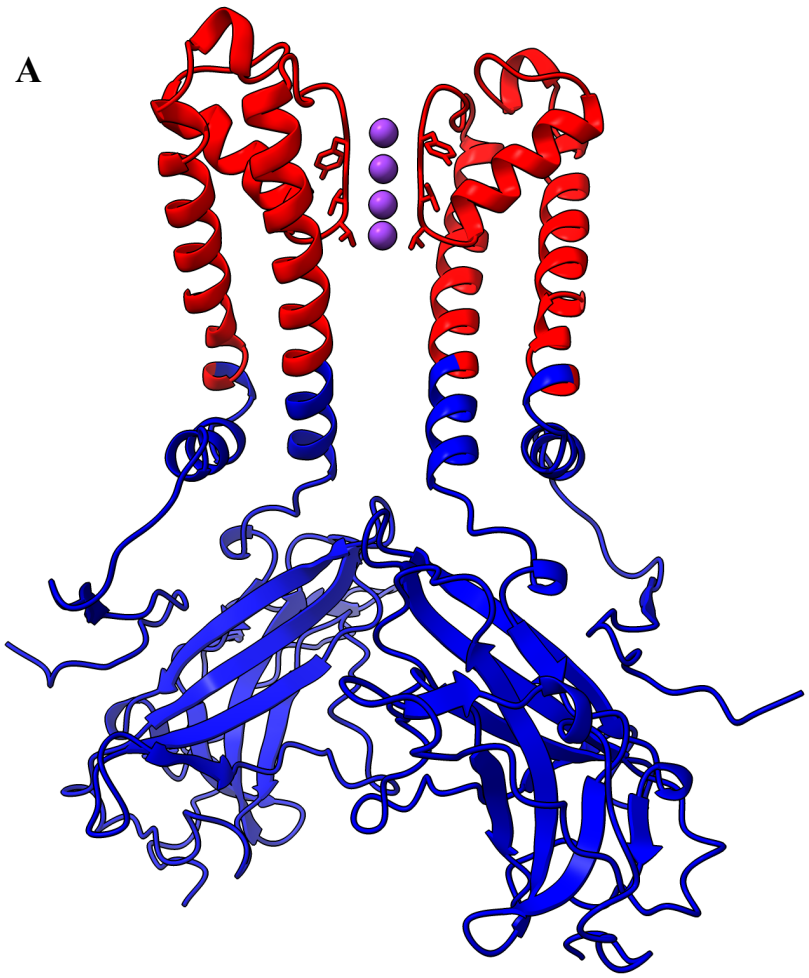

B

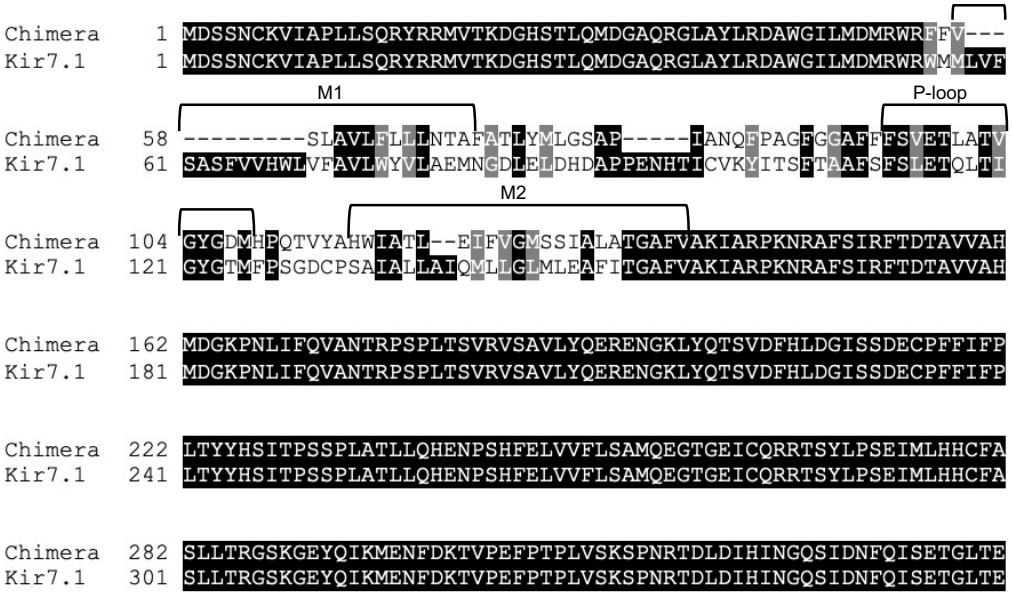

Figure 4.1. Kir7.1-KirBac1.3 chimera.

A. A homology model produced for the Kir7.1-KirBac1.3 chimera based on the crystal structure of Kir3.1-KirBac1.3 (PDB: 2QKS). The sequence corresponding to human Kir7.1 is shown in blue and the KirBac1.3 sequence is shown in red. Four potassium ions are represented by purple spheres in the selectivity filter. Only two out of four subunits are shown. Modelling was performed using SWISS-MODEL, and the image was generated using ChimeraX. **B.** Amino acid sequence alignment of WT Kir7.1 and Kir7.1-KirBac1.3 chimera. Residues shaded in black represent identical amino acids. Transmembrane regions M1, M2 and the P-loop are labelled.

4.2 Expression in *E. coli*

4.2.1 Construct design

WT human Kir7.1 and the Kir7.1-KirBac1.3 chimera were inserted into a pET15b expression vector and constructs were generated with regions of the N- and C-termini deleted. This vector generated constructs with a 6x-Histidine tag and a thrombin cleavage site on the N-terminal of the protein. Successful truncations were confirmed by DNA sequencing and subsequently used for expression in *E. coli* (**Table 4.1**).

Construct name	Residues	Length (amino acids)
Wild type		
Construct WT1	1-360	360
Construct WT2	10-360	350
Construct WT3	1-339	339
Chimera		
Construct C1	1-341	341
Construct C2	10-341	331
Construct C3	1-320	320

Table 4.1. Constructs created for expression in *E. coli.*

Constructs WT1 and C1 represent the full-length version of human Kir7.1 and the chimera, respectively. The residue column notes the starting and ending residue in each construct relative to the full-length sequences. The length column describes the complete number of amino acids.

4.2.2 Small-scale expression trials

All six constructs outlined in **Table 4.1** were expressed in a small-scale format using *E. coli.* The amount of expression was detected and measured by western blot (WB). Each construct was initially expressed in triplicate at 37 °C for four hours. Constructs were subsequently expressed at 30 °C for five hours, 25 °C overnight and 18 °C overnight.

All WT constructs showed either no or very little expression, and this was represented by a faint band on a WB (**Fig. 4.2**). WT1 showed the clearest band at 30 °C, 25 °C and 18 °C but the overall expression level was low (**Fig. 4.2**).

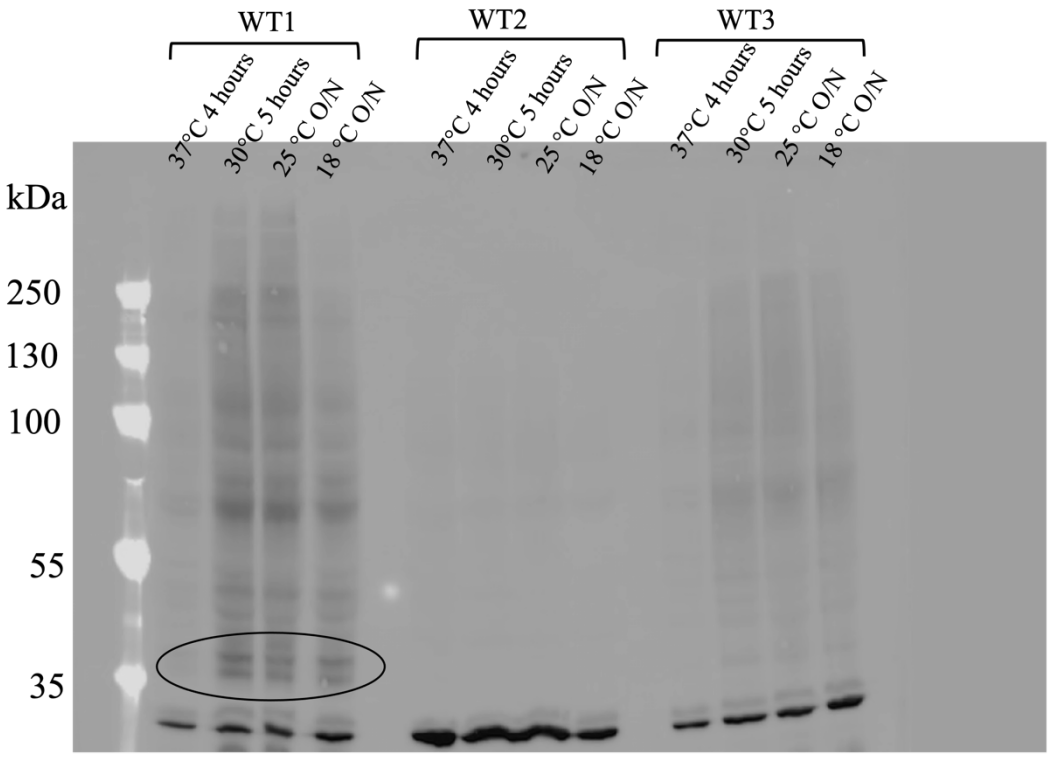

Figure 4.2. Western blot of WT constructs expressed in *E. coli.*

An anti-Kir7.1 antibody was used for detection. The constructs and conditions tested are labelled above the blot and the molecular weight ladder is labelled. The molecular weight of a monomer of Kir7.1 is ~40 kDa and the corresponding protein band is circled in black.

The expression levels of the chimera proteins were more promising, with construct C2 producing the strongest band in the WB (**Fig. 4.3**). Expression at 30 °C for 5 hours achieved the highest level of expression and therefore was used for further investigations. At this point, it was deemed most appropriate to conduct further *E. coli*-based expression experiments with the chimeric C2 construct rather than any WT constructs.

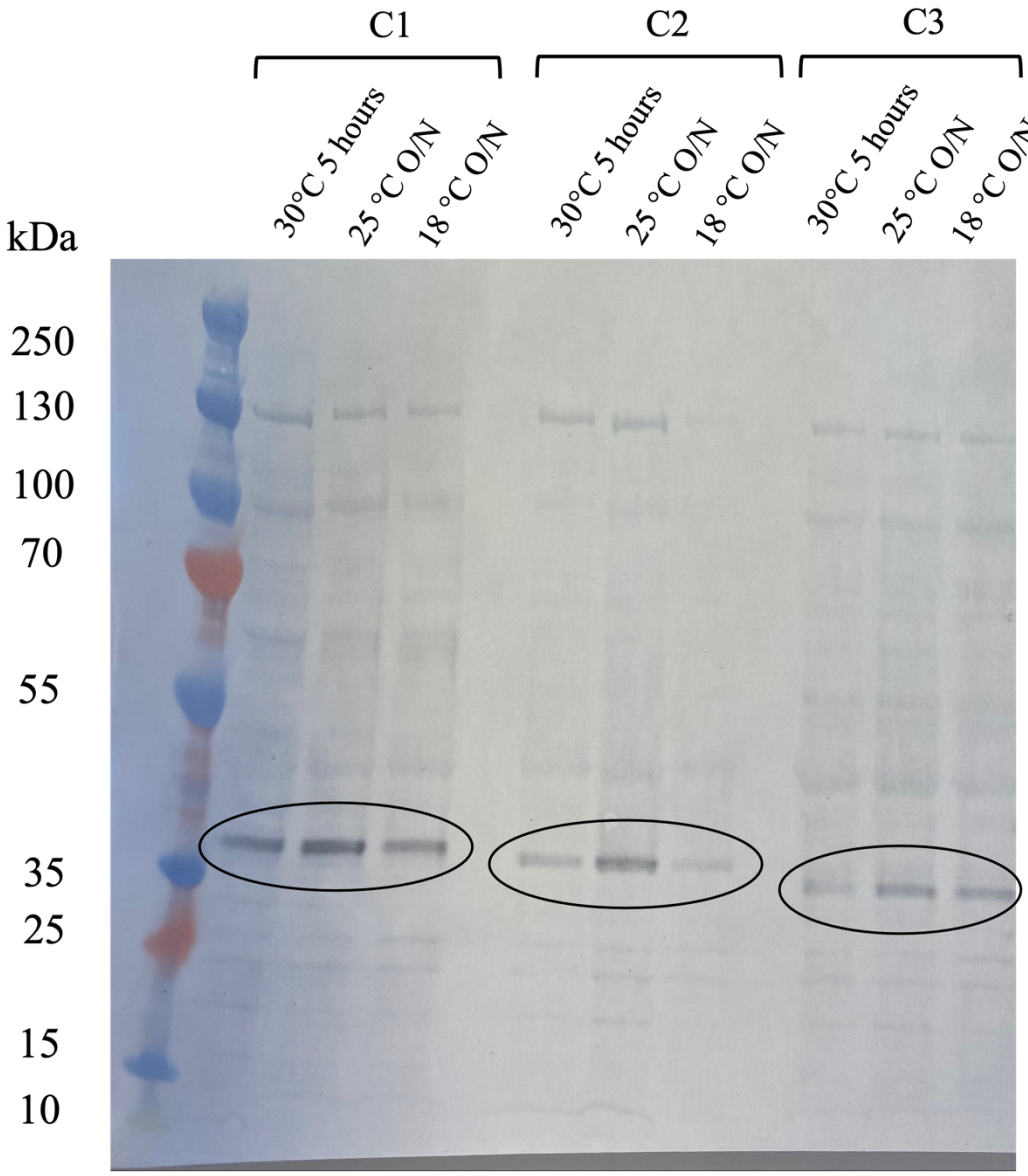

Figure 4.3. Western blot of chimera constructs expressed in *E. coli.*

An anti-His antibody was used for detection. The constructs and conditions tested are labelled above the blot and the molecular weight ladder is labelled. The molecular weight of a monomer of Kir7.1 is ~40kDa and the corresponding protein band is circled in black for each construct.

4.2.3 Construct C2 in large-scale expression trials

Construct C2 was expressed in 6.4 litres at 30 °C for 5 hours. Membranes were split into two batches. One sample was solubilised in 1 % n-dodecyl β-D-maltoside (DDM) and the other was solubilised in 1 % glyco-diosgenin (GDN). Two different detergents were used to investigate the variation in solubilisation and purification of

construct C2 in each. Nickel resin was used to bind the 6x-His tag positioned on the N-terminal of the protein and imidazole was used, in increasing concentrations, to elute the protein. Anti-His WB analysis confirmed the presence of C2 in elution fractions of both DDM and GDN solubilised samples. DDM solubilised a higher quantity of the protein and therefore was concentrated and taken forward to size exclusion chromatography (SEC). SEC and WB analysis showed the presence of C2 in the aggregate peak (peak 1), the tetramer elution peak (peak 2) and the monomer elution peak (peak 3) (**Fig. 4.4**). This demonstrated that a portion of the construct C2 was expressed in tetrameric form, but the amount was very low. From 3.2 litres of *E. coli* cells, the final protein peak is small with the protein undetectable by Coomassie staining on SDS-PAGE. It is possible, with optimisation, that expression of the chimera in *E. coli* could have been achieved to a sufficient level. However, it was decided that protein expression using *E. coli* was not the most viable option for this project.

A

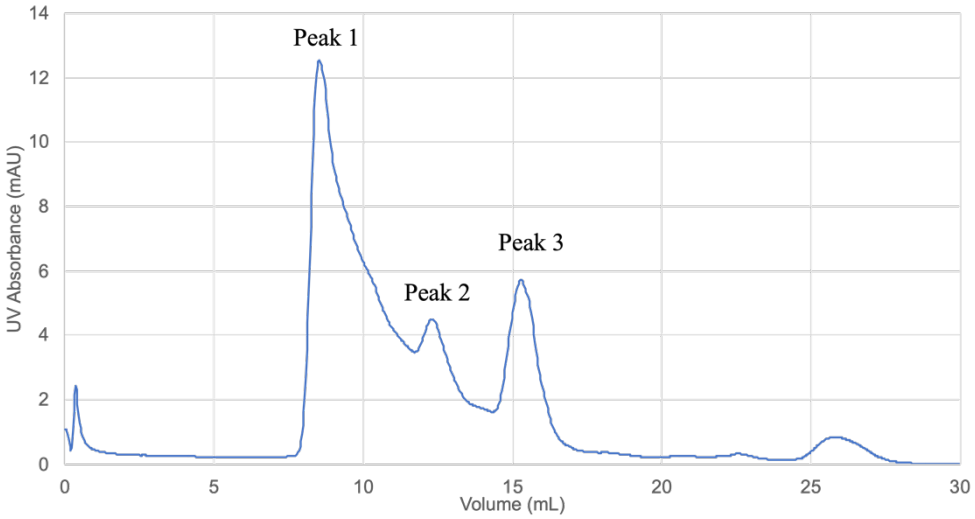

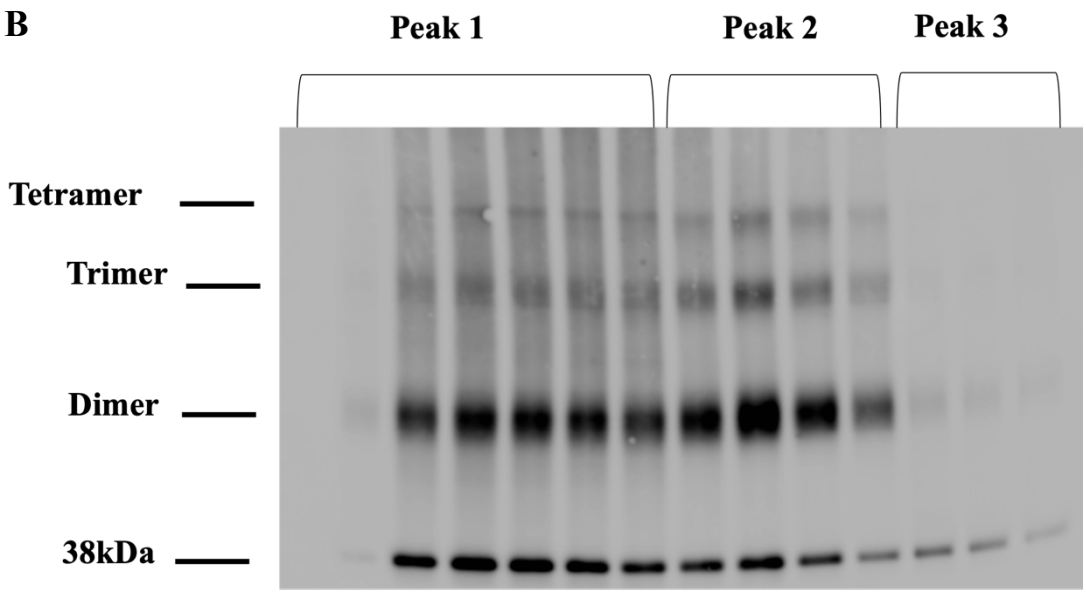

Figure 4.4. Purification of chimeric construct C2.

A. Size exclusion chromatogram of DDM solubilised construct C2. **B.** Western blot analysis of SEC elution fractions using an anti-Kir7.1 polyclonal antibody. Lanes 1-7 investigate the first peak and its shoulder, lanes 8-11 show the second peak and the final 12-14 lanes show the third peak. A 38 kDa band is labelled representing the monomeric protein and corresponding bands are labelled showing possible other oligomeric states of the protein.

4.3 Expression in HEK293 cells

Human embryonic kidney 293 (HEK293) cells are an attractive choice for expressing mammalian membrane proteins in their most native form. Advantages of this system include lipid bilayer composition, protein folding machinery, and post-translational modifications.

The expi293 expression system was chosen for the transient expression of native Kir7.1 and chimeric Kir7.1-KirBac1.3. Expi293F cells are derivatives of the HEK293 cell line selected for their transfection efficiency and productivity (Liu et al., 2008). Additionally, expi293F GnTI- cells lack an N-acetylglucosaminyltransferase, thereby preventing complex glycosylation of proteins. This facilitates the expression of homogenous proteins without varying degrees of glycosylation. Kir7.1 contains a glycosylation site at residue 95, an asparagine that lies in the extracellular turret between the two transmembrane

domains (Carrington et al., 2018). Both expi293F and expi293F GnTI- cells were used for expression trials.

4.3.1 Small-scale expression trials of WT and chimera proteins

The WT and chimera DNA was designed with an N-terminal FLAG tag, a C-terminal TEV cleavage site, a GFP tag, and a 10x-Histidine tag. DNA was inserted into a pBAcmam vector for mammalian cell expression. DNA was inserted into HEK293 cells by transient transfection and initial small-scale expression trials were conducted. Firstly, expi293F cells were investigated at 30 °C and 37 °C for 48 and 72 hours. A 70 kDa protein band, representing the monomeric version of the protein and tags, was identified by SDS-PAGE and WB under all expression conditions, with 37 °C for 48 hours appearing to be the optimal condition (**Fig. 4.5A and C**). Secondly, expi293F GnTI- cells were used for expression of both proteins at 30 °C and 37 °C for 48 and 72 hours. Similar to expi293F cells, a 70 kDa protein band was detected under all conditions (**Fig. 4.5B and C**).

The initial small-scale expression trials indicated successful expression of the WT and chimera proteins under all conditions. As the WT protein showed expression levels similar to the chimera, it was decided that the WT protein would be the sole focus of the project. The optimal expression conditions were found to be expi293F cells at 37 °C for 48 hours.

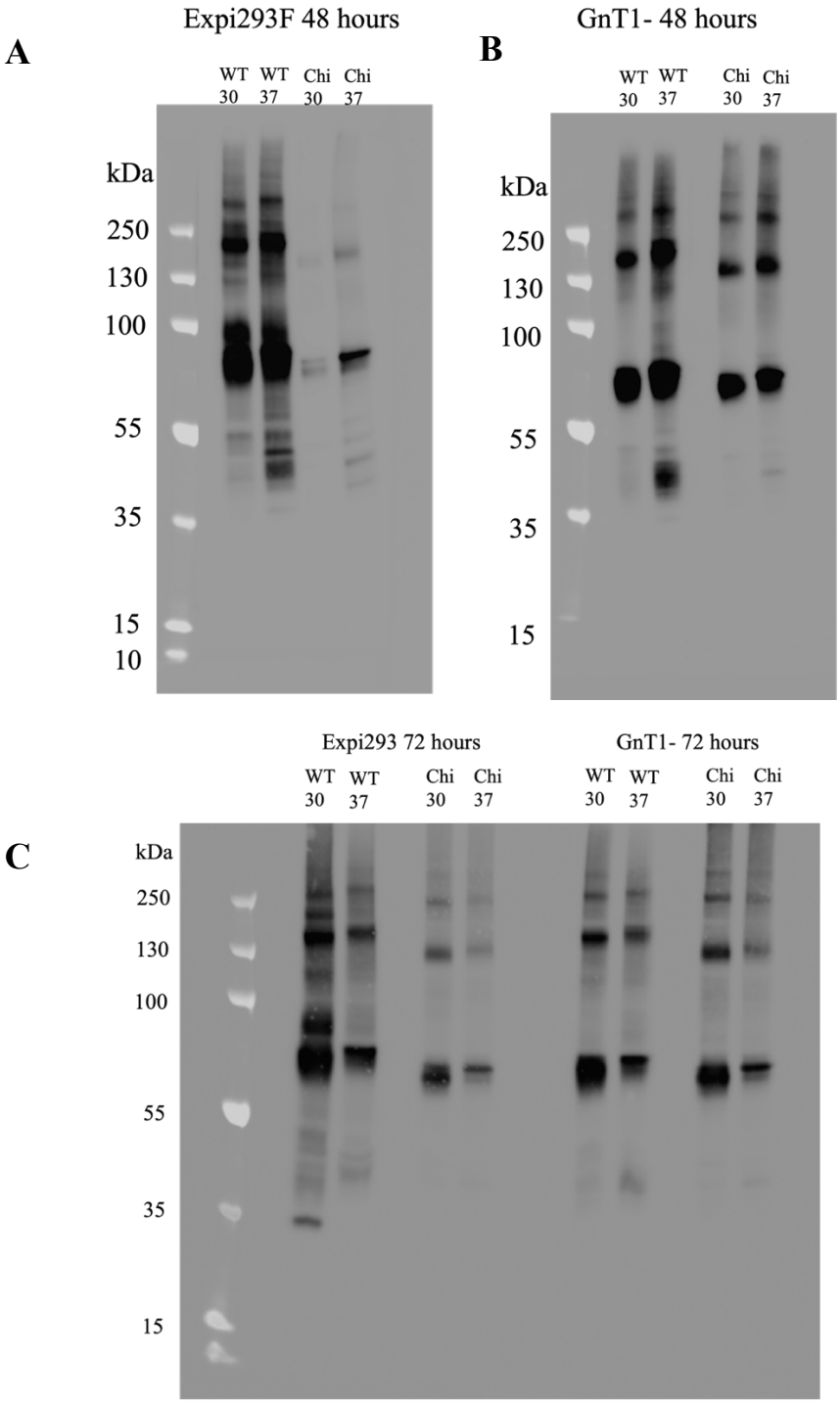

Figure 4.5. Western blots analysis showing expression levels of WT and chimera constructs in mammalian cells.

Expression of WT and chimera proteins in **A.** Expi293F cells for 48 hours, **B.** GnTI- cells for 48 hours, and **C.** Expi293F and GnTI- cells for 72 hours. In all blots, Kir7.1 monomers are present at 70 kDa with higher oligomeric states visible. An anti-Kir7.1 antibody was used for detection.

4.3.2 Construct design of WT Kir7.1

Whilst initial full-length constructs were being evaluated, it was decided to generate a construct library that may aid the expression of WT Kir7.1 in HEK293 cells. An important factor that influences protein expression, stability and structure determination is the degree of disorder and flexibility within the protein. Protein DisOrder prediction (PrDOS) is a web-based tool predicting regions of disorder based on the amino acid sequence of a protein (Ishida and Kinoshita, 2007). Using PrDOS, residues before position 17 and residues after position 333 were classified as disordered (**Fig. 4.6**). The N- and C- termini of WT Kir7.1 were removed at various positions to generate constructs with fewer regions of disorder (**Fig. 4.6**). **Table 4.2** shows the constructs of Kir7.1 designed and created for expression trials in HEK293 cells. All constructs in **Table 4.2** were created and >30 µg DNA was produced for each construct to achieve transient transfection.

Construct Name	Residues	Length (amino acids)
Wild type	1-360	360
Construct A	1-326	326
Construct B	1-339	339
Construct C	1-347	347
Construct D	4-360	356
Construct E	4-326	322
Construct F	4-339	335
Construct G	4-347	343
Construct H	10-360	350
Construct I	10-326	316
Construct J	10-339	329
Construct K	10-347	337
Construct L	14-360	346
Construct M	14-326	312
Construct N	14-339	325

Table 4.2. Constructs of Kir7.1 created for expression in HEK293 cells.

The starting and ending residue numbers are shown relative to the wild type Kir7.1 sequence.

A

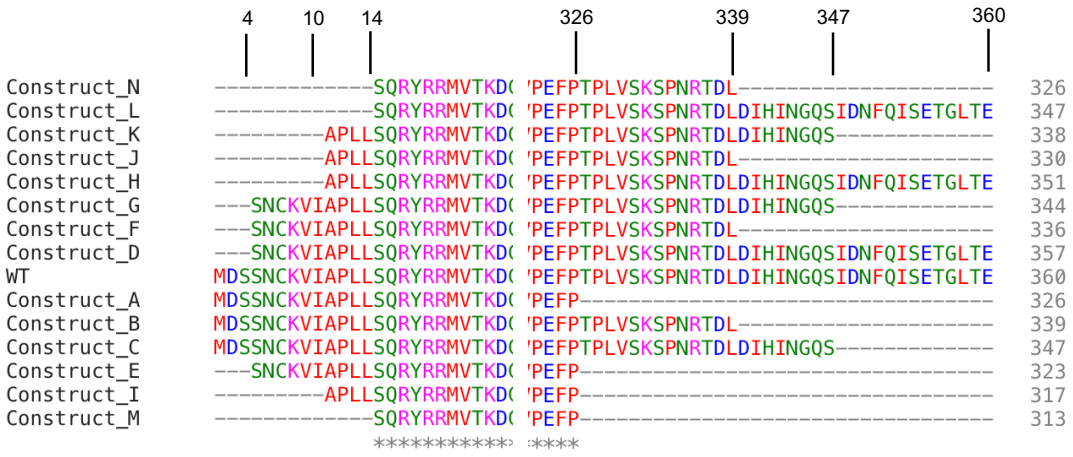

B

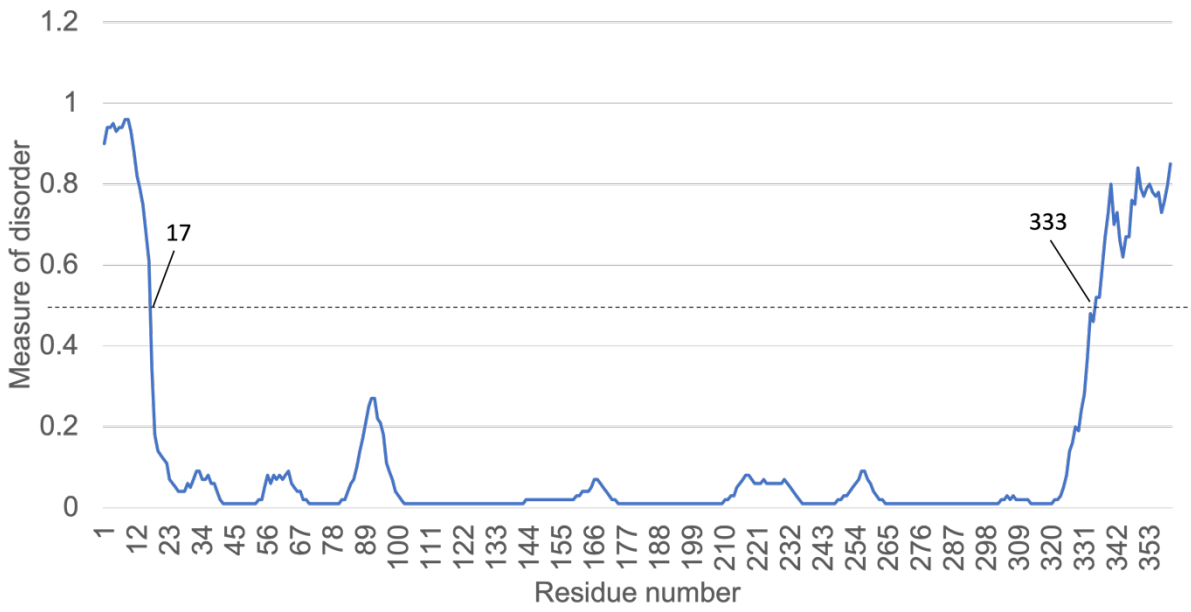

Figure 4.6. Prediction of disordered regions in Kir7.1 and construct design. **A.** Amino acid sequence alignment of constructs described in **Table 4.2**. The first 24 amino acids and the last 37 amino acids only are shown as all other amino acids are identical for all constructs. Residues 4, 10, 14, 326, 339, 347 and 360 are labelled. **B.** Plot showing predicted disorder of Kir7.1. Residue number is shown on the x-axis and the degree of disorder is measured on the y-axis. A threshold of 0.5 separates

ordered and disordered regions and this is represented by a dashed line. Residues before 17 and after 333 are above this threshold and classified as disordered.

4.3.3 Small-scale expression trials of WT construct library

All 14 constructs created were expressed in expi293F cells for 48 hours at 37 °C, as was determined to be the optimal conditions for WT expression (**Section 4.3.1**). Small-scale expression trials were conducted as outlined in **Section 3.5.4**. Protein expression levels were analysed by SDS-PAGE, WB and GFP fluorescence. The GFP fluorescence present in each construct, due to the GFP tag on the C-terminal, was detected in the SDS-PAGE (**Fig. 4.7**).

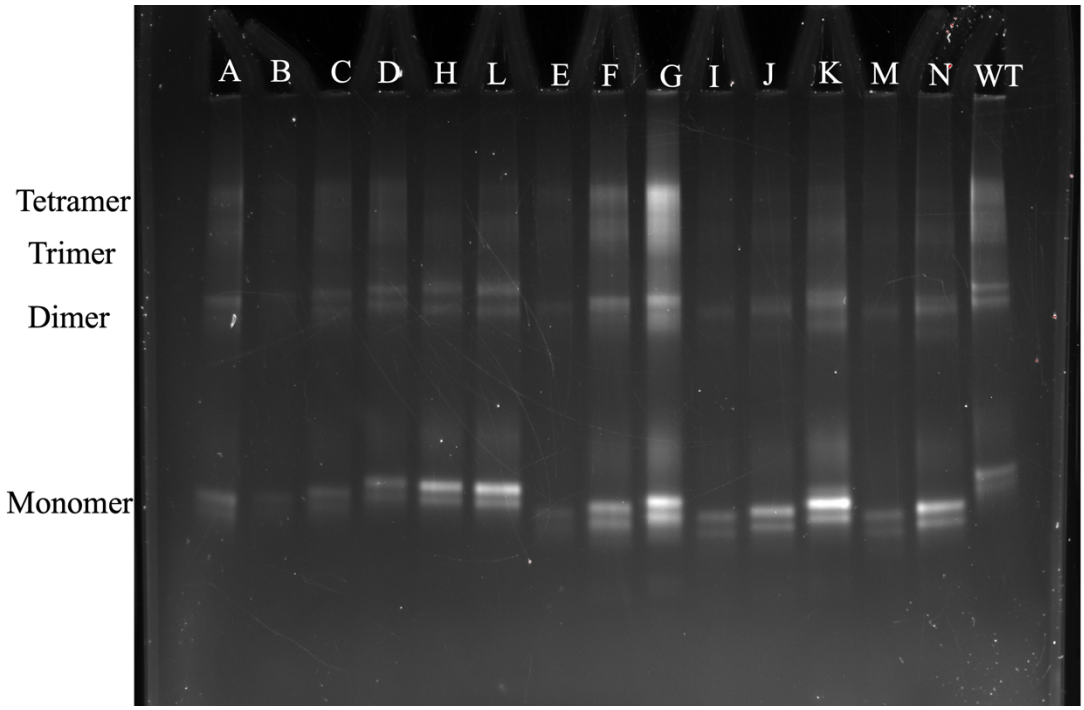

Figure 4.7. SDS-PAGE of truncated construct library expressed in HEK293 cells.

GFP fluorescence was measured and displayed by white bands. Kir7.1 monomer, dimer, trimer, and tetramer are labelled. The construct name is labelled above the corresponding lane.

Several truncated constructs were expressed in larger quantities compared to the full-length WT protein. In particular, construct L, construct G and construct K appear as a stronger band compared to WT (**Fig. 4.7**). Nevertheless, the WT protein was

generated in sufficient quantities, making it more preferable as a target for subsequent experiments compared to the truncated version. Truncated constructs were retained and prepared, but full-length WT protein was used for further experiments.

4.4 Purification of human Kir7.1

4.4.1 Detergent screening

4.4.1.1 Introduction

The first step in purifying a membrane protein is extraction from the phospholipid bilayer environment. The bilayer structure needs to be disrupted in order to extract the protein, but the protein structure itself needs to remain intact. One of the main approaches for this extraction is the use of amphiphilic molecules, such as detergents, that are capable of mimicking the stabilising properties of the native phospholipids. There is a wide variety of molecules with such detergent-like properties that are synthesised for this purpose and optimising the use of detergents for extraction and stabilisation of specific target proteins is vital (Churchward et al., 2005; Heinz and Niederweis, 2000; Lehner et al., 2003). There are currently no clear guidelines to suggest which detergent will be the most efficient for the extraction of a given protein. Therefore, studies of membrane proteins often begin with screening several different detergents.

4.4.1.2 Thermal unfolding of WT Kir7.1 extracted in different detergents

Thermal unfolding of Kir7.1, when solubilised in a range of different detergents, was analysed using a Prometheus Andromeda machine. The Andromeda machine measures changes in fluorescence while the protein unfolds during thermal treatment. A pico-RED dye interacts with the His-tag, allowing the protein to be detected without the need for purification.

Ten different detergents were tested, both with and without the addition of 100 mM of KCl. This work was completed by Dr. Belinda Faust at Vertex Pharmaceuticals.

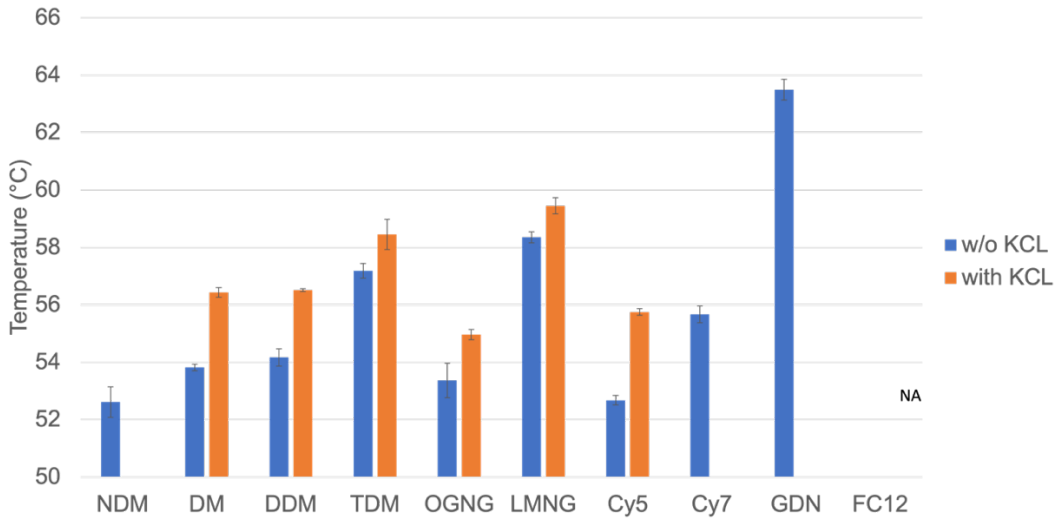

Figure 4.8. Thermal unfolding of wild type Kir7.1 extracted in different detergents.

Melting temperature is labelled on the y-axis and different detergents are labelled on the x-axis. Samples with KCl added are coloured orange and samples without the addition of KCl are coloured blue. It was not possible to test all samples in the presence of KCl due to limited access to the testing equipment. FC12 does not produce a Tm measurement due to its harsh nature, which causes protein denaturation upon solubilisation.

Thermal stability screening provided two main results. Firstly, all samples tested with KCl present showed increased stability compared to samples in the absence of KCl (**Fig. 4.8**). Since Kir7.1 is a potassium ion channel, it is anticipated that the presence of potassium would enhance its stability. Additionally, the presence of potassium ions can serve as an indicator that the channel is in a properly folded and functional state. Foscholine12 (FC12) is a harsh detergent that unfolds almost all proteins and serves as a negative control.

Secondly, the detergents to use for purification optimisation were identified. GDN appeared to stabilise the protein the most (**Fig. 4.8**), with LMNG and the maltoside detergents (DM, DDM, TDM) also appearing suitable.

4.4.1.3 Kir7.1 purified in different detergents

Based on the thermal stability screening, four detergents from four different classes were selected for purification trials. GDN, DDM, LMNG and cymal-5 were chosen

due to their differing chemical properties. An expression batch of 1.4 L of expi293F cells was split into four samples, each solubilised in a different detergent. The protein was solubilised in 1 % of each detergent, with 0.1 % CHS present in all except GDN. A FLAG pulldown purification was carried out for each sample followed by size exclusion chromatography using a superdex200 increase15/150 column.

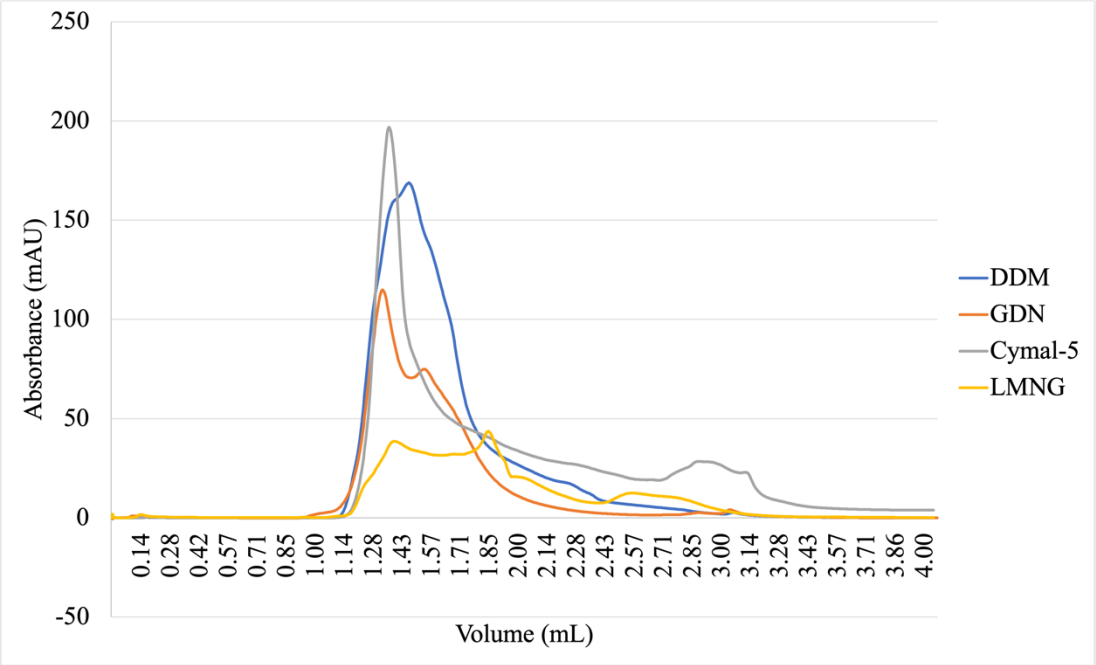

Figure 4.9. Size exclusion chromatography traces from detergent testing. Elution volume is displayed on the x-axis and UV absorbance is shown on the y-axis. The void volume was eluted at approximately 1.37 mL. Different coloured traces represent the different detergent-solubilised samples.

The importance of detergent selection is evident from this screening (**Fig. 4.9**). Purification using GDN (orange trace) produced a SEC profile with a distinct elution peak at the volume predicted for the tetrameric protein (1.5 mL). DDM (blue trace) showed increased protein extraction, however, the SEC profile showed a merged void peak and elution peak. Similarly, cymal-5 (grey trace) mainly demonstrated a void peak only, suggesting that the protein was unstable and aggregating. Finally, LMNG (yellow trace) exhibited a void peak and a second peak representing lower molecular weight proteins that may represent monomeric versions of Kir7.1.

In summary, the results of the detergent screening experiments indicated that GDN would be the most suitable detergent for effectively solubilising and purifying Kir7.1. When purified in GDN, Kir7.1 appeared the most stable (**Fig. 4.8**) and properly folded forming a tetramer (**Fig. 4.9**). Therefore, GDN was used as the purifying detergent for all future experiments.

4.4.2 Large-scale purification of Kir7.1 using GDN

When purifying Kir7.1 from large quantities of cells (>1 L) a FLAG pulldown step was conducted before concentrating the relevant fractions and loading onto a size exclusion column for a final purification step (outlined in **Section 3.5.4**). This final SEC analysis produced two elution peaks (**Fig. 4.10A**). The initial void peak was present at ~9 mL, followed by what was labelled 'peak 1' and 'peak 2' at ~11.9 mL and 14.2 mL, respectively (**Fig. 4.10A**). Peak 2 was positioned at the volume predicted for the tetrameric form of Kir7.1, whereas peak 1 represented a molecular weight of almost double the tetrameric molecular weight. Fractions from the void peak, peak 1 and peak 2 were analysed by SDS-PAGE and Kir7.1 was detected in all peaks (**Fig. 4.10B**).

Additionally, both peak 1 and peak 2 fractions were analysed by NS-EM. **Fig. 4.10** shows the NS-EM images, with particles in peak 1 appearing more heterogeneous compared to peak 2 and approximately double the length in diameter. Peak 2 particles exhibited a diameter similar to that predicted by Kir7.1 modelling. Taking the SEC and NS-EM analysis into consideration, it was concluded that peak 2 likely possessed the tetrameric form of Kir7.1 and was more appropriate to use for structural studies.

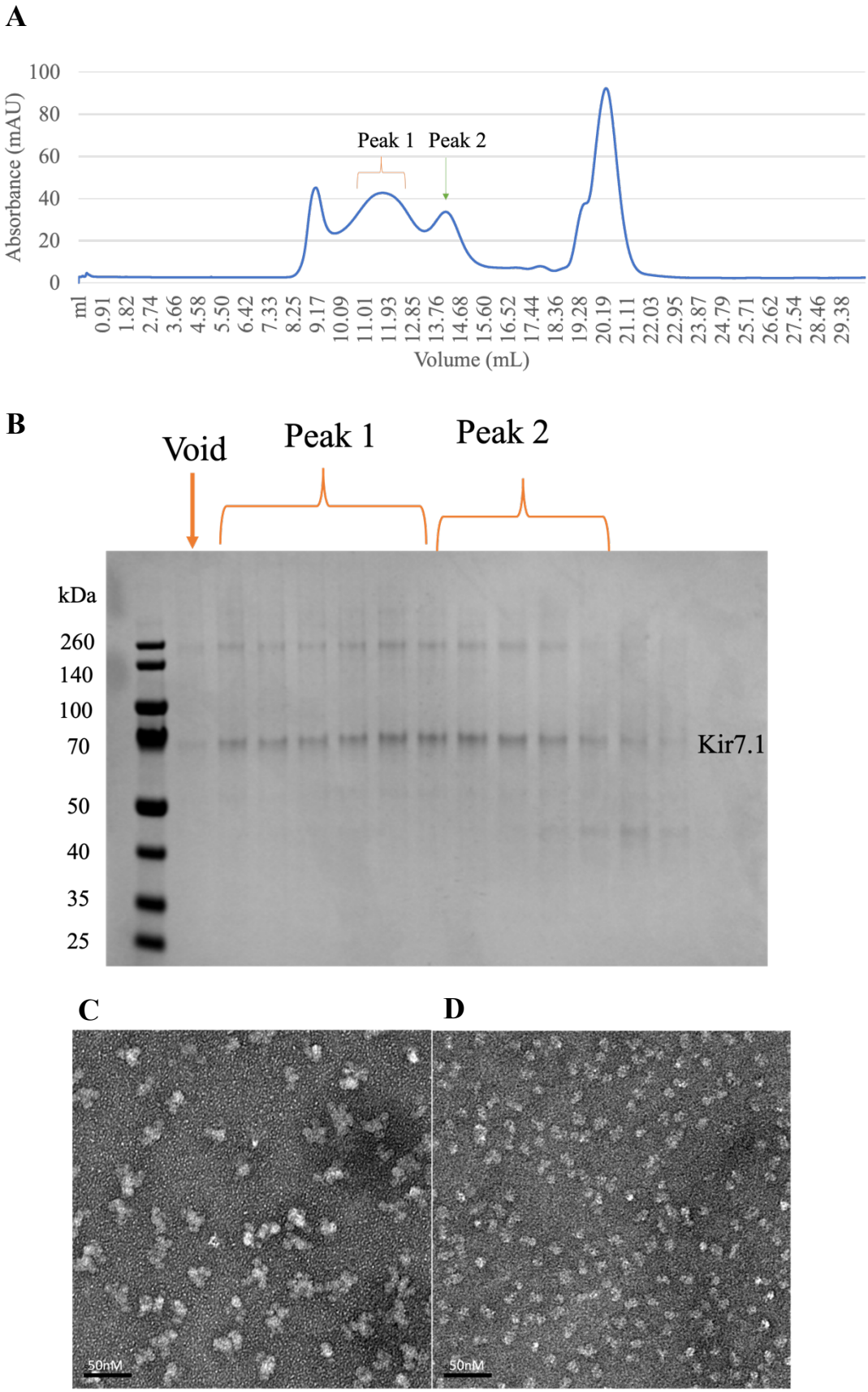

Figure 4.10. SEC, SDS-PAGE, and NS-EM analysis of Kir7.1 sample. A. Kir7.1 SEC profile exhibits two elution peaks of Kir7.1 protein. A void peak is present at ~9 mL with peak 1 and peak 2 labelled. **B.** Coomassie-stained SDS-PAGE analysis of

SEC peaks. Bands present at 70 kDa represent Kir7.1 in all peaks. **C.** NS-EM image of particles from peak 1. **D.** NS-EM image of particles from peak 2. Scale bar is 50 nM.

4.4.3 Confirmation of Kir7.1 identity by mass spectrometry

Peak 1 and peak 2 samples were sent to the BSRC Mass Spectrometry Facility (University of St. Andrews) for protein identification. Proteins present in the sample were digested and the peptides were analysed by mass spectrometry (MS). The MS spectra were searched against the Swiss-Prot protein database for identification. The top hit in both peaks was Kir7.1. **Fig. 4.11** exhibits the peptide hits from the MS analysis mapped onto Alphafold models of Kir7.1. Peptide hits were predominantly found in the N- and C-terminal portions of the protein. The transmembrane domains of membrane proteins are very hydrophobic and can be challenging for proteomic workflows (Min et al., 2015). Transmembrane domains tend to have fewer trypsin cleavage sites and trypsin digestion of membrane proteins can lead to low protein sequence coverage (Macher and Yen, 2007). Therefore, obtaining peptide hits from the cytoplasmic domain and the N-terminal region of Kir7.1 was a positive result. Along with Kir7.1 peptide hits, peptides from heat shock protein 70 (Hsp70) were detected. Heat shock proteins are stress-induced proteins that assist in the folding of non-native proteins and quality control of misfolded proteins (Mayer and Bukau, 2005). The presence of heat shock proteins is frequently observed when human proteins are overexpressed, and cells undergo stress. Nevertheless, in order to attain the utmost purity in the final sample, measures were implemented to minimise the presence of these chaperones.

A

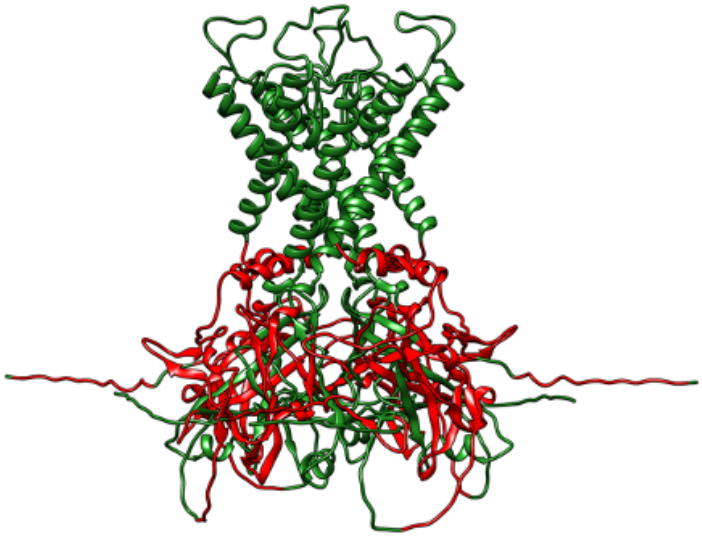

```
  1 MDSSNCKVIA PLLSQRYRRM VTKDGHSTLQ MDGAQRGLAY LRDAWGILMD
 51 MRWRWMMLVF SASFVVHWLV FAVLWYVLAE MNGDLELDHD APPENHTICV
101 KYITSFTAAF SFSLETQLTI GYGTMFPSGD CPSAIALLAI QMLLGLMLEA
151 FITGAFVAKI ARPKNRAFSI RFTDTAVVAH MDGKPNLIFQ VANTRPSPLT
201 SVRVSAVLYQ ERENGKLYQT SVDFHLDGIS SDECPFFIFP LTYYHSITPS
251 SPLATLLQHE NPSHFELVVF LSAMQEGTGE ICQRRTSYLP SEIMLHHCFA
301 SLLTRGSKGE YQIKMENFDK TVPEFPTPLV SKSPNRTDLD IHINGQSIDN
351 FQISETGLTE
```

B

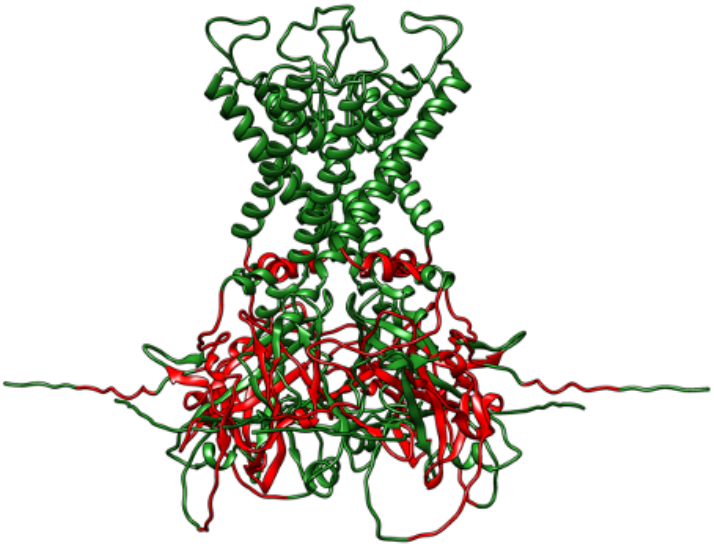

```
  1 MDSSNCKVIA PLLSQRYRRM VTKDGHSTLQ MDGAQRGLAY LRDAWGILMD
 51 MRWRWMMLVF SASFVVHWLV FAVLWYVLAE MNGDLELDHD APPENHTICV
101 KYITSFTAAF SFSLETQLTI GYGTMFPSGD CPSAIALLAI QMLLGLMLEA
151 FITGAFVAKI ARPKNRAFSI RFTDTAVVAH MDGKPNLIFQ VANTRPSPLT
201 SVRVSAVLYQ ERENGKLYQT SVDFHLDGIS SDECPFFIFP LTYYHSITPS
251 SPLATLLQHE NPSHFELVVF LSAMQEGTGE ICQRRTSYLP SEIMLHHCFA
301 SLLTRGSKGE YQIKMENFDK TVPEFPTPLV SKSPNRTDLD IHINGQSIDN
351 FQISETGLTE
```

Figure 4.11. Mass spectrometry peptide hits shown on Kir7.1 predicted structure.

A. Peak 1 peptide hits mapped onto the predicted model of Kir7.1 and coloured red. The amino acids identified in the peptide hits are coloured red in the sequence below. **B.** Peak 2 MS peptide hits are coloured red on the Kir7.1 predicted model and on the related amino acid sequence.

4.4.4 Removal of the Hsp70 contamination

An ATP wash step was introduced into the purification in an attempt to remove the Hsp70 chaperone. ATP directly interacts with Hsp70, and this could reverse any current interaction of Hsp70 with Kir7.1 and eliminate the chaperone from the sample. The addition of an unfolded protein can aid this process as it has the ability to further attract chaperone binding (Morales et al., 2019).
Therefore, the addition of ATP-Mg and an unfolded protein was tested to investigate if the presence of Hsp70 in the purified protein sample could be reduced.

An ATP wash step with 2 mM, 5 mM, and 5 mM ATP with α-synuclein was evaluated. **Fig. 4.12** shows the SDS-PAGE result representing the ATP wash step and the final FLAG elution step. The wash steps for all three conditions displayed a strong protein band at the 70 kDa molecular weight representing Hsp70. Additionally, in the elution fractions for all three samples, there is a protein band at a position slightly below 70 kDa that represents the Kir7.1 monomer. There was still a faint band for Hsp70 in the elution fraction, but a large portion was removed in the wash step. It was concluded that all ATP conditions achieved the same level of contaminant removal and therefore, the lowest amount, 2 mM, was used for subsequent experiments.

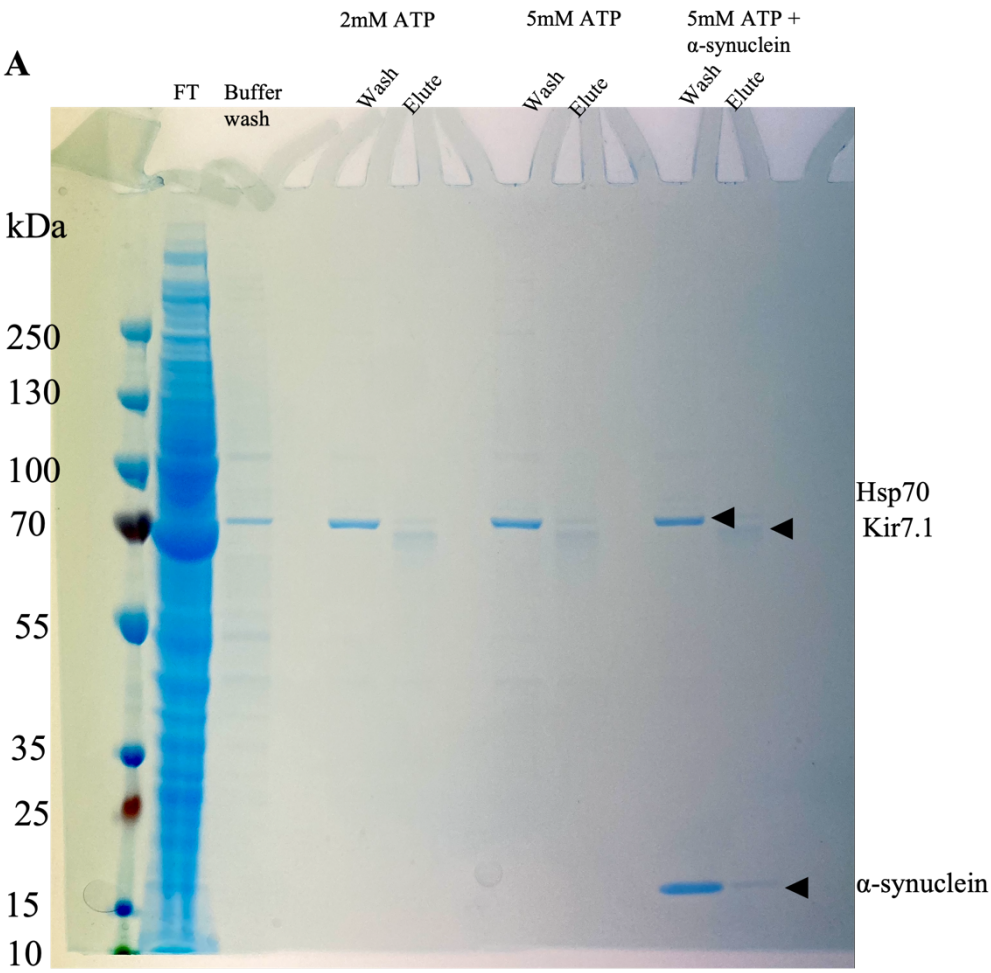
A
2mM ATP
5mM ATP
5mM ATP +
α-synuclein
FT
Buffer
wash
Wash
Elute
Wash
Elute
Wash
Elute
kDa
250
130
100
70
55
35
25
15
10
Hsp70
Kir7.1
α-synuclein

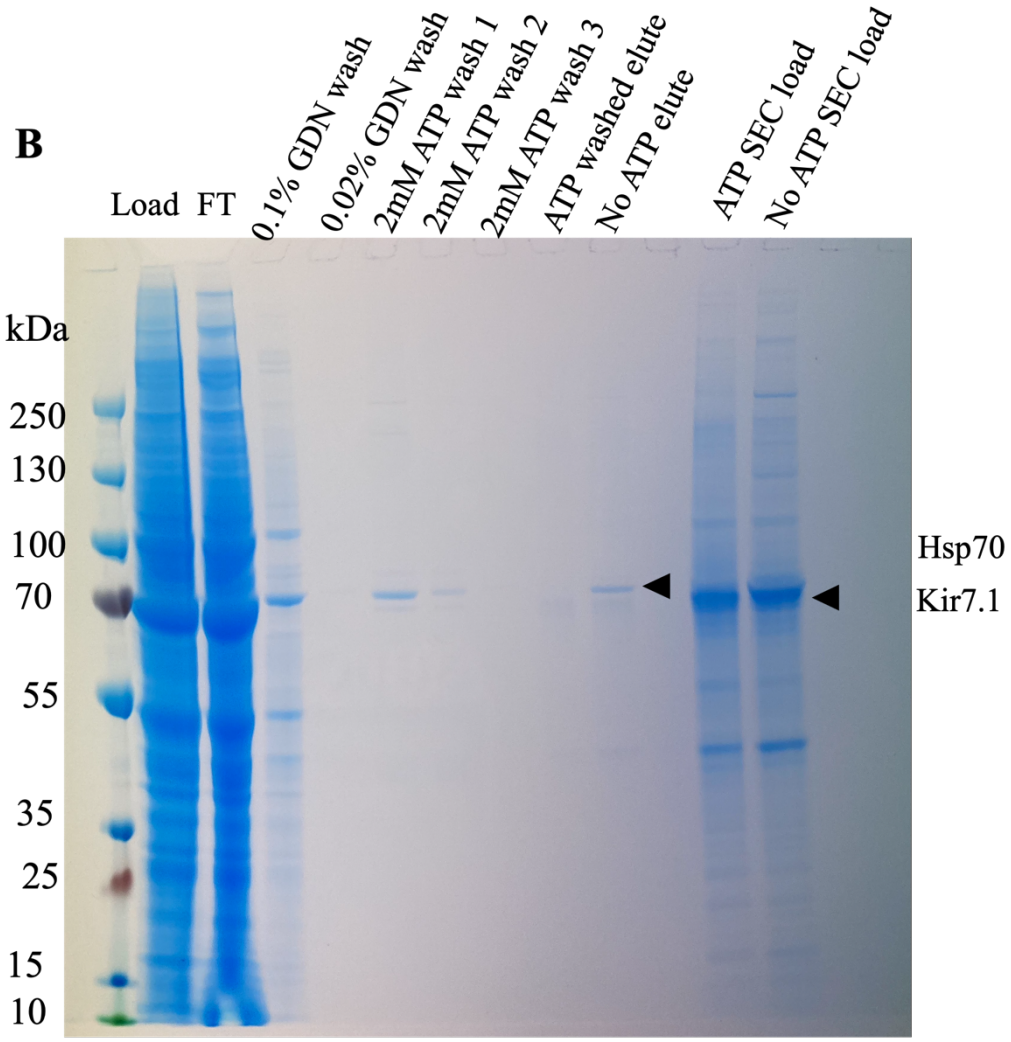

Figure 4.12. SDS-PAGE analysis of ATP washes used for Hsp70 removal.
A. Initial ATP wash evaluation for Hsp70 removal. Three conditions were tested: 2 mM ATP, 5 mM ATP, and 5 mM ATP in the presence of α-synuclein. The lanes labelled wash represent the ATP wash step and the lanes labelled elute represent the FLAG elution. FT is the flow-through and buffer wash is the initial wash in the FLAG purification protocol. **B.** Coomassie-stained SDS-PAGE showing purification with an ATP wash step compared to purification without an ATP wash step. 2 mM ATP wash was conducted three separate times and labelled wash 1, 2 and 3. 'ATP washed elute' and 'No ATP wash elute' show the protein eluted in the final step of the FLAG purification. SEC load samples are the concentrated elute fractions prepared for loading onto the size exclusion chromatography column.

The implementation of the 2 mM ATP wash step into the overall purification protocol was tested. It was necessary to investigate if the removal of Hsp70 affected the stability of Kir7.1.

Three ATP wash steps were carried out to ensure sufficient washes were being conducted **(Fig. 4.12)**. By the third wash, there was no longer a protein band observed at 70 kDa suggesting that all contamination that can be removed by the ATP wash had been removed. The elution fractions from purified samples with and without the ATP wash showed a clear distinction at this 70 kDa mark. Both samples, when concentrated for SEC, displayed similar amounts of Kir7.1 protein suggesting that ATP washing did not hamper Kir7.1 purification. Analysis by SEC showed comparable profiles for both samples (**Fig. 4.13**). Overall, the addition of an ATP wash step appeared to reduce the presence of the Hsp70 contamination whilst retaining protein stability. Therefore, this step was fully implemented into the FLAG purification workflow and was used for all future experiments.

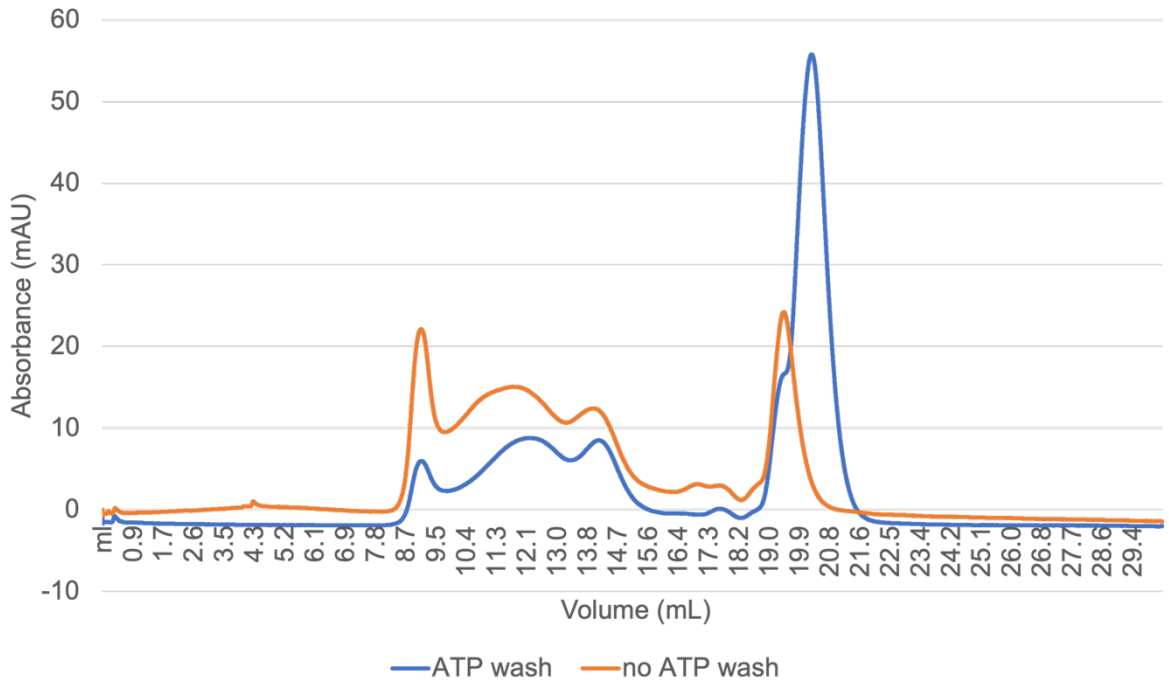

Figure 4.13. Size exclusion chromatography from protein purifications with and without ATP washes.

Protein purified without an ATP wash step is represented by an orange UV trace and protein purified with the implementation of an ATP wash step is shown in blue.

4.4.5 Reducing size exclusion chromatography peak 1

Following preliminary structural studies, it was decided to attempt further optimisation of the purification workflow to improve sample quality. This involved an investigation into reducing the presence of peak 1 in the SEC profile (**Fig. 4.14**) by cleaving the GFP fusion tag on the C-terminus of the protein. A TEV cleavage enzyme was incubated with the protein post FLAG pulldown to cleave the GFP overnight. As the 10x-His tag was positioned on the C-terminus of the GFP, it was then possible to conduct a reverse Ni-NTA purification where the cleaved protein was collected in the flow-through sample. This experiment displayed a shift of peak 1 towards peak 2 suggesting that cleaving the GFP tag helped recover tetrameric Kir7.1. GFP cleavage was fully implemented into the purification workflow and used for all further experiments.

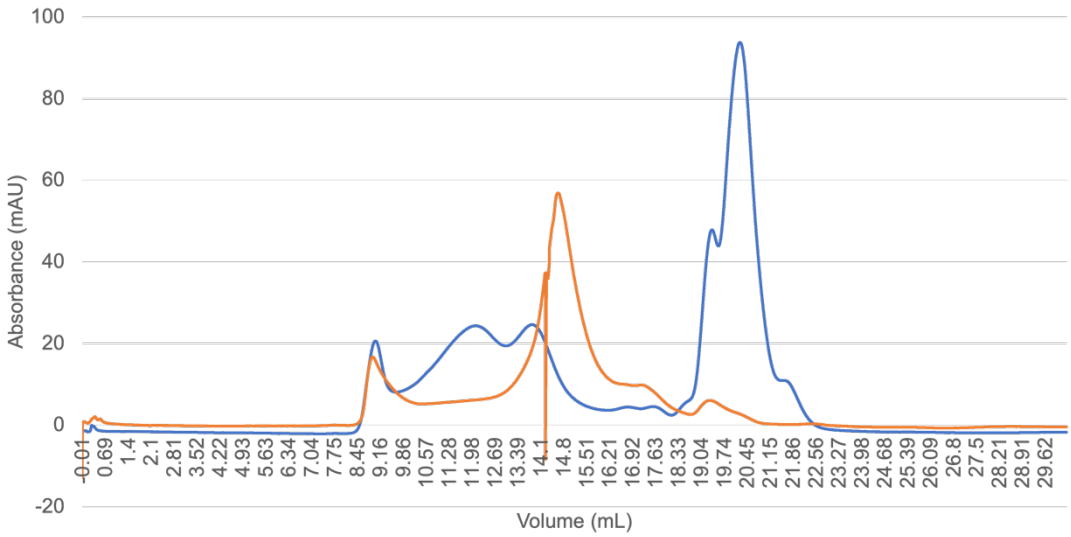

Figure 4.14. SEC analysis of GFP cleaved sample compared to sample without GFP cleavage.

UV trace of protein purified without a GFP step is shown in blue. Peak 1 and peak 2 can be observed at ~12 mL and ~14 mL. The UV trace of protein purified with GFP cleaved is shown in orange. Peak 2 is now detected at ~15 mL. An AKTA error caused an artefact observed in the orange trace at ~14.3 mL.

4.4.6 Summary

A comprehensive evaluation was conducted to assess various approaches and techniques for the expression and purification of Kir7.1. After conducting tests on both bacterial and mammalian expression systems, HEK293 cells were determined to be the optimal choice. Furthermore, a bacterial-human chimera construct was generated and expressed in both systems, providing an alternative avenue for studying Kir7.1. It was observed that the wild type protein and the chimeric protein exhibited comparable expression levels. Consequently, the wild type construct was deemed optimal for subsequent structural analysis.

A construct library of truncated Kir7.1 was created and expressed to investigate the effect of removing regions of disorder. Several constructs showed increased expression levels compared to the WT protein, but the full-length protein was expressed in sufficient quantities for further studies. In conclusion, an expression and purification protocol was developed, optimised, and proven effective in generating sufficient quantities of full-length human Kir7.1 protein.

Chapter 5

5. Structural insights into Kir7.1 using cryo-electron microscopy

This chapter focuses on the structural studies carried out on Kir7.1. Optimisation of expression and purification outlined in section four produced a stable tetrameric version of Kir7.1. The aim was to use electron microscopy and single-particle analysis to study the protein. Kir7.1 samples were prepared in both an apo form and in the presence of PIP_2. As outlined in Chapter One, PIP_2 is a membrane-bound phospholipid that activates all human Kir channels. Given the lack of prior structural information regarding Kir7.1 and its activation, both structures were of significant interest. This research aimed to determine two structures that could elucidate the effect of PIP_2 binding.

5.1 Preliminary cryo-EM experiments of Kir7.1

Three initial cryo-EM data sets were collected using the conditions outlined in **Sections 3.7.2.1 and 3.7.3**. Two preliminary data sets, initial-apo-Kir7.1 and initial-apo-Kir7.1-GO, were collected based on a preliminary grid screening. Initial-apo-Kir7.1 grids were prepared using unsupported ice, while initial-apo-Kir7.1-GO grids employed a graphene oxide support. **Fig. 5.1A and 5.2A** display representative micrographs from these data collections, showing the increased particle density when using the graphene oxide support compared to unsupported ice. The micrograph with unsupported ice also shows particles close together and possibly overlapping (**Fig. 5.1A**).

Both data sets were processed using cryoSPARC Live and cryoSPARC. Firstly, the unsupported data set was evaluated. Blob picker selected ~600 k particles and 2D classification removed any 'junk' particles. Final 2D classes are shown in **Fig. 5.1A** and this represented a final 34,000 particles. Heterogeneous refinement and non-uniform refinement resulted in a final low-resolution reconstruction (**Fig. 5.1B**). Several other attempts were made to improve map refinement but there was no success.

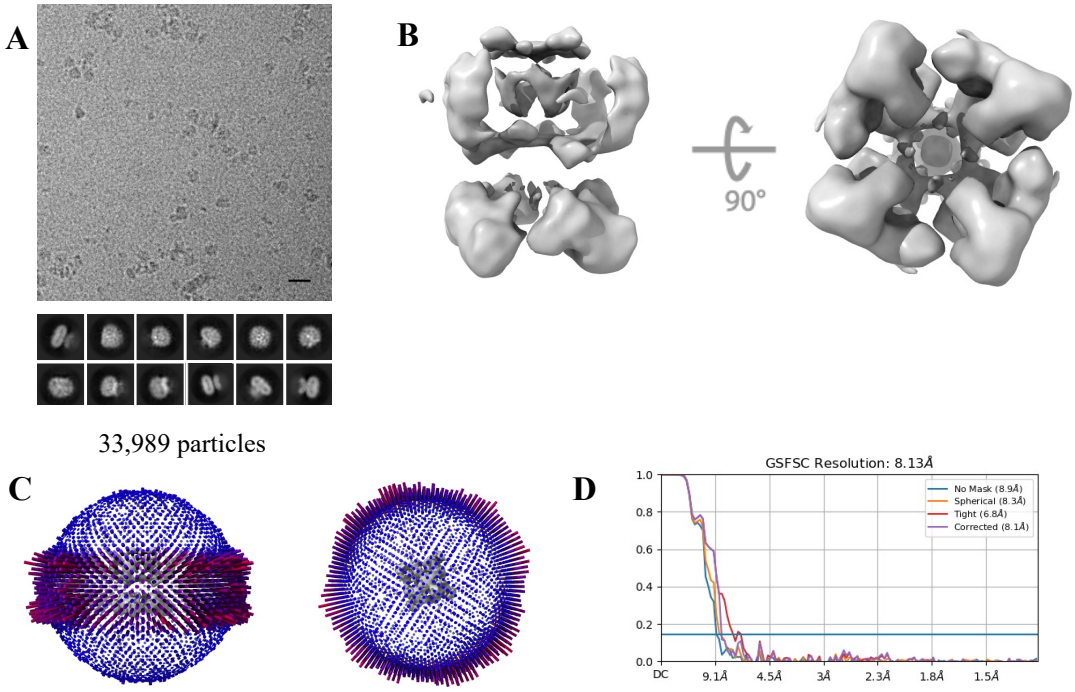

Figure 5.1. Image processing and 3D reconstruction of initial-apo-Kir7.1. A. Representative micrograph and 2D classes. **B.** Non-uniform refinement using ~30 k particles. **C.** 3D histogram showing the orientation distribution of final selected particles. **D.** Fourier shell correlation (FSC) plot for the calculated half-maps; overall resolution determined by the 0.143 criterion (blue line) was 8.13 Å.

Due to the limited resolution of the unsupported data set, the focus was put on the graphene oxide-supported data. Initially, blob picker was used to select particles and generate 2D classes, which were subsequently utilised for template picking. Particles were extracted in a box size of 360 pixels and generated 2D classes (**Fig. 5.2A**). *Ab initio* reconstruction produced an initial map and after several rounds of heterogeneous refinement, non-uniform refinement produced a low-resolution map using ~50 k particles (**Fig. 5.2B**). Gold-standard Fourier shell correlation (GSFSC) curves determined a resolution of 6.32 Å, however, the map did not show any clear features that would be evident in a map of that resolution. The map gave an overall shape comparable to a Kir channel, however, there were not any distinct features in the map corresponding to secondary structural elements in the protein. A second data set was collected from the same grid preparation and was processed independently

and merged with this data set. Extensive data processing was conducted but unfortunately, no improvement to the consensus refinement was achieved.

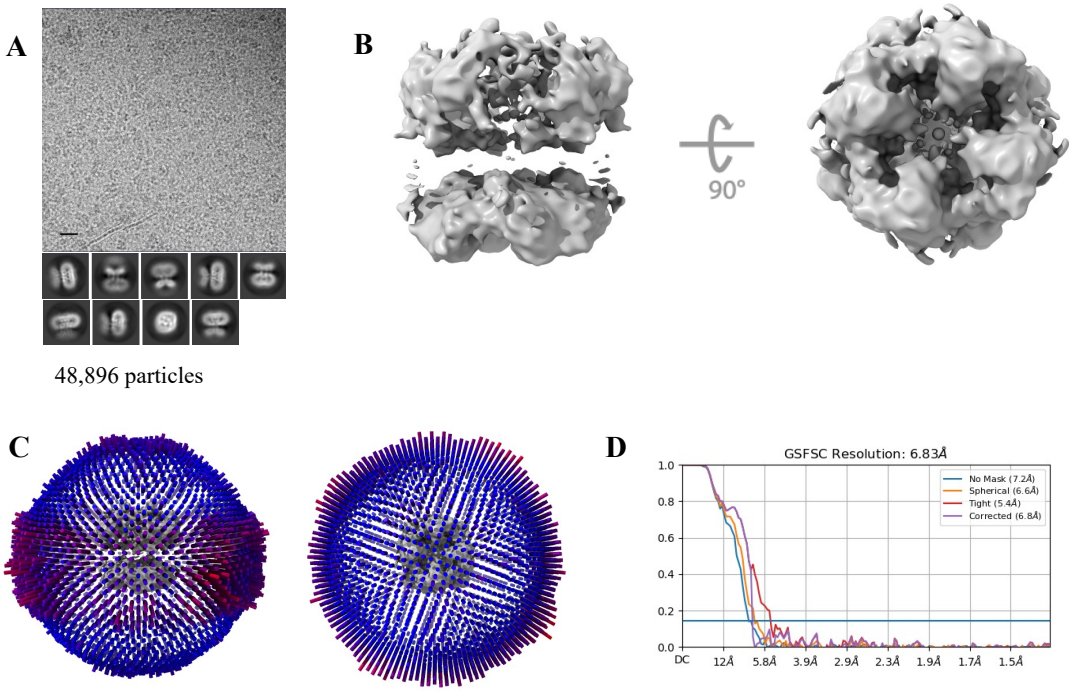

Figure 5.2. Image processing and 3D reconstruction of initial-apo-Kir7.1-GO. A. Representative micrograph and 2D classes. **B.** Non-uniform refinement using ~50 k particles. **C.** 3D histogram showing the orientation distribution of final selected particles. **D.** Fourier shell correlation (FSC) plot for the calculated half-maps; overall resolution determined by the 0.143 criterion (blue line) was 6.83 Å.

5.2 Optimisation of Kir7.1 protein sample

Due to the limitations of the initial cryo-EM data sets, the biochemistry was revisited, and the purification protocol was further optimised (**Section 4.4.5**). Size exclusion chromatography fractions from the optimised samples were first analysed by NS-EM (**Fig. 5.3**). All four fractions analysed appeared homogeneous with particles evenly distributed across the grid. To maintain the highest possible sample homogeneity, only the two central fractions were selected for future structural analysis.

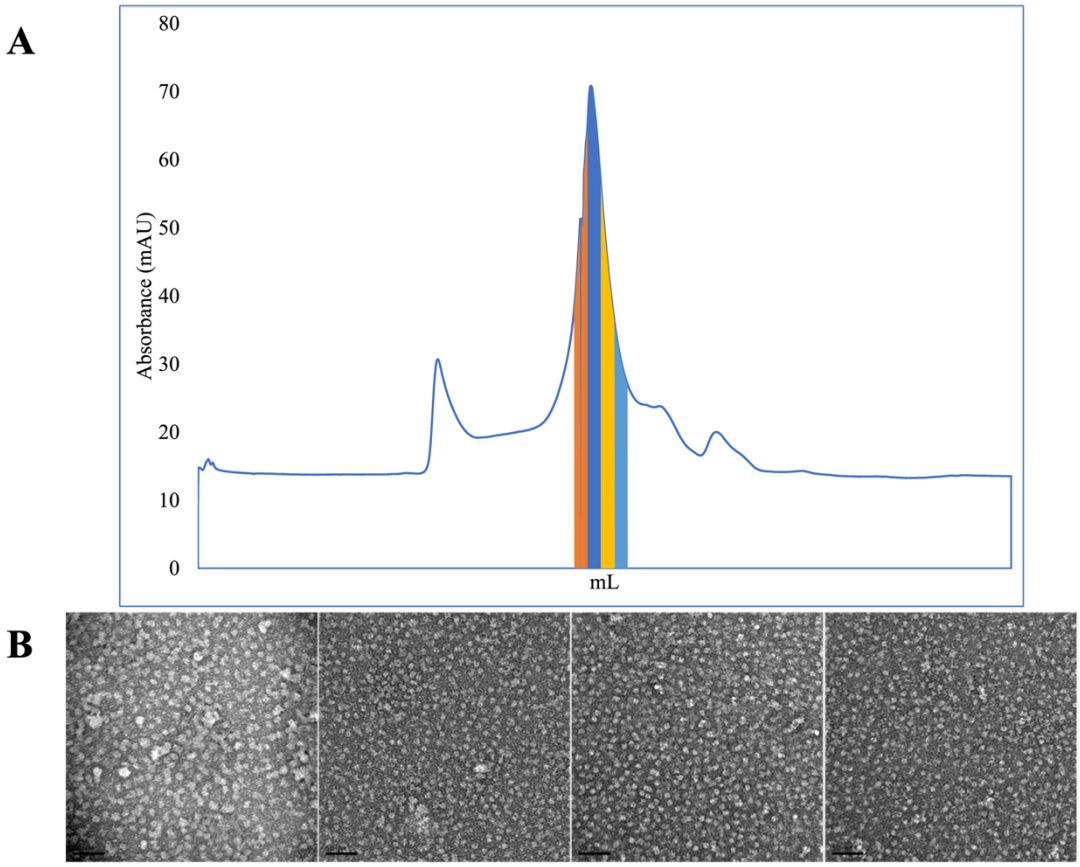

Figure 5.3. Characterisation of optimised purification fractions by NS-EM. A. SEC profile from protein purification with four main fractions from the elution peak coloured differently. **B.** NS-EM images of a sample from each fraction of the elution peak. NS-EM images are in the order they appear in the peak, from orange to blue going left to right. The scale bar is 50 nm for all images.

5.3 Cryo-EM analysis of apo Kir7.1

5.3.1 Sample preparation

Subsequently, different grid types and vitrification parameters were evaluated. Quantifoil R1.2/1.3 on 300 gold mesh and UltrAuFoil holey gold grids were used. Compared to the initial cryo-EM attempts, higher protein concentrations were used in the range of 4-8 mg/mL. Samples were centrifuged at 100, 000 x *g* before blotting to remove any aggregates. Each grid support demonstrated successful protein vitrification and particle distribution. If the ice in the centre of the holes became too thin due to longer blotting times, particles were sequestered to the edges of the holes. 6 mg/mL protein concentration was applied to Quantifoil grids and blotted for four

seconds before vitrification. For further grid preparations, Quantifoil supports were used with ~6/7 mg/mL protein applied.

5.3.2 Grid screening and data collection

Two samples were prepared for data collection: Kir7.1 only and Kir7.1 with 1mM C8-PIP_2 added. Both samples were vitrified on Quantifoil grids with gold mesh and screened on a Titan Krios TEM with 300 kV accelerating voltage and K3 detector. EPU software was used to screen grid squares and evaluate ice thickness and particle distribution. Grid squares with thinner ice demonstrated a sequestering of particles to the edges of the holes and therefore squares with thicker ice were selected for data collection.

Two data sets were collected for apo Kir7.1, 12,558 micrographs initially and a subsequent 23,114 micrographs. Both data sets were processed independently and produced similar EM density maps, with the first data set map being of lower quality. Despite merging both data sets in an effort to enhance map resolution, no improvements were observed in either resolution or map quality. As a result, the second data set, which generated the highest resolution map, was selected for the final reconstructions and model building.

5.3.3 Data processing

23,114 micrographs were imported into cryoSPARC and after motion correction, CTF estimation and manual exposure curation, particles were selected using blob picker. Particles were extracted in a 440-pixel box and binned by a factor of 2 resulting in a box size of 200 pixels. The extracted particles were subjected to 2D classification to generate templates, which were subsequently employed in the template picker process. This led to the selection of nearly 6 million initial particles. 2D classification was implemented for several rounds of ‘cleaning’ these particles and ‘good’ classes were used for *ab initio* reconstruction with three classes. The best and worst classes obtained from the *ab initio* reconstruction were employed in several rounds of heterogeneous refinement. This process aimed to further segregate poor-quality particles into the 'poor 3D class,' thereby enhancing the quality of the final refinement. The best class was subjected to non-uniform refinement to further

enhance the consensus refinement. This iterative process was repeated until no further improvement in the consensus refinement was observed, as depicted in **Fig. 5.4**. Three masks were generated to encompass either the transmembrane domain, the cytoplasmic domain, or the whole protein excluding the micelle. Local refinement with C4 symmetry was used with each of these masks but no significant improvement was observed in any case. The final 3D refinement produced a map with a global resolution of 3.54 Å.

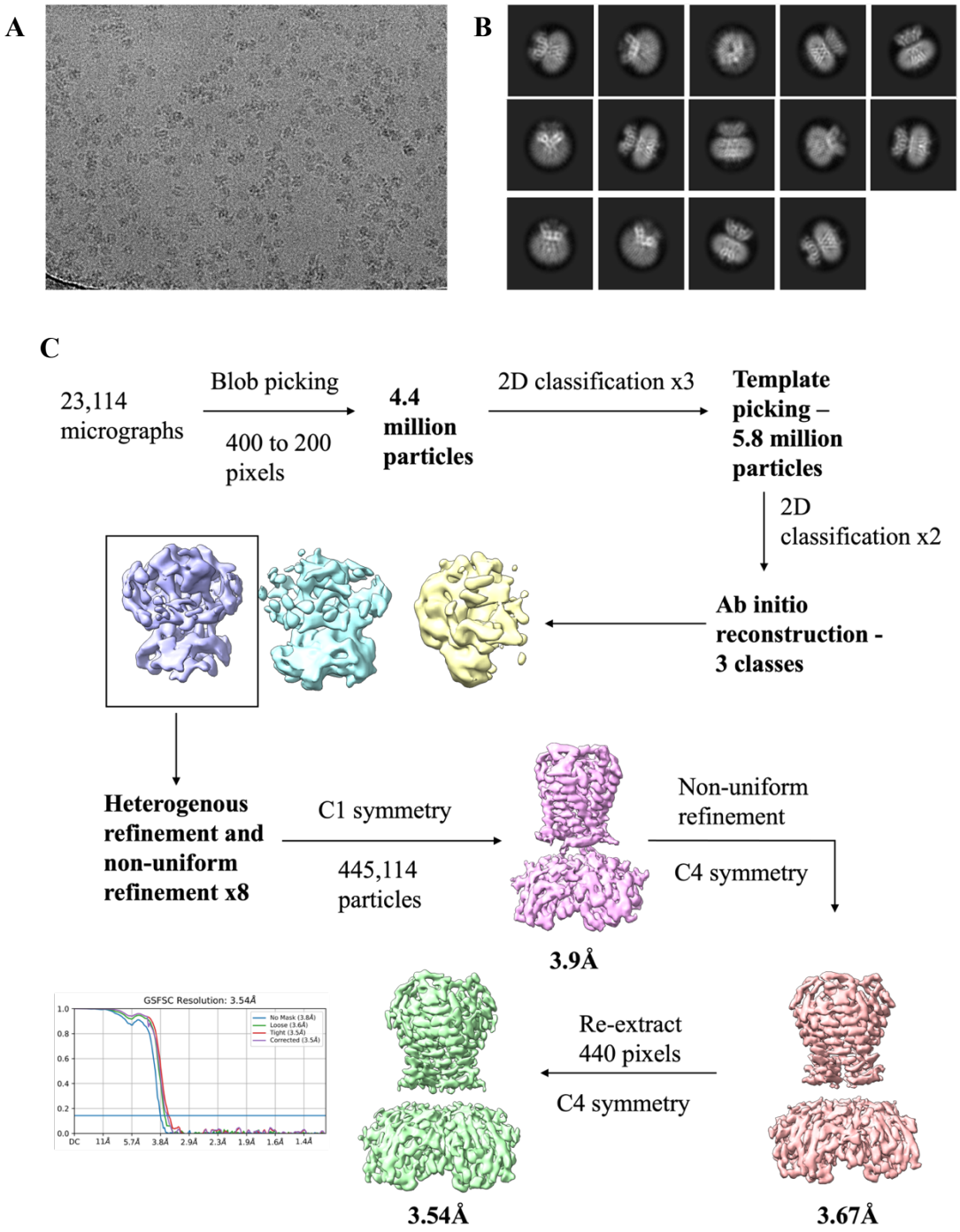

Figure 5.4. Image processing overview of the apo Kir7.1 data set. A. Representative micrograph from the data set. **B.** 2D class averages showcasing a range of views of Kir7.1 within the detergent micelle. **C.** Image processing workflow producing a final refinement of 3.54 Å with C4 symmetry.

Image processing yielded a 3D reconstruction of Kir7.1 at a resolution of 3.54 Å. DeepEMhancer was used to sharpen the map (**Fig. 5.5**). Local resolution estimation was coloured onto the sharpened map highlighting the difference in resolution throughout the channel (**Fig. 5.5B**). Regions of lower resolution are observed in the extremities of the channel and the N and C termini where the protein enters regions of disorder (coloured blue in **Fig. 5.5B**). The flexible linker region between the TMD and the CTD also demonstrates lower resolution, attributed to its inherent flexibility. 3D variability analysis in cryoSPARC was conducted to investigate discrete and continuous heterogeneity in the data set. These results displayed continuous movement of the CTD in relation to the TMD. A swinging and twisting motion could be observed but distinct conformations could not be isolated within the dataset. The observed intrinsic flexibility and movement within the dataset and the protein suggest that these dynamic factors may contribute to the limited overall resolution of the EM map.

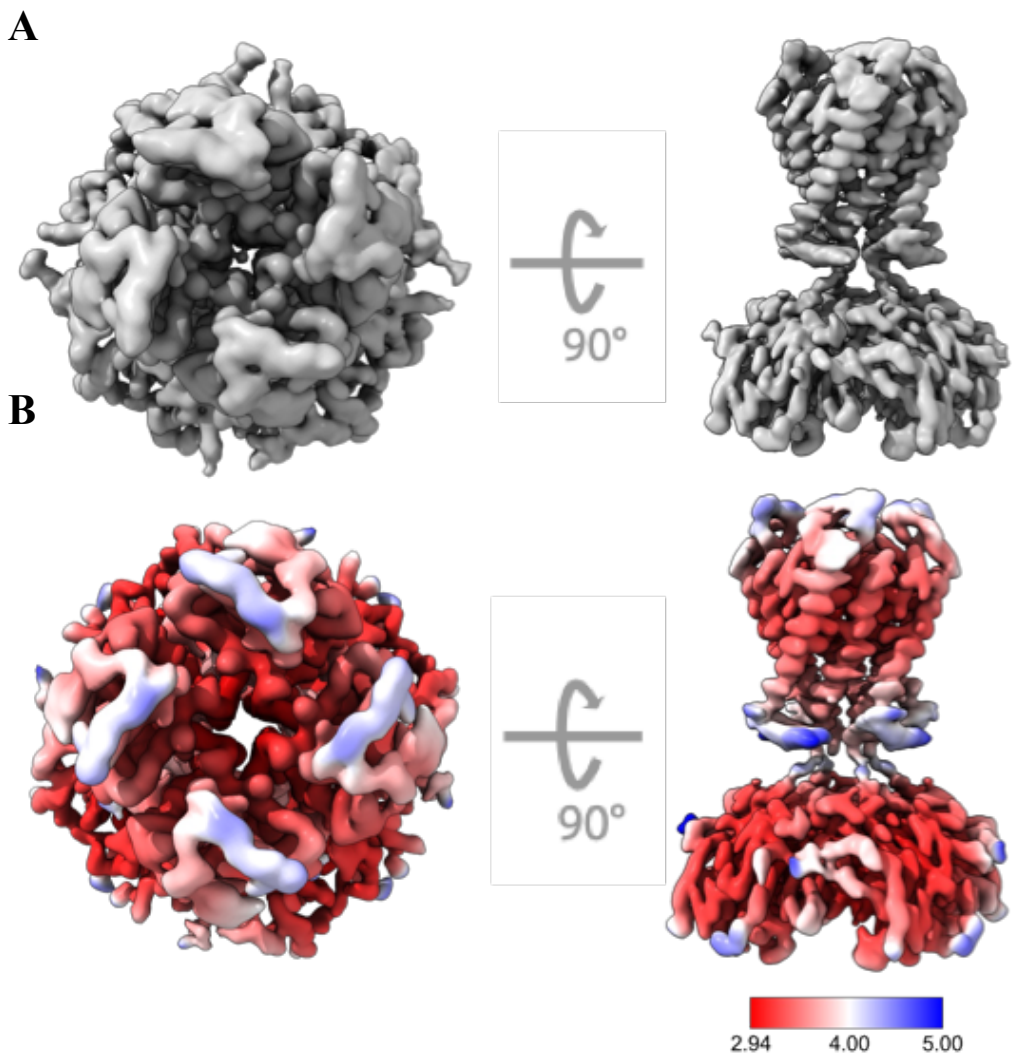

Figure 5.5. EM density map of Kir7.1. A. EM map sharpened using DeepEMhancer showing a top-down and side-on view of the channel. **B.** Sharpened map coloured by local resolution. The colour scale is shown by the bar underneath, with units in Å.

5.3.4 Model building, refinement, and validation

The quality of the EM density map enabled successful model building. Initial attempts involved using SWISS-MODEL to generate homology models (Waterhouse et al., 2018). When these models were docked into the EM map, they provided a poor fit. Subsequently, Alphafold multimer was used to generate a predicted model of the tetrameric protein (Evans et al., 2021). The Alphafold-predicted model was divided into two sub-models: one for the transmembrane domain and another for the cytoplasmic domain. Docking these domains independently resulted in a better fit.

However, certain regions still exhibited a poor fit to the density map. Finally, ModelAngelo was used to automatically build the protein into the density map. The resulting model displayed accurate building in most regions, but some loops and flexible regions were still missing. The map was blurred in Coot and regions of lower resolution were manually built into the density and refined using Phenix real-space refine. The final apo Kir7.1 model had residues 17-28, 45-305 and 310-324 built.

The final model was validated using both Phenix and Isolde and the model quality and fit to the data were validated by Ramachandran plot, rotamer outliers, clash score and using validation tools such as Molprobity, Caßlam and map-to-model (**appendix 1**) (Prisant et al., 2020; Williams et al., 2018). The core portion of the protein, comprising the transmembrane alpha helices and the beta strands in the CTD have the highest map-to-model correlation coefficients. The TMD-CTD flexible linker demonstrates the poorest fit due to the lower resolution and flexibility in the region. The final, validated model revealed general structural elements that are typical of Kir channels, coloured accordingly in **Fig. 5.6**. In each subunit, two alpha helices span the membrane, while a third, smaller helix known as the pore helix points inwards, forming the selectivity filter. The helix bundle crossing and the G-loop, two previously studied gating points within Kir channels are also observed (**Fig. 5.6B**). The Kir7.1 model in **Fig. 5.6A** highlights the arginine at position 162 within the flexible linker region. This residue is known to be involved in the binding of PIP_2, and in patients suffering from snowflake vitreoretinal degeneration, the native arginine is mutated to a tryptophan residue.

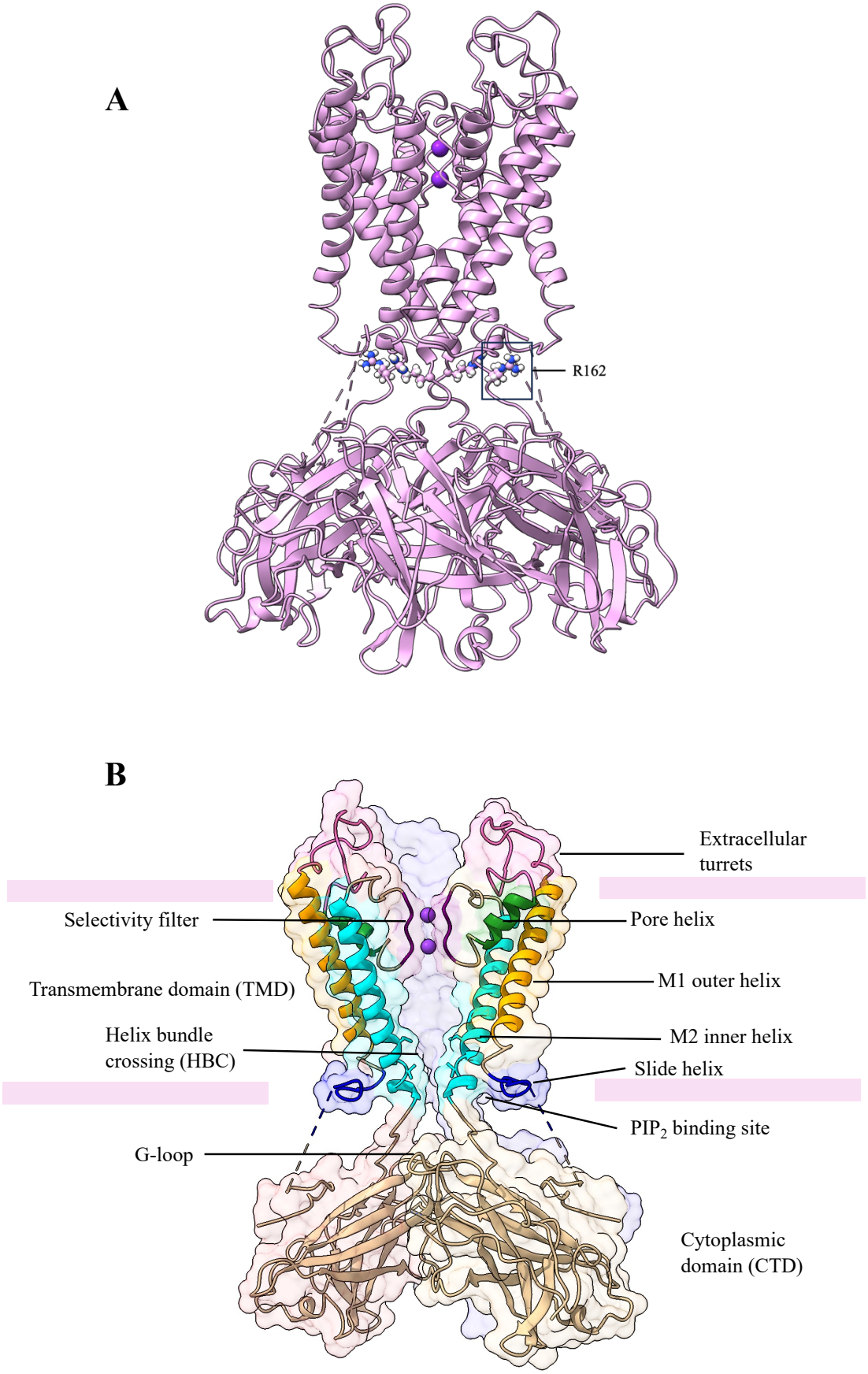
A
R162
B
Extracellular turrets
Selectivity filter
Pore helix
Transmembrane domain (TMD)
M1 outer helix
Helix bundle crossing (HBC)
M2 inner helix
Slide helix
PIP2 binding site
G-loop
Cytoplasmic domain (CTD)

Figure 5.6. Kir7.1 model showcasing typical Kir channel features. A. The complete apo model with all four subunits shown. Two potassium ions in the selectivity filtered are coloured purple. Arginine at residue position 162 is displayed with the side chain shown as ball and stick. **B.** Key Kir channel features displayed on the apo Kir7.1 model. Side view of Kir7.1 atomic model fitted into cryo-EM map (transparent coloured surface). Two subunits are shown with typical structural features of Kir channels coloured and labelled: outer helix (M1, yellow), inner helix (M2, cyan), pore helix (green), slide helix (blue), selectivity filter (purple), extracellular region (pink), G-loop, helix bundle crossing (HBC) and PIP_2 binding site. Pink bars represent the plasma membrane.

5.4 Structural investigation of PIP_2 binding to Kir7.1

5.4.1 Grid screening and data collection

As described for the apo cryo-EM experiments, two data sets were ultimately collected for the Kir7.1-PIP_2 sample. Despite attempting to merge the data sets, similar to the apo sample, there was no improvement in the overall map quality and resolution. As a result, only the second data set was utilised for the final reconstructions and therefore this section will solely focus on describing the results obtained from the second data set.

22,098 movies were collected and imported into cryoSPARC for data processing. Motion correction and CTF estimation were conducted, and these parameters were used to curate the exposures to a final number of 22,012. Image processing was conducted similarly to the apo data set and is outlined in **Fig. 5.7**. Final non-uniform refinement with C4 symmetry produced a reconstruction at 3.29 Å with ~556,510 particles. DeepEMhancer was used to sharpen this map for visual inspection and manual building in Coot (**Fig. 5.8.A**). The cryoSPARC sharpened map was used for refinement.

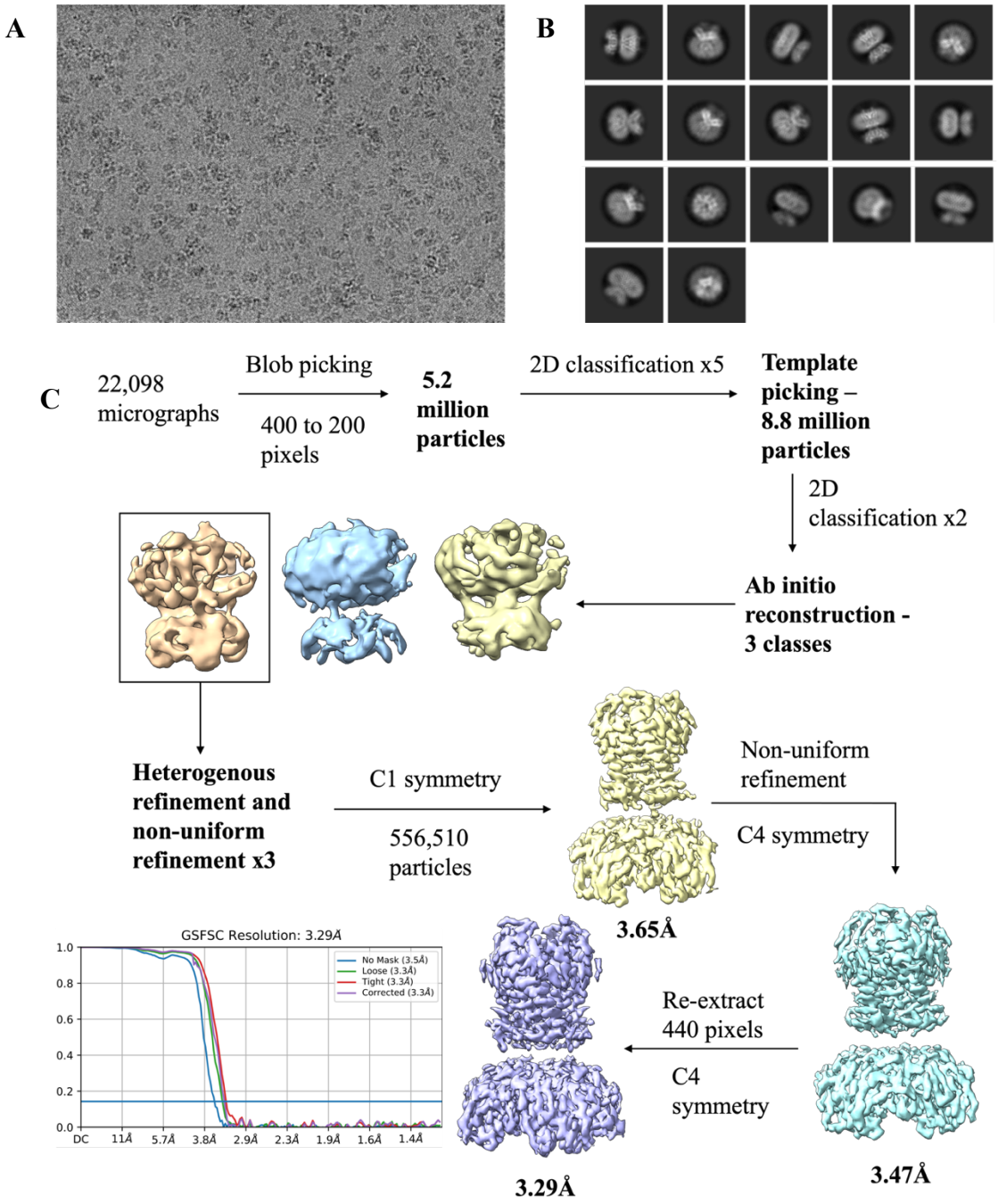

Figure 5.7. Image processing overview of Kir7.1-PIP$_2$ data set. A. Representative micrograph from the data collection. **B.** 2D class averages showcasing a range of views of Kir7.1 within the detergent micelle. **C.** Image processing workflow producing a final refinement of 3.29 Å with C4 symmetry.

5.4.2 Model building, refinement, and validation

Local resolution estimation was mapped onto the sharpened map showing the difference in resolution throughout the channel (**Fig. 5.8B**). As with the apo data set, a lower resolution was observed at the extremities of the channel and in the region between the TMD and the CTD (**Fig. 5.8B**). 3D variability analysis showed similar flexibility compared to the apo data set including the movement of the CTD in relation to the TMD. However, the overall resolution was higher in the dataset with PIP_2 compared to the dataset without PIP_2. Similar micrograph and particle numbers were collected for both samples which suggests that the presence of PIP_2 may contribute to the improved map resolution. The final Kir7.1-PIP_2 model had residues 17-28 and 38-324 built.

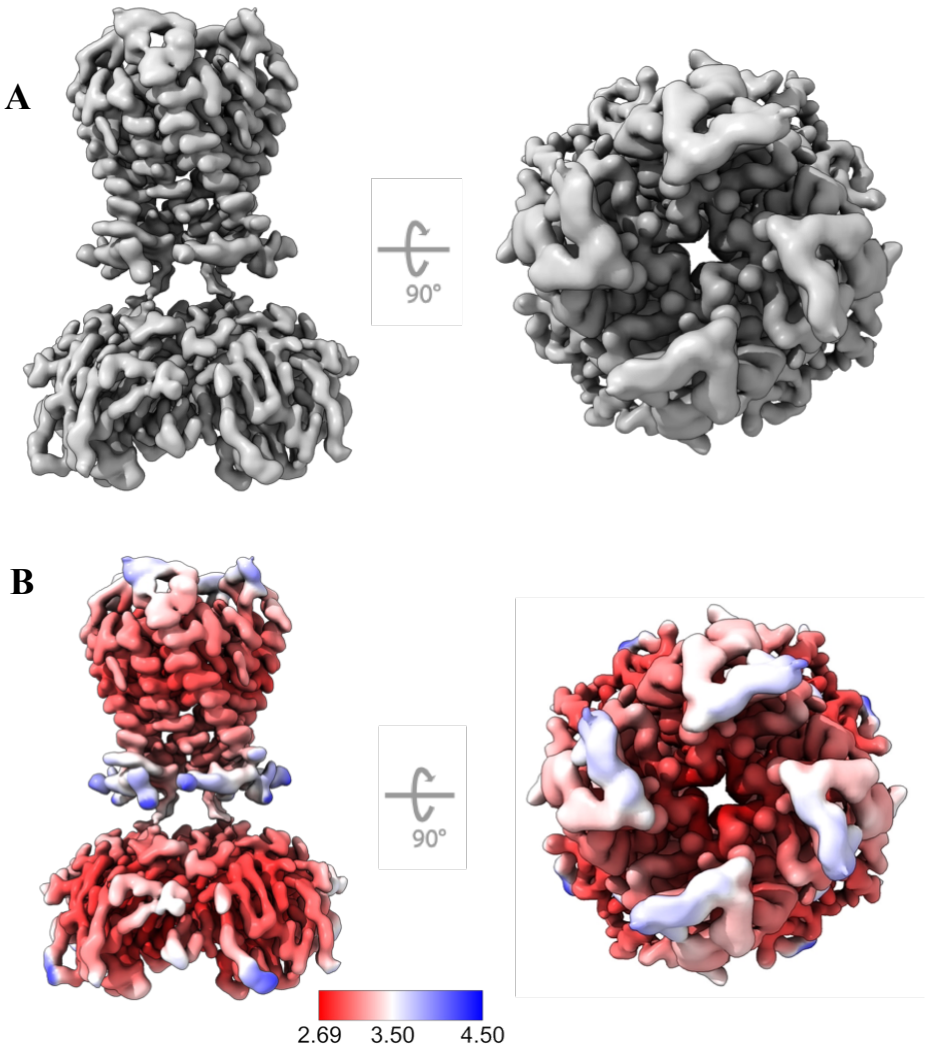

Figure 5.8. 3D reconstruction of Kir7.1 in complex with PIP_2. A. DeepEMhancer sharped map of Kir7.1 with PIP_2 present. A side-on view is shown on the left and a

top-down view is shown on the right. **B.** Local resolution estimation of the map. The colour scale is shown by the bar below, with units in Å.

5.4.3 Modelling of PIP_2 into the EM density

Previous studies on Kir channels activated by PIP_2 have shown that when PIP_2 is bound, there is a translation of the CTD towards the TMD. This structural arrangement is denoted as a "docked conformation" (**Fig. 1.4**). This cryo-EM sample with Kir7.1 and PIP_2 did not produce any 3D maps demonstrating CTD translation. Several approaches were used to investigate if any classes of particles within this data set existed with a docked conformation. 3D classification, utilising various numbers of classes, failed to detect any discernible differences among the classes.

Additionally, the cryo-EM map of GIRK2 in a docked conformation (PDB:6XIT) was imported to cryoSPARC, low pass filtered, and used to generate templates for template picking. This was intended to aid in finding any docked conformations if they existed within the dataset. However, even with these templates, no docked particles were identified within the data set.

Although the predicted CTD docking was not observed, there was an unmodelled density present within the known PIP_2 binding pocket. A PIP_2 molecule was placed into the unmodelled density for each subunit in Coot and the acyl chains were deleted until only the portion of PIP_2 within the density remained. Phenix eLBOW was used to generate ligand restraints and Phenix real-space refine was used on the model and PIP_2.

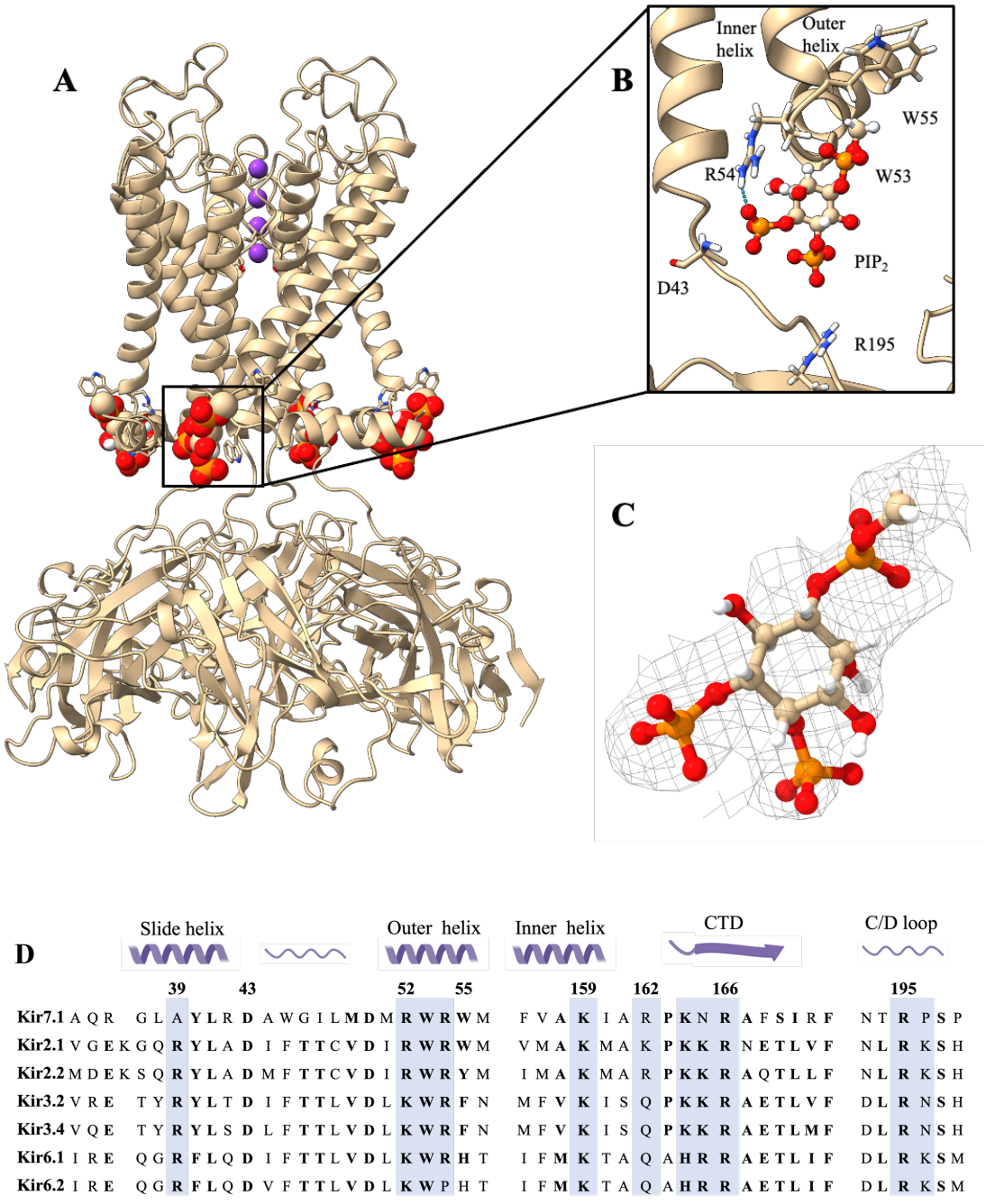

Figure 5.9. PIP_2 in complex with Kir7.1. A. Cryo-EM structure of Kir7.1 tetramer with four PIP_2 molecules bound. Kir7.1 is displayed as tan cartoon ribbons and the partial PIP_2 molecules are displayed as spheres. **B.** Zoom-in on one partial PIP_2 molecule bound to Kir7.1. Residues within 5 Å of the PIP_2 molecule are shown and labelled. R54 is capable of forming a hydrogen bond with PIP_2 and this is represented by a cyan dashed line. **C.** Isolated density of one PIP_2 molecule demonstrating ligand to map fit. **D.** An amino acid sequence alignment of eukaryotic Kir channels with published structural information. Residues previously identified as

interacting with PIP_2 are highlighted in blue. Residues are numbered according to Kir7.1. *CTD:* Cytoplasmic domain.

A model of Kir7.1 with PIP_2 partially modelled at each subunit was produced (**Fig. 5.9**). The binding site identified in this model is shared amongst Kir channels and other Kir structures have PIP_2 bound in the same location (Hansen et al., 2011; Niu et al., 2020). With PIP_2 modelled into this density the surrounding protein residues were analysed. The modelled segment of PIP_2 and Kir7.1 reveals that residues within 5 Å of the ligand include arginine 54, which exhibits the potential to form a hydrogen bond with PIP_2. (**Fig. 5.9B**).

Sequence alignment of Kir7.1 and all other Kir channels with published structural information was conducted, and residues implicated in binding PIP_2 were identified (**Fig. 5.9D**). Notably, residue 39 in Kir7.1 is an alanine, whereas in all other Kir channels, it is an arginine. However, despite this unique difference at residue 39, the Kir7.1 residues located in close proximity to PIP_2 are mostly conserved in other Kir channels. These conserved residues have previously been shown to be involved in PIP_2 binding, suggesting a shared mechanism of interaction with PIP_2 among different Kir channel members (**Fig. 5.9**).

5.4.4 Effect of PIP_2 binding to Kir7.1 detected by thermal unfolding

In addition to structural experiments, nano differential scanning fluorimetry (nanoDSF) was used to assess Kir7.1 properties. Purified protein was subjected to thermal unfolding and Tm values were used to investigate any changes to protein stability. Samples were prepared consisting of Kir7.1 only and Kir7.1 in the presence of increasing concentrations of C8-PIP_2. The Tm of each condition was tested in triplicate. The ΔTm for each PIP_2 concentration was calculated compared to the protein-only sample. Positive ΔTm values indicate an increase in melting temperature, reflecting enhanced stability, while negative values indicate a decrease in melting temperature, suggesting reduced stability.

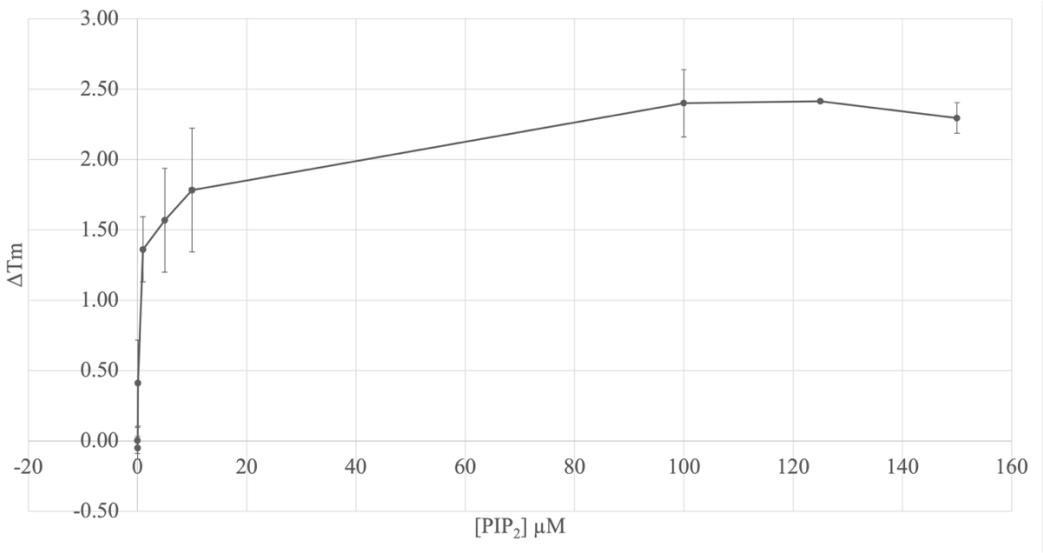

Figure 5.10. Impact of increasing PIP_2 concentrations on the ΔTm of Kir7.1. Each experimental condition was independently replicated at least twice, and the error bars indicate the variability between replicates. The y-axis represents the change in melting temperature (ΔTm) relative to the apo Kir7.1 (baseline condition).

Fig. 5.10 illustrates the dose-response of Kir7.1 ΔTm in relation to increasing concentrations of PIP_2. 100 µM of PIP_2 induced a 2.4 °C shift of the protein Tm, highlighting a stabilising effect of PIP_2. This work aids the structural analysis by further suggesting the binding of PIP_2 to Kir7.1, as the observed stabilisation of the Tm values in response to increasing concentrations of PIP_2 provides additional evidence for this interaction.

5.5 Structural analysis and comparison of Kir7.1 with and without PIP_2 bound

5.5.1. Helix bundle crossing in Kir7.1

The helix bundle crossing (HBC) is denoted as the region at the bottom of the inner M2 helices where a constriction of the channel occurs. **Fig. 5.11** highlights where the HBC exists within Kir7.1 and shows the two main residues implicated in this gating, threonine 153 and valine 157. Sequence alignment of this region with other Kir channels shows a variation of the residue present at these positions. At position 153 in other Kir channels, the amino acid is typically hydrophobic, while in Kir7.1, it is a polar threonine. At position 157, the residues are similar in that they all share hydrophobic properties. However, Kir7.1 possesses a smaller valine, while other Kir channels have larger residues like methionine and phenylalanine.

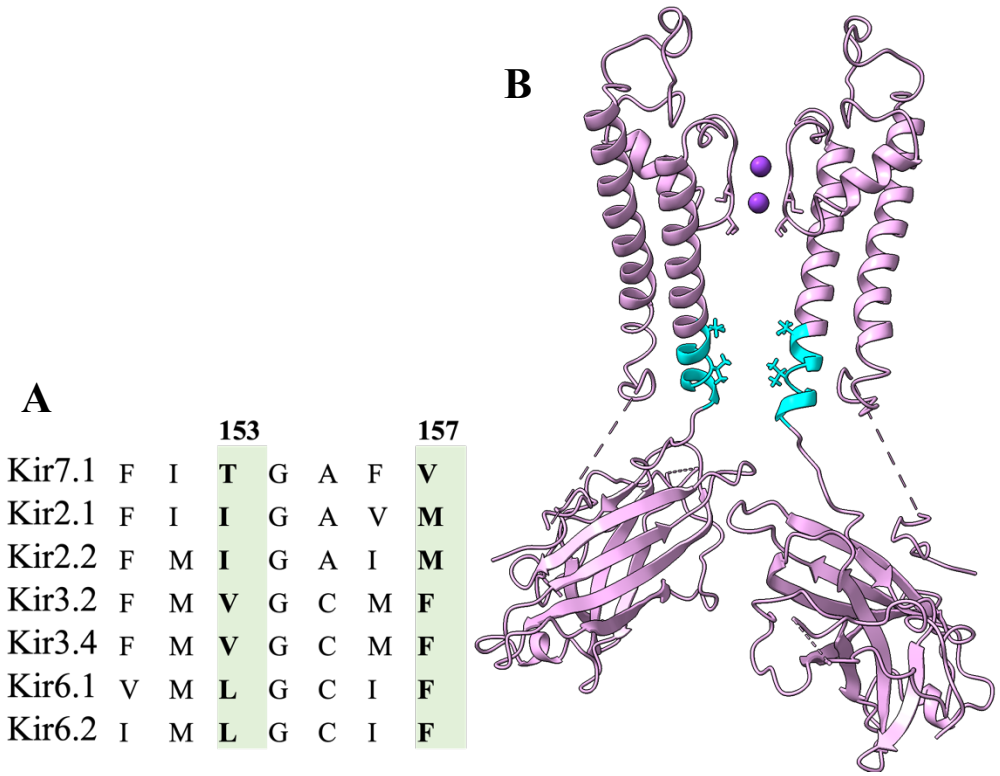

Figure 5.11. Analysis of the helix bundle crossing in Kir7.1. A. Sequence alignment of all Kir channels with published structural information. The two residues implicated in the helix bundle crossing are shown in bold and highlighted in green. Residues are numbered according to Kir7.1. **B**. Model of apo Kir7.1 with the helix

bundle crossing coloured in cyan. Only two subunits of the tetramer are shown for clarity. The side chains of T153 and V157 are displayed.

5.5.2 Movement of residues and widening of the helix bundle crossing

When comparing the apo Kir7.1 model with the Kir7.1-PIP_2 model, a noticeable change was evident in the HBC region. The threonine residue at position 153 appears in a different position in each structure. In the apo model, the oxygen of the threonine side chain is oriented inward, directed towards the channel pore. In contrast, in the PIP_2-bound model, the threonine side chain has been reoriented, causing the oxygen to point in the opposite direction (**Fig. 5.12**). This movement of the threonine side chain alters the diameter of the HBC. When measured in ChimeraX without Van der Waals radii, the distance between the threonine side chains changes from 7.8 Å in the apo model to 9.2 Å in the PIP_2 model. Similarly, valine at position 157 shows an increase in the distance between side chains when PIP_2 is present. The distance changes from 6.9 Å to 8.5 Å although side chain reorientation is not observed.

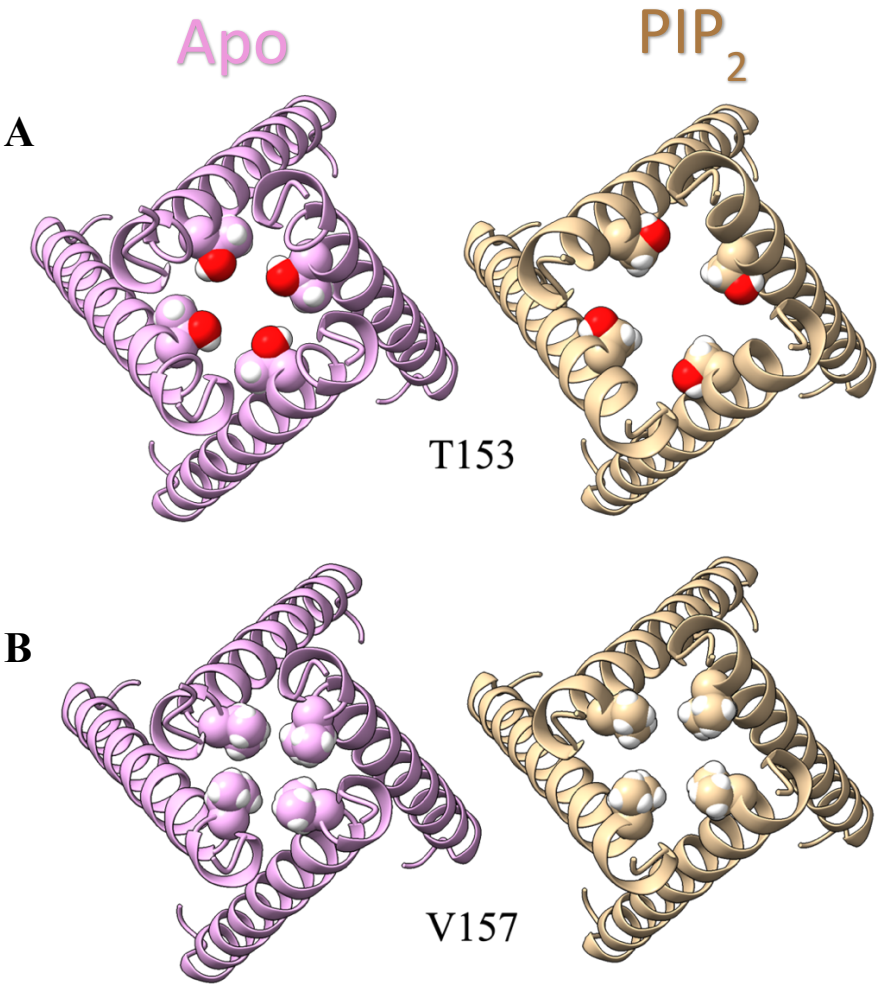

Figure 5.12. Movement of residues and widening of the helix bundle crossing in Kir7.1. The apo model is shown in tan and the PIP_2 model is shown in pink. Only inner M2 helices are shown viewed from the intracellular side. **A.** Residue T153 is shown as spheres and coloured by heteroatom with oxygen shown in red and hydrogen in white. **B.** Residue V157 is represented as spheres with hydrogens coloured white.

5.5.3 Bending of inner M2 helices

Movement of the side chains within the HBC appears to be caused by a slight bending of the inner M2 helices. When comparing the M2 helices from the apo and PIP_2-bound models, it was evident that the M2 helix moved outward towards the PIP_2 binding site (**Fig. 5.13A**). Residues located at the bottom of the M2 helix and within the flexible linker region are known to be conserved among Kir channels, as they play a crucial role in interacting with PIP_2.

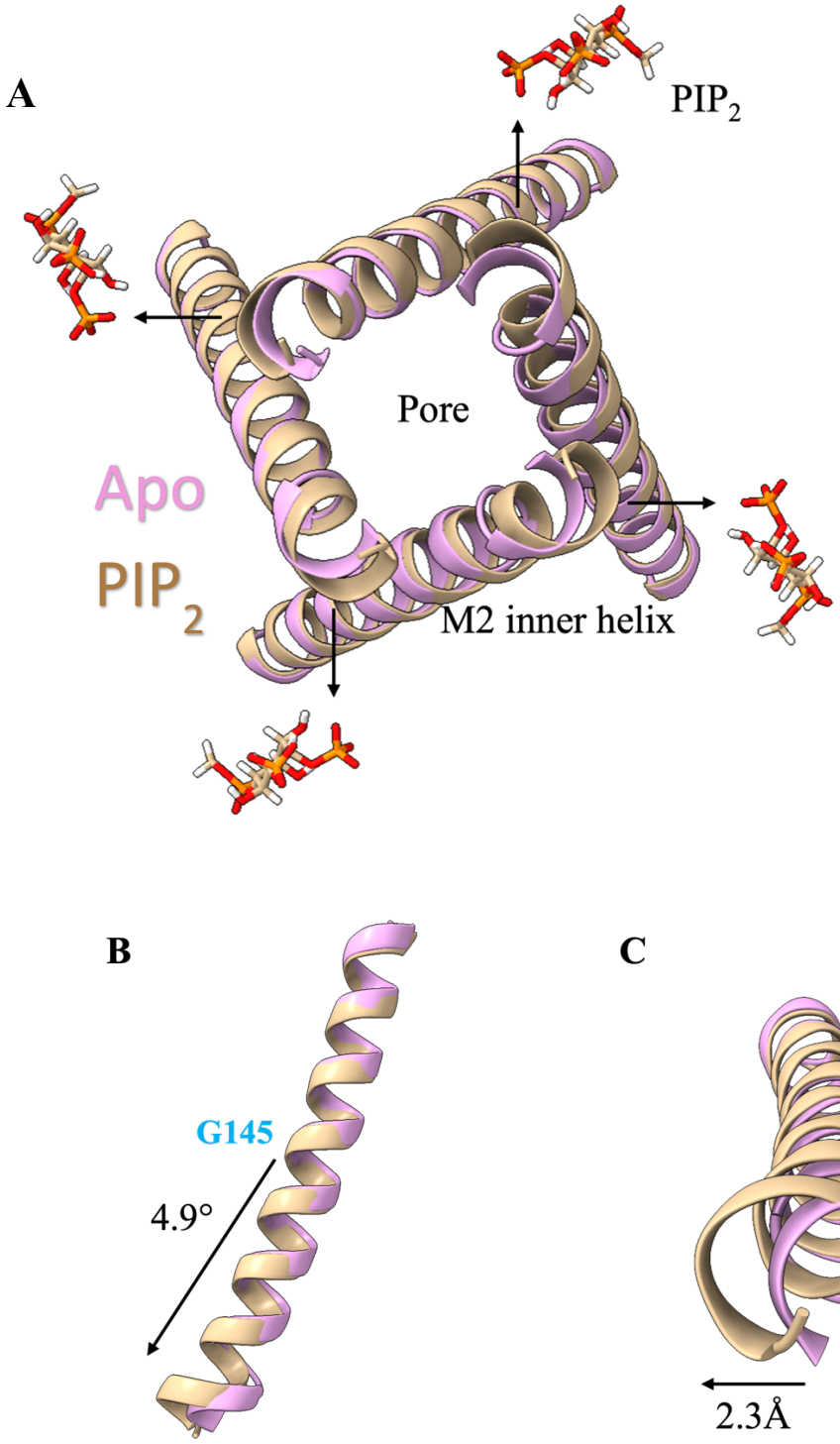

Figure 5.13. Inner M2 helix movement in Kir7.1 PIP_2 model. The apo model is shown in tan and the PIP_2 model is shown in pink. **A.** 4.9 ° bending of the inner helix observed in the PIP_2 model compared to the apo model. Bending originates at glycine 145, labelled in blue. **C.** At the bottom of the M2 helix, the PIP_2-bound

model exhibits a splayed-outward conformation that is 2.3 Å different compared to the apo model.

The angle between the M2 helix in the apo model and the M2 helix in the PIP_2 model was analysed. The investigation revealed that the bending of the helix in the PIP_2 model originated at glycine 145 (**Fig. 5.13B**). This conserved glycine residue is found in all Kir channels and has been recognised as crucial for the bending of the helix and the opening of the HBC. The M2 helix in the PIP_2 structure bends at a 4.9 ° angle compared to the apo structure. As a result of this bending, the end of the M2 helix in the PIP_2-bound model is positioned 2.3 Å further away compared to the apo model.

5.5.4 Channel properties implicated by pore widening

The movement and widening of the helix bundle crossing is likely involved in Kir7.1 channel activity. Channel pore radius analysis was performed using HOLE2 and visualised using the visual molecular dynamics program (Humphrey et al., 1996; Smart et al., 1996). In the apo Kir7.1 model, pore constriction points were observed at the HBC, whereas the Kir7.1-PIP_2 model displayed a more dilated pore with less constriction (**Fig. 5.15A and B**). A pore radius graph for each model was produced and overlayed to draw comparisons (**Fig. 5.14C**). The selectivity filter exhibited similar pore size in both models but at the HBC the PIP_2 model showed a wider pore radius compared to the apo model. At the most constricted point of the HBC in the PIP_2 model, the pore diameter is ~4.8 Å which is likely too constricted to allow the passage of hydrated potassium ions. The apo model at this same point is only 3.3 Å in pore diameter (**Fig. 5.14**).

Additionally, the G-loop gate appears to have different pore radius profiles in the apo and PIP_2 models. Although the apo model appears more constricted than the PIP_2 model in some regions, all parts of the G-loop are above the 6 Å threshold and are dilated enough to facilitate hydrated potassium ion conduction (**Fig. 5.14C**). The HOLE2 profiles of the apo and PIP_2 models demonstrate that the apo model is more constricted overall compared to the PIP_2-bound model.

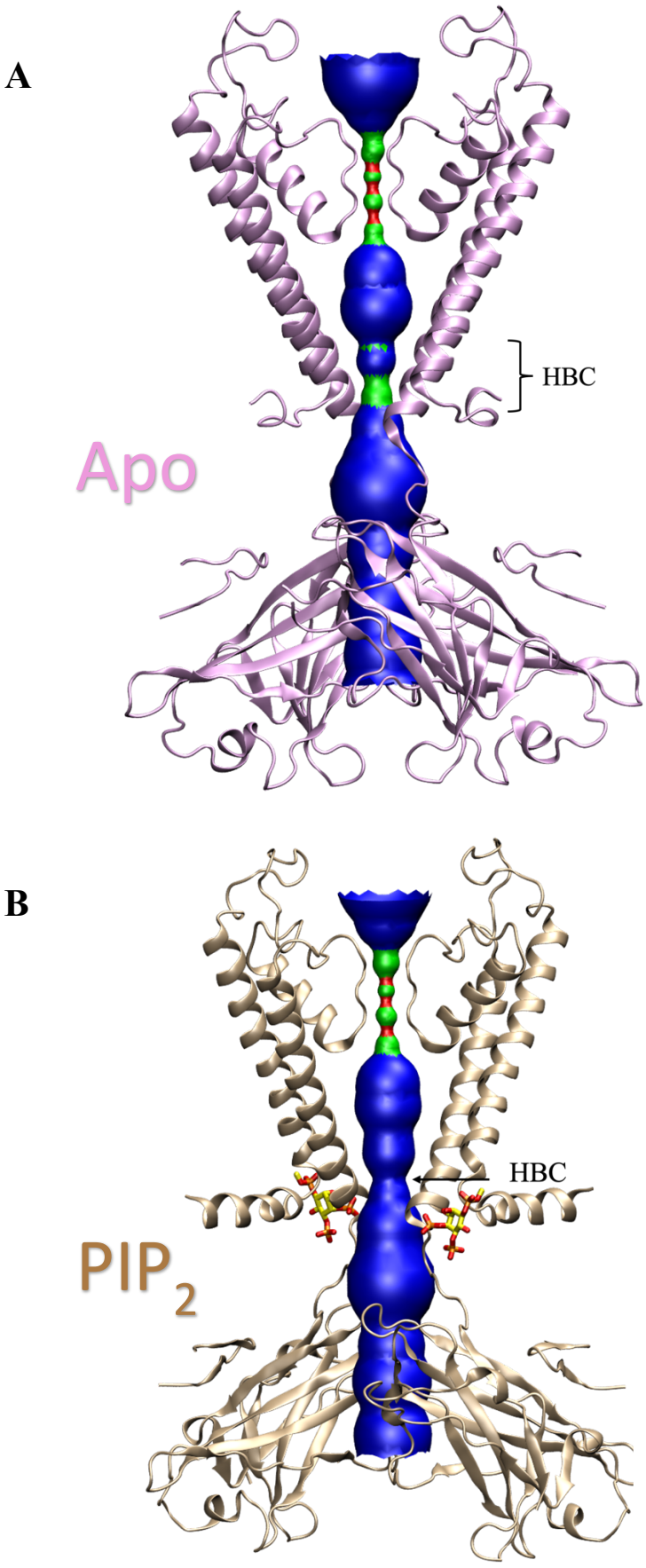
A
HBC
Apo
B
HBC
PIP2

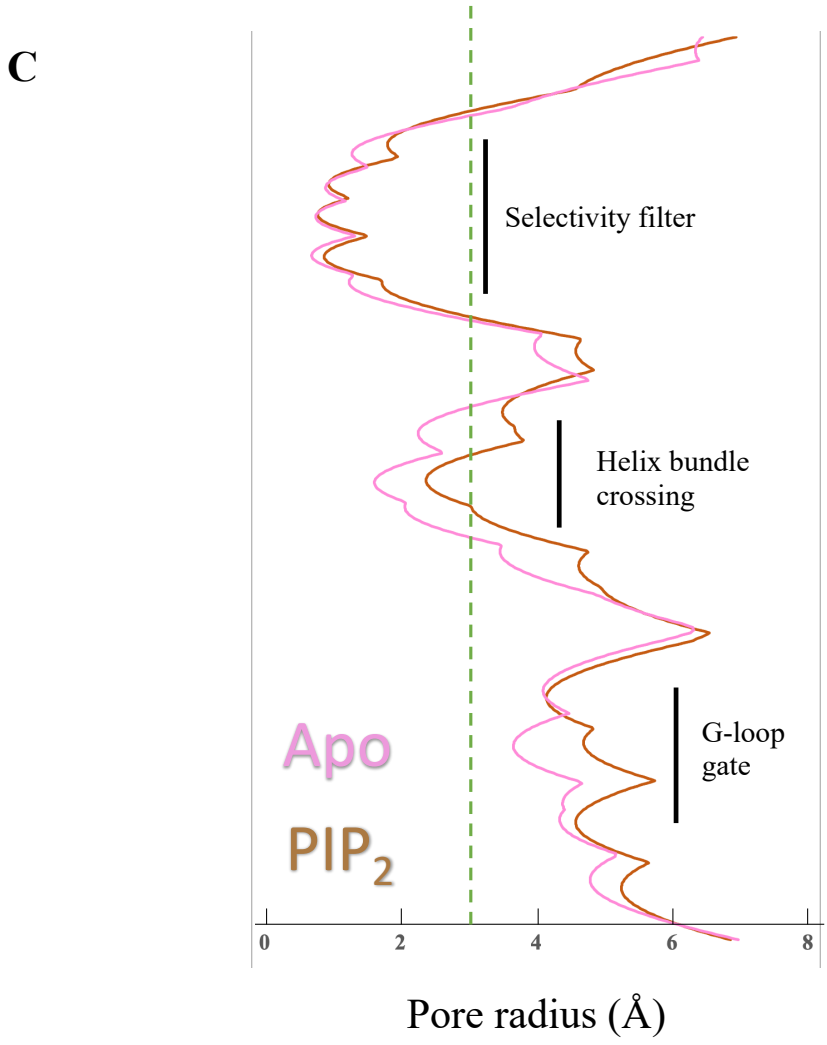

Figure 5.14. Pore radius analysis of apo Kir7.1 and Kir7.1-PIP$_2$. The apo model is shown in tan and the PIP$_2$ model is shown in pink. **A.** The apo Kir7.1 model with a HOLE2 profile showing pore radius. Two subunits of the tetramer are shown with the HBC labelled. **B.** Kir7.1-PIP$_2$ model with a HOLE2 profile showing the pore radius. Two subunits of the tetramer only are shown. A PIP$_2$ molecule is shown bound to each subunit. The HBC is labelled. Green represents a radius of 1.15-2.3 Å and red represents a radius less than 1.15 Å. Blue displays a radius larger than 2.3 Å. **C.** Graph representation of HOLE2 profiles of the apo and PIP$_2$ models. The selectivity filter, helix bundle crossing, and G-loop gate are labelled. The pore radius is labelled across the x-axis and a green dashed line at 3 Å represents the lower limit for hydrated potassium radius.

5.6 Summary

This chapter centred on cryo-EM and structural analysis of the novel Kir7.1 channel, both in the absence and presence of the activating phospholipid PIP_2. The cryo-EM sample preparation was thoroughly optimised, and despite initial challenges in data collection, suitable conditions were established to ensure data quality sufficient for generating 3D reconstructions. The Kir7.1 apo map was resolved to a resolution of 3.5 Å, while the Kir7.1-PIP_2 map was produced at a slightly higher resolution of 3.3 Å. Both maps exhibited intrinsic flexibility within the data sets, which restricted the overall resolution. This flexibility was particularly evident between the transmembrane and cytoplasmic domains, suggesting its potential relevance to the function of the protein. The Kir7.1 apo model was constructed using ModelAngelo and manual building in Coot. Partial building of PIP_2 into the EM density was accomplished in the Kir7.1-PIP_2 map. Subsequently, both structures were compared, and the structural analysis revealed a widening of the HBC in the PIP_2 model compared to the apo model. The observed widening is attributed to the bending of the inner M2 helix and its movement out towards the PIP_2 molecule.

Chapter 6

6. Characterisation of Kir7.1 disease-associated mutants

This chapter focuses on the effect of disease-associated mutations on the function of Kir7.1. Snowflake vitreoretinal degeneration (SVD) and Leber congenital amaurosis (LCA) are two rare retinal diseases that are currently without any treatment option. The gene *KCNJ13*, responsible for encoding Kir7.1, has been implicated in the pathogenesis of both diseases. Various mutations in Kir7.1 have been identified in individuals with SVD and LCA (**Table 6.1**). A loss-of-function of Kir7.1 is the proposed effect of all of these mutations, although a thorough characterisation has not been published to date. Therefore, this portion of the thesis will focus on a preliminary characterisation of the disease-associated mutations, with an emphasis on the R162W mutation responsible for SVD.

6.1 Generation of disease-associated constructs and evaluation of expression levels

Site-directed mutagenesis was employed on the full-length Kir7.1 sequence to create constructs for expressing each disease-associated mutant. Expi293 cells were used in a small-scale format (3 mL) to express each disease mutant. Conditions that were previously determined as optimal for expression of the WT protein were used: 48 hours of incubation at 37 °C (**Section 4.3.1**). A FLAG-pulldown was conducted to purify the protein and expression levels were measured by SDS-PAGE with silver staining and WB analysis (**Fig. 6.2**).

Mutation	Protein location	Disease
S105I	Transmembrane domain	LCA
I120T	Selectivity filter	LCA
T153I	Transmembrane domain	LCA
R162W	PIP_2 binding domain/flexible linker	SVD
R166*	PIP_2 binding domain/ flexible linker	LCA
Q219*	Cytoplasmic domain	LCA
L241P	Cytoplasmic domain	LCA

Table 6.1. Disease-associated mutations in Kir7.1. Mutations in Kir7.1 that have been identified in individuals with either LCA or SVD. The mutation, its location within the protein and the disease it's associated with is outlined. * Represents a stop codon. *LCA:* Leber congenital amaurosis, *SVD:* Snowflake vitreoretinal degeneration.

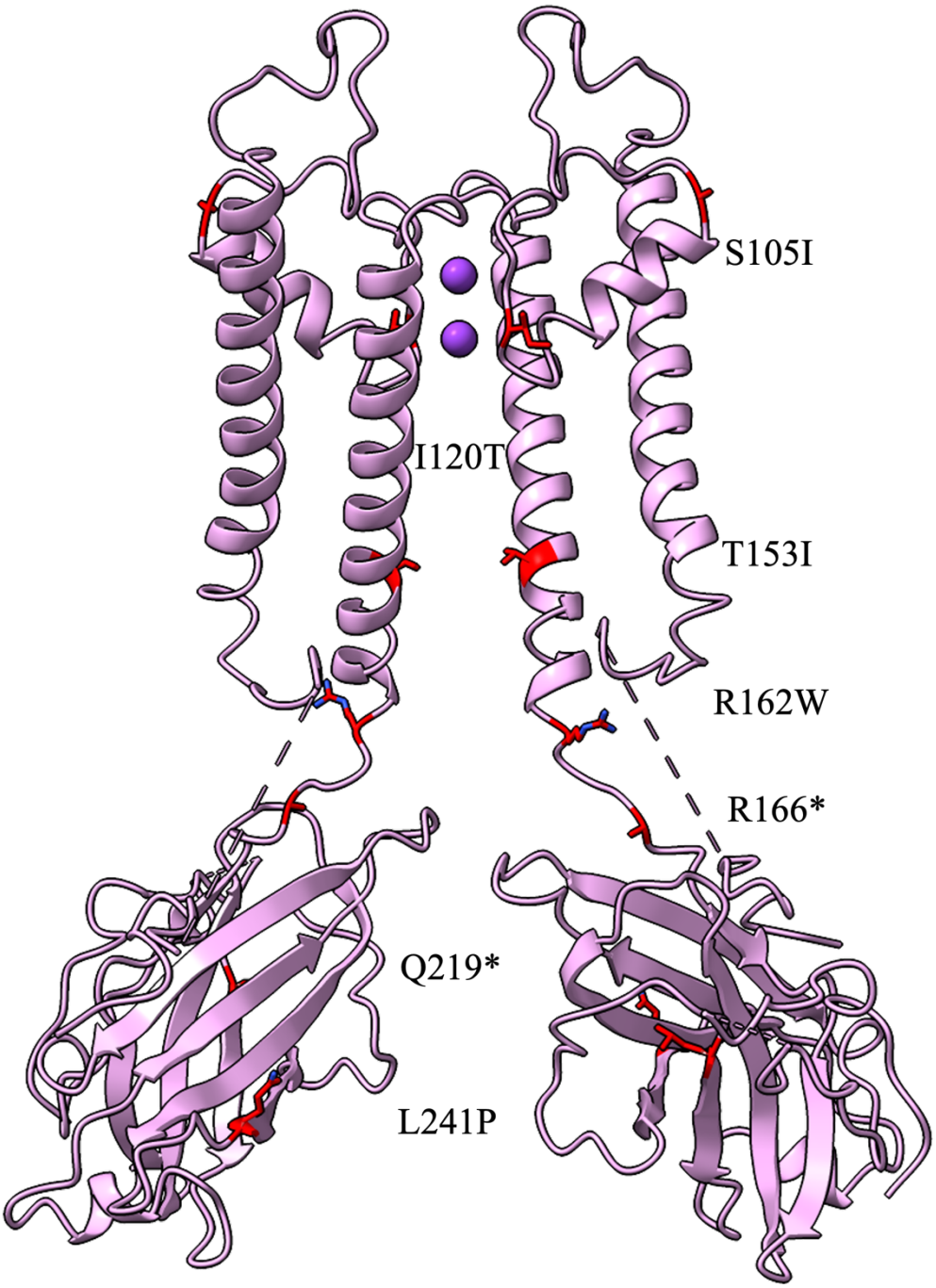

Figure 6.1. Mapping of mutations associated with SVD and LCA onto the Kir7.1 structure. Residues within Kir7.1 that are mutated in either LCA or SVD are coloured red and have their side chains shown in ball and stick. Two subunits of the channel are shown for clarity and mutations are labelled. The R162W mutation is associated with SVD, and all other mutations are linked with LCA.

WB analysis investigated both the soluble fraction of the cell lysate and the purified protein (**Fig. 6.2B**). This enabled the identification of proteins that could potentially be expressed but may be unstable or unable to be purified by the N-terminal FLAG tag. Silver-stained SDS-PAGE was used to analyse the purified protein samples as this gave a more accurate comparison between expression levels (**Fig. 6.2A**).

Firstly, both R166* and Q219* showed no discernible expression levels (**Fig. 6.2A and B**). These mutants both possess early stop codons making them unlikely to produce folded, functional proteins. From SDS-PAGE and WB analysis, it appeared that mutants T153I, R162W and L241P were expressed in sufficient amounts. The I120T protein showed expression in the cell lysate but this amount was greatly reduced in the purified samples when analysed by WB and SDS-PAGE (**Fig. 6.2A and B**). For purified protein samples, only T153I and R162W showed higher oligomeric states as evidenced by the bands that exhibit a resemblance to the WT pattern (**Fig. 6.2B**). This implies that both of these mutants may be in the folded tetrameric form. Therefore, these two variants were selected for further evaluation.

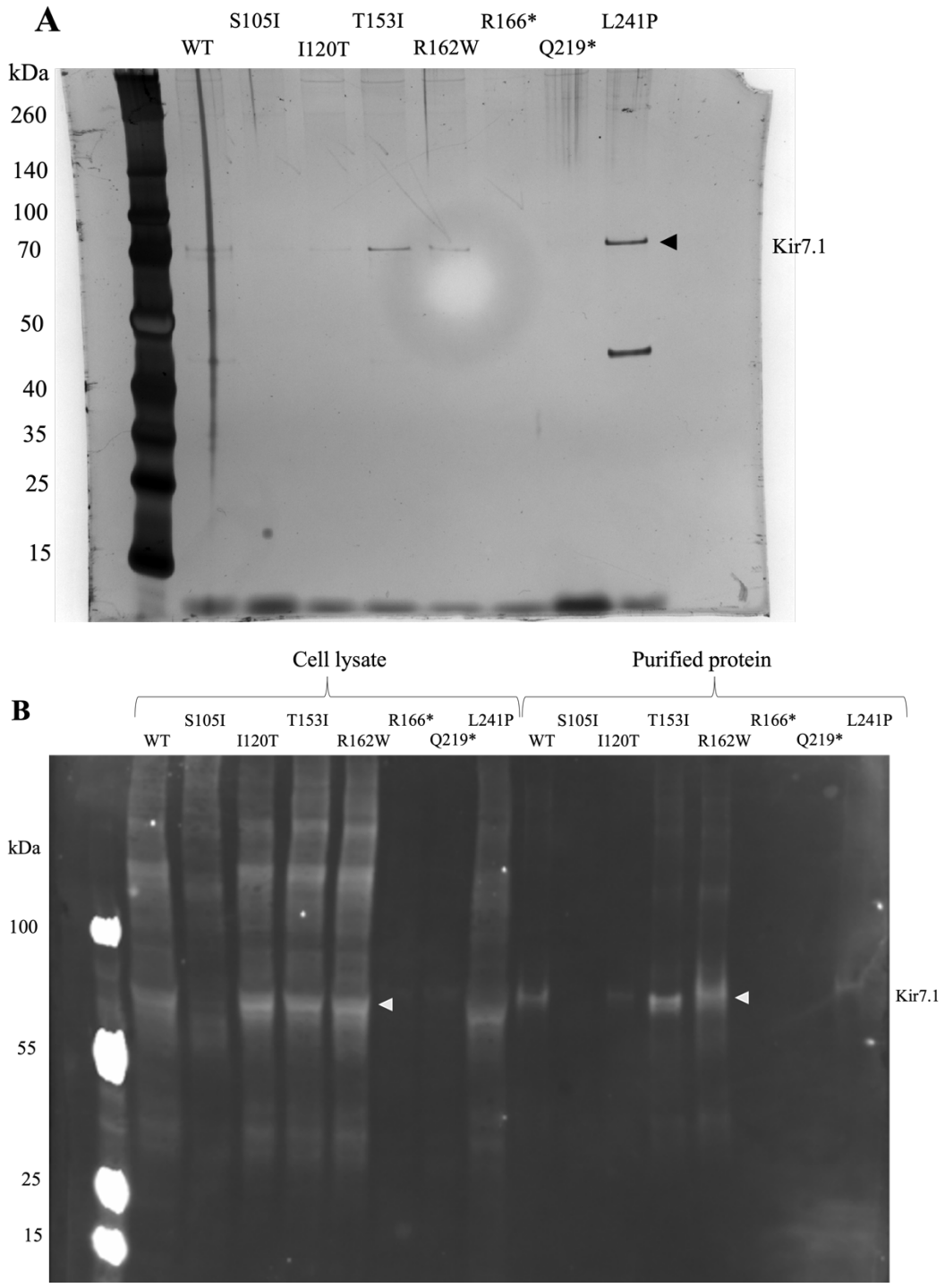

Figure 6.2. Analysis of Kir7.1 mutant expression levels through SDS-PAGE and western blot. A. SDS-PAGE of purified proteins analysed with silver stain. Monomeric bands are identified at the 70 kDa marker. The protein sample in each lane is labelled above. **B.** Western blot analysis of whole cell lysate and purified protein. An anti-Kir7.1 antibody was used for detection. Monomers are identified at approximately 70 kDa and higher oligomeric states can be identified in some lanes.

6.2 Large-scale expression and purification of constructs

Based on the initial expression tests, the mutants T153I and R162W were evaluated for expression and purification in a large-scale format. The optimised purification protocol established for the WT protein was used for both mutants (**Section 4**). The size exclusion profiles of both mutants closely resembled that of the WT (**Fig. 6.3**), albeit with a slightly reduced yield for each mutant. Elution peaks were observed at approximately the same volume as WT suggesting a folded tetrameric version of the mutants (**Fig. 6.3**).

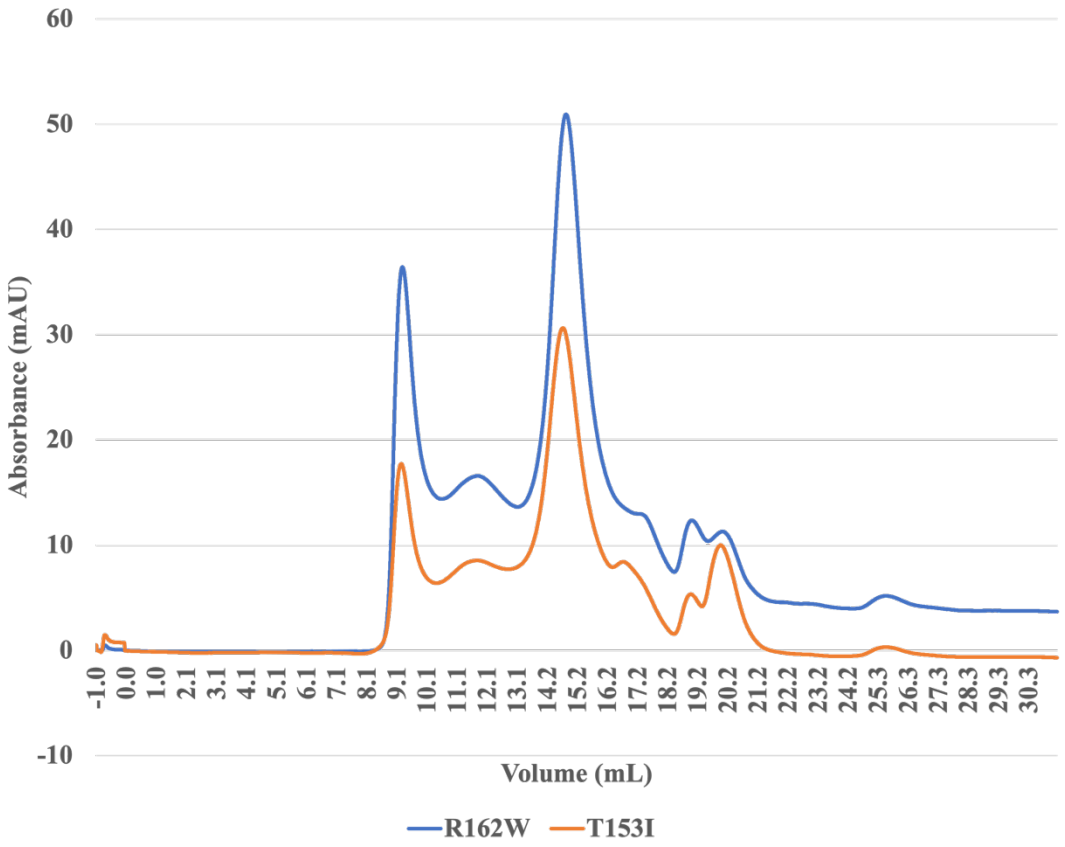

Figure 6.3. Size exclusion chromatograms of R162W and T153I mutants. Both mutants were subjected to size exclusion chromatography using the same methodology as applied to the WT protein. R162W is represented by the blue trace and T153I is represented by the orange trace. Elution peaks at ~14.8 mL represent tetrameric protein.

6.3 Structural analysis of Kir7.1-R162W

Large-scale purification of T153I and R162W mutants was successful at producing purified, tetrameric proteins. To prioritise structural investigations, resources and efforts were concentrated on the R162W mutant, given its exclusive association with SVD. Therefore, R162W was expressed in 8 litres of HEK293 cells and purified with the protocol established for WT protein (**Section 4**). This produced sufficient protein for EM grid preparation. Grids were prepared using the conditions that were optimised for the WT protein (**Section 2.8.4**). From initial grid screening, particles appeared homogenous and evenly distributed appearing suitable for high-resolution data collection.

6.3.1 3D reconstruction of Kir7.1-R162W

A data set consisting of 22,423 micrograph movies was collected and imported into cryoSPARC. The data set was processed similarly to the previously successful WT protein dataset (**Section 5.4**). The notable difference is that *ab initio* reconstruction was not necessary, as a 3D volume was imported from the apo data set (**Fig. 6.4C**). The volume was low pass filtered to 10 Å and used as an initial volume in heterogeneous refinement. A 'bad' volume, from the PIP_2 data set, was used three times in the heterogeneous refinement to filter particles into the good and bad classes (**Fig. 6.4C**). This was conducted in an iterative process alongside non-uniform refinement until no further improvement of the map was observed.

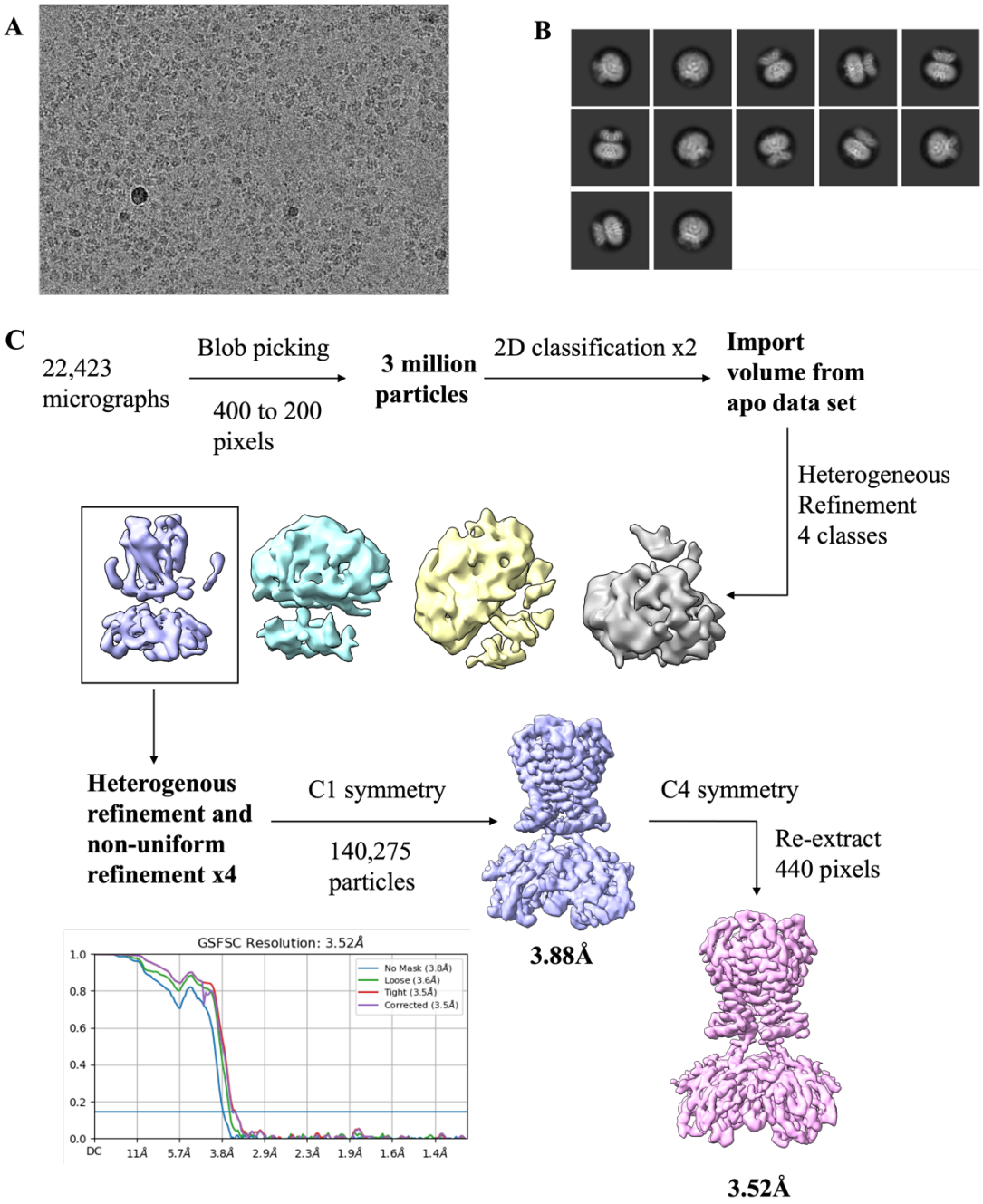

Figure 6.4. Image processing overview of Kir7.1-R162W data set. A. Representative motion corrected micrograph. **B.** 2D classes showing various views of Kir7.1-R162W. **C.** Image processing workflow producing a final refinement of 3.52 Å with C4 symmetry.

A final consensus refinement was achieved using non-uniform refinement with C4 symmetry enforced. DeepEMhancer was used for sharpening the map and local resolution was estimated and the map was coloured accordingly (**Fig. 6.5B)**. Comparable regions display low resolution in both the Kir7.1-R162W and apo Kir7.1 maps (**Fig. 5.5B and 6.5B**). The core portion of the protein remains the most highly resolved likely due to increased stability and rigidness within these regions.

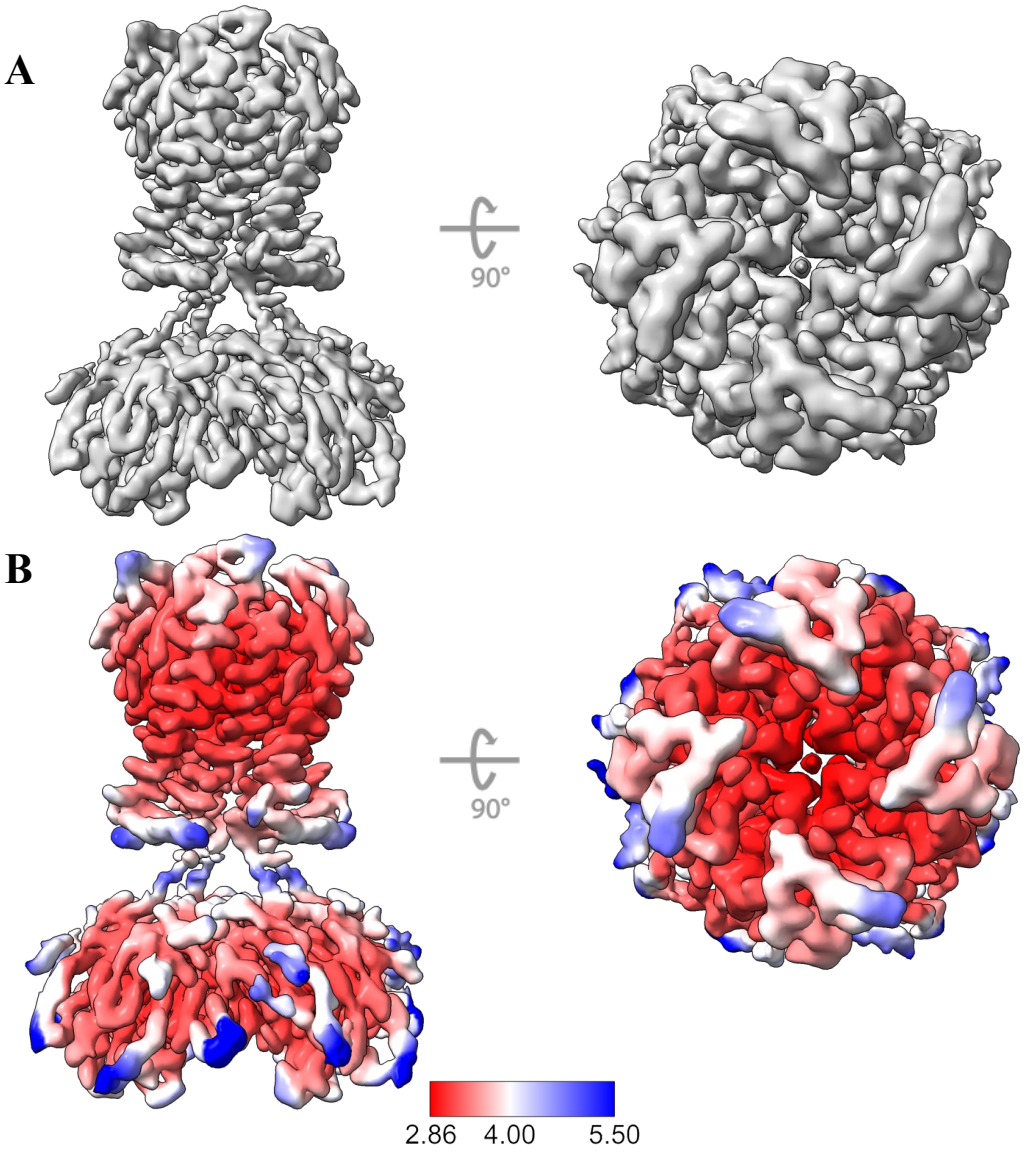

Figure 6.5. EM density map of Kir7.1-R162W. A. EM map sharpened using DeepEMhancer showing a top-down and side-on view of the channel. **B.** Sharpened map coloured by local resolution. The colour scale is shown by the bar underneath, with units in Å.

6.3.2 Kir7.1-R162W model

The previously built and validated apo Kir7.1 model (**Section 5.4.2**) was placed into the Kir7.1-R162W EM map and residue 162 was mutated to tryptophan in Coot. The model was refined and manually built until a good model-to-map fit was achieved. The final model had residues 17-38, 38-229 and 318-324 built and exhibited similar structural features compared to apo Kir7.1. The mutated residue, at position 162, located in the TMD-CTD linker showcases different properties in each model (**Fig. 6.6B and C**). In the apo WT model, the R162 side chain points outwards from the channel pore (**Fig. 6.6C**). However, in the Kir7.1-R162W model, the tryptophan is positioned inwards into the channel pore (**Fig. 6.6B**). This mutation results in a bulky hydrophobic amino acid lying within the channel pore.

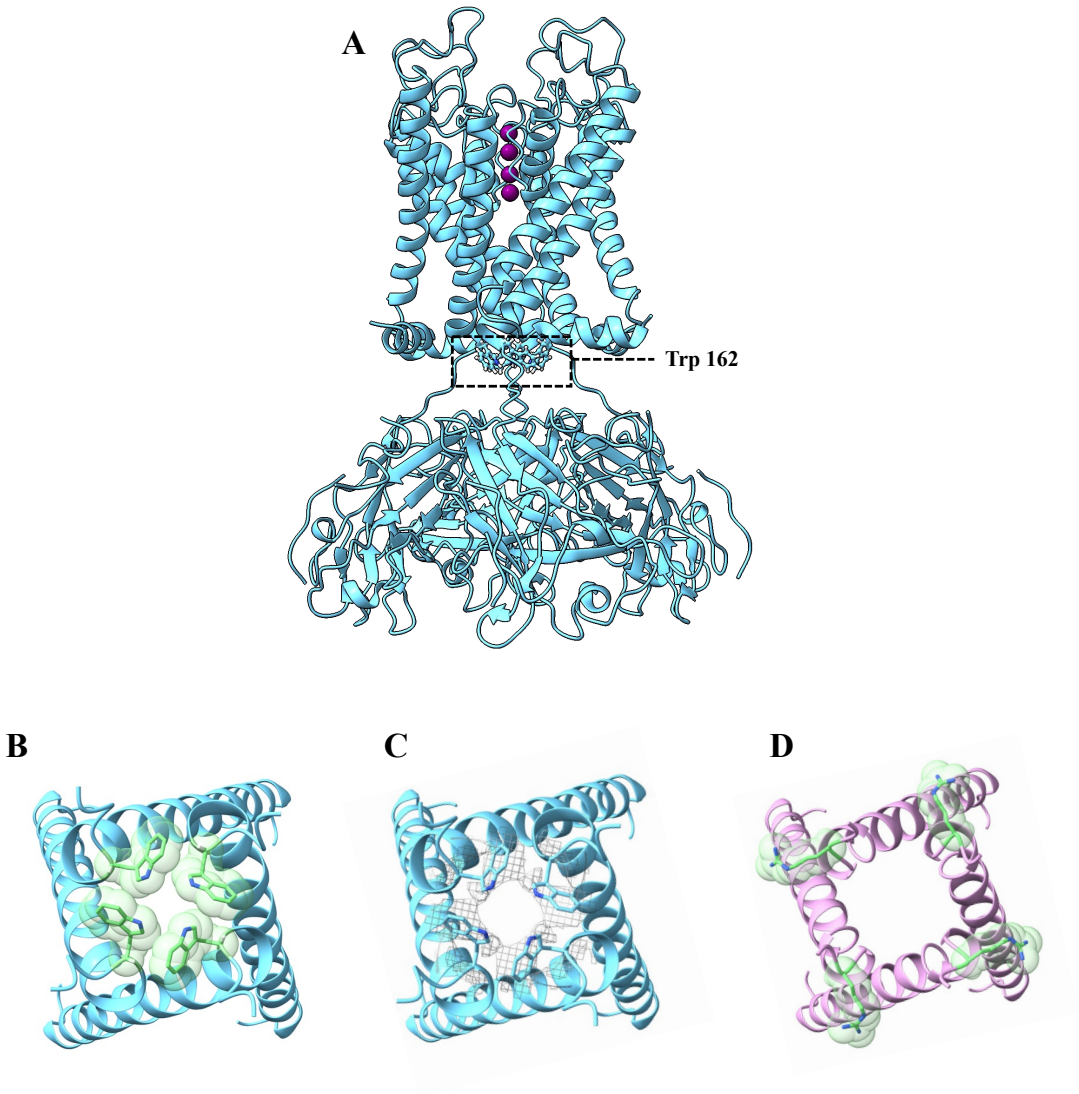

Figure 6.6. Kir7.1-R162W model showcasing the disease-associated mutation. A. Full Kir7.1-R162W model showing tryptophan 162 in the TMD-CTD linker region. Potassium ions within the selectivity filters are shown coloured purple. **B.** Zoomed-in view of the R162W mutation from the intracellular side of the pore overlaid with semi-transparent space-filling models. **C.** Zoomed-in view of R162W with densities shown in grey mesh visualised at a contour threshold of 0.971. **D.** Zoomed-in view of R162 in the apo Kir7.1 model. Arginine side chains are shown overlaid with semi-transparent space-filling models. Kir7.1-R162W is coloured blue and apo Kir7.1 is coloured pink.

6.4 Analysing the pore radius of Kir7.1-R162W

Due to the position of the tryptophan mutation, it was of interest to analyse the Kir7.1-R162W channel's pore size. HOLE2 analysis identified points of constrictions along the pore (**Fig. 6.7A**). At position 162, a new constriction point exists that wasn't present in the WT protein (**Fig. 6.8**). The bulky tryptophan present in the mutant protein points inward into the pore (**Fig. 6.7**) introducing a constriction point that may be capable of impeding ion translocation. HOLE2 analysis shows that the pore radius at the point of the tryptophan is 1.3 Å which is too narrow for a hydrated potassium ion to pass through.

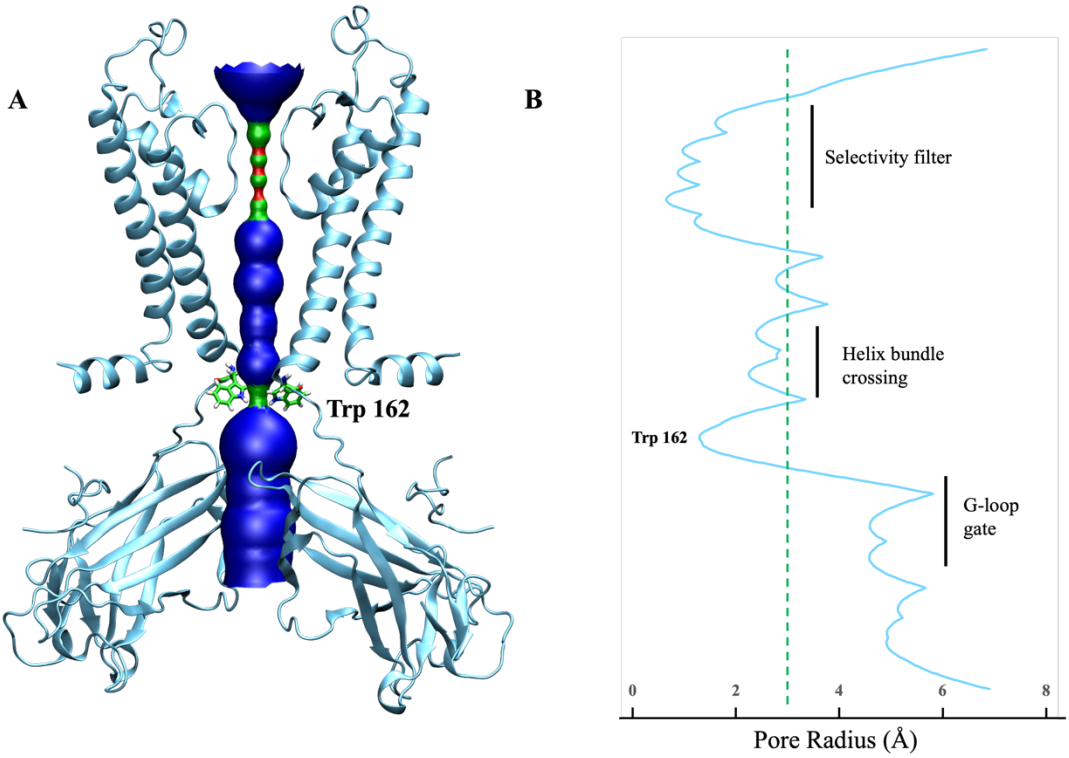

Figure 6.7. Pore radius analysis of Kir7.1-R162W. A. The Kir7.1-R162W model with a HOLE2 profile showing pore size. Two subunits of the tetramer are shown with tryptophan 162 side chains shown. Green represents a radius of 1.15-2.3 Å and red represents a radius less than 1.15 Å. Blue displays a radius larger than 2.3 Å. **B.** Graph representation of the HOLE2 profile of Kir7.1-R162W. The selectivity filter, helix bundle crossing, and G-loop gate are labelled. The pore radius is labelled across the x-axis and a green dashed line at 3 Å represents the lower limit for a hydrated potassium ion radius.

6.5 Pore radius comparison of apo Kir7.1 and Kir7.1-R162W

To understand the implications of the R162W mutation, the mutant channel was compared to the WT channel. The apo Kir7.1 model was used for comparison as it represents the protein with no PIP_2 influence. The overall HOLE2 profile in the TMD looks more constricted in Kir7.1-R162W compared to apo Kir7.1 (**Fig. 6.8**). The position at residue 162 appears much narrower in Kir7.1-R162W than in apo Kir7.1.

By plotting the HOLE2 profiles, it is possible to analyse the regions of the channel incapable of allowing conduction. A pore radius threshold of 3 Å is established, considering that a hydrated potassium ion typically has an average diameter of 6.6 Å, ranging from 6 to 8 Å (O'M. B., 1982). A comparison of apo and Kir7.1-R162W profiles shows the difference in pore radius at position 162 (**Fig. 6.8C**). The pore changes from having a radius of 3.5 Å in the WT protein to 1.3 Å in Kir7.1-R162W at this position. In the mutant channel, this constriction point is formed by hydrophobic side chains, contrasting with the positively charged arginine side chains present in the WT channel.

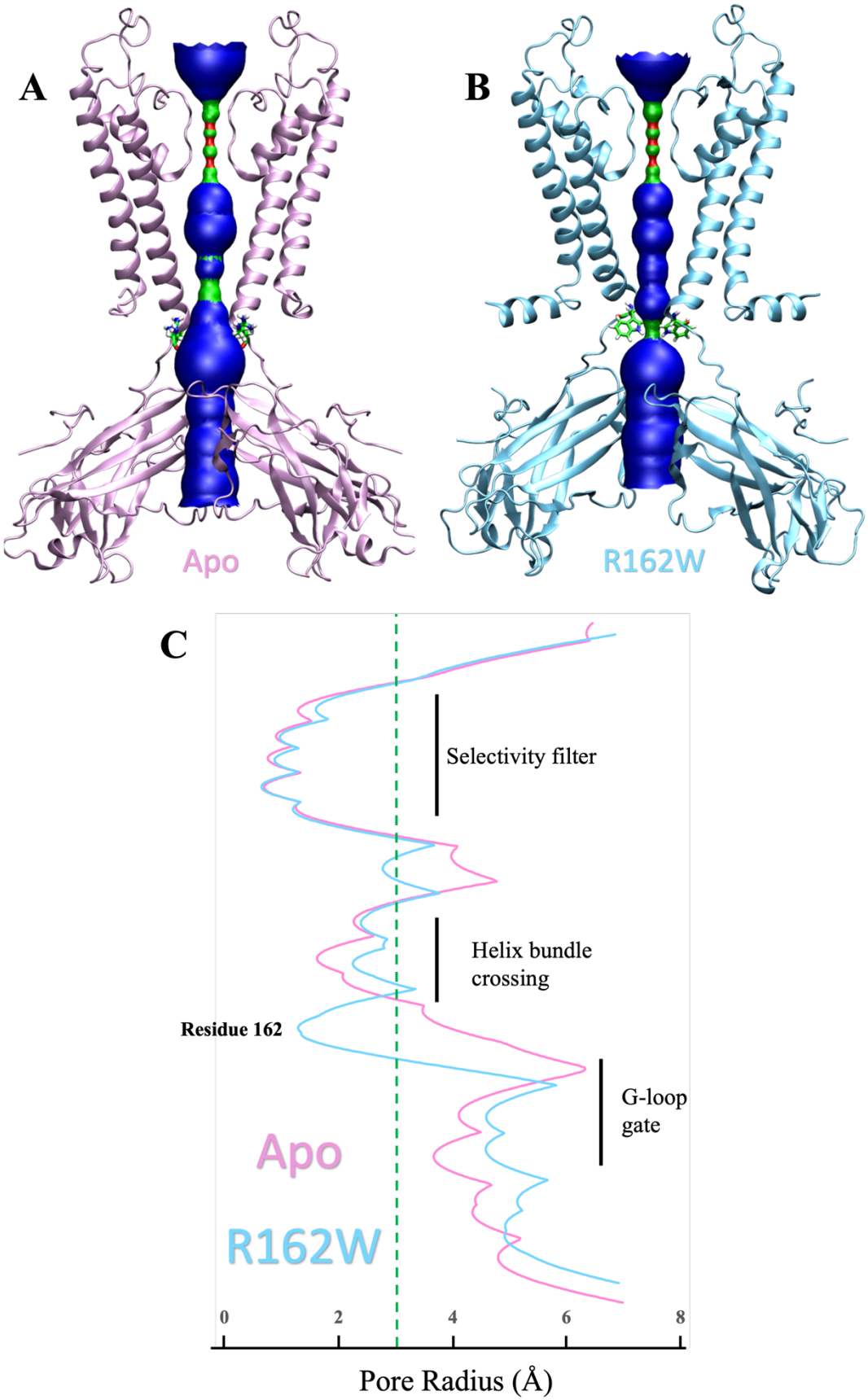

Figure 6.8. HOLE2 profiles of apo Kir7.1 and Kir7.1-R162W models. A. The apo Kir7.1 model with a HOLE2 profile showing pore size. **B.** The Kir7.1-R162W model

with a HOLE2 profile showing pore size. Two subunits of each tetramer are shown with residue 162 side chains shown. Green represents a radius of 1.15-2.3 Å and red represents a radius less than 1.15 Å. Blue displays a radius larger than 2.3 Å. Apo Kir7.1 is shown on the left in pink and Kir7.1-R162W is displayed on the right in blue. **C.** Graph representation of HOLE2 profiles of the apo and Kir7.1-R162W models. The selectivity filter, helix bundle crossing, and G-loop gate are labelled. The pore radius is labelled across the x-axis and a green dashed line at 3 Å represents the lower limit for hydrated potassium ion radius.

6.6 Comparing the degree of constriction in each structure

To investigate the three different structures, apo Kir7.1, Kir7.1-PIP_2 and Kir7.1-R162W, the portion of the channel deemed too constricted to allow the conduction of hydrated potassium was evaluated (**Fig. 6.9**). The selectivity filter was not included in this analysis as this will always be narrower than a hydrated potassium ion. The model with the lowest percentage of constriction was Kir7.1-PIP_2 at 5 % suggesting it may be the most capable of ion conduction. Apo Kir7.1 has a higher degree of constriction at 14 % and Kir7.1-R162W has the most amount of pore constriction at 24 % of the channel being narrower than 6 Å in diameter.

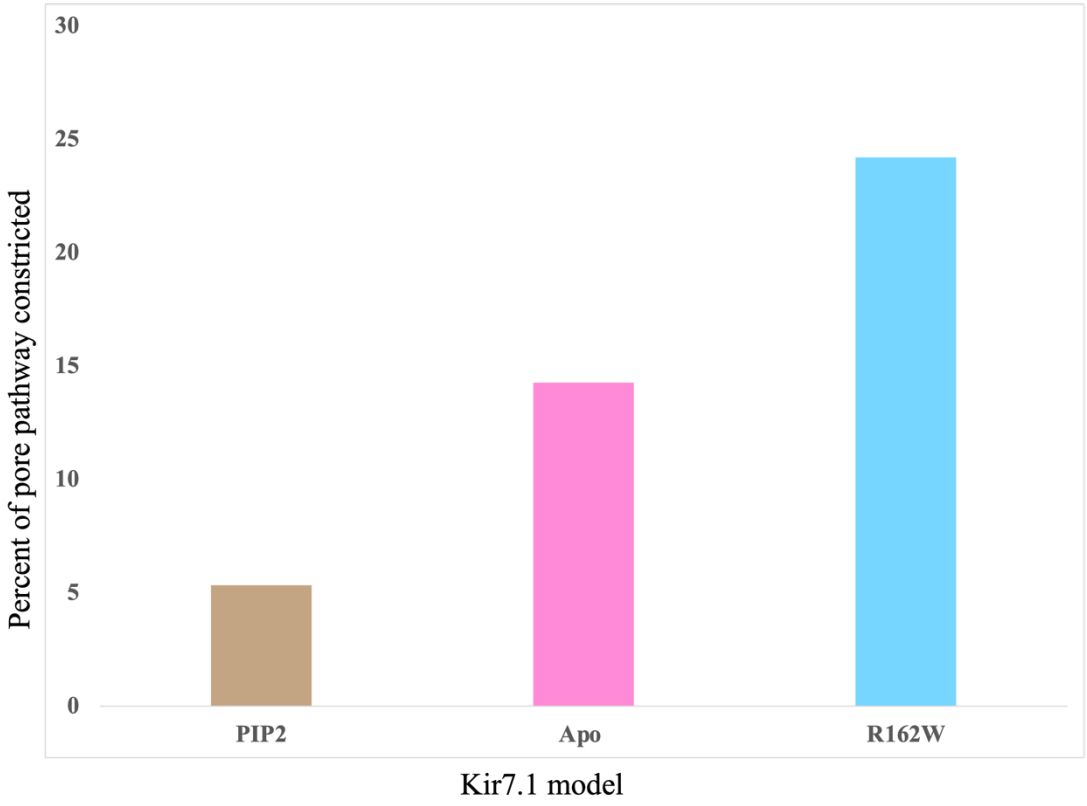

Figure 6.9. Comparison of the degree of constriction in each Kir7.1 structure. Graph representing the percentage of the pore in each model that is too constricted to allow potassium conduction, excluding the selectivity filter. The y-axis is the percentage of the channel pore. The Kir7.1 model is labelled below with Kir7.1-PIP_2 in tan, apo Kir7.1 in pink and Kir7.1-R162W in blue.

6.7 Thermal unfolding of Kir7.1-R162W

Section 5.5.3 outlined nanoDSF analysis of apo Kir7.1 and Kir7.1-PIP_2 to investigate the Tm shift induced by PIP_2 binding. Kir7.1-R162W was subjected to this analysis to compare any differences in thermal stability caused by the R162W mutation. The thermal stability of Kir7.1-R162W is comparable to that of WT Kir7.1 (**Fig. 6.10**). The addition of 0.1 mM C8-PIP_2 to each protein sample revealed that WT Kir7.1 displayed a more pronounced increase in Tm compared to Kir7.1-R162W. Specifically, WT Kir7.1 exhibited a Tm shift of 2.1 °C, while Kir7.1-R162W showed a shift of 1.2 °C (**Fig. 6.10**). Although the shift in Tm was smaller for Kir7.1-R162W, it still demonstrated enhanced stability in the presence of PIP_2, suggesting a potential interaction between the mutant protein and PIP_2.

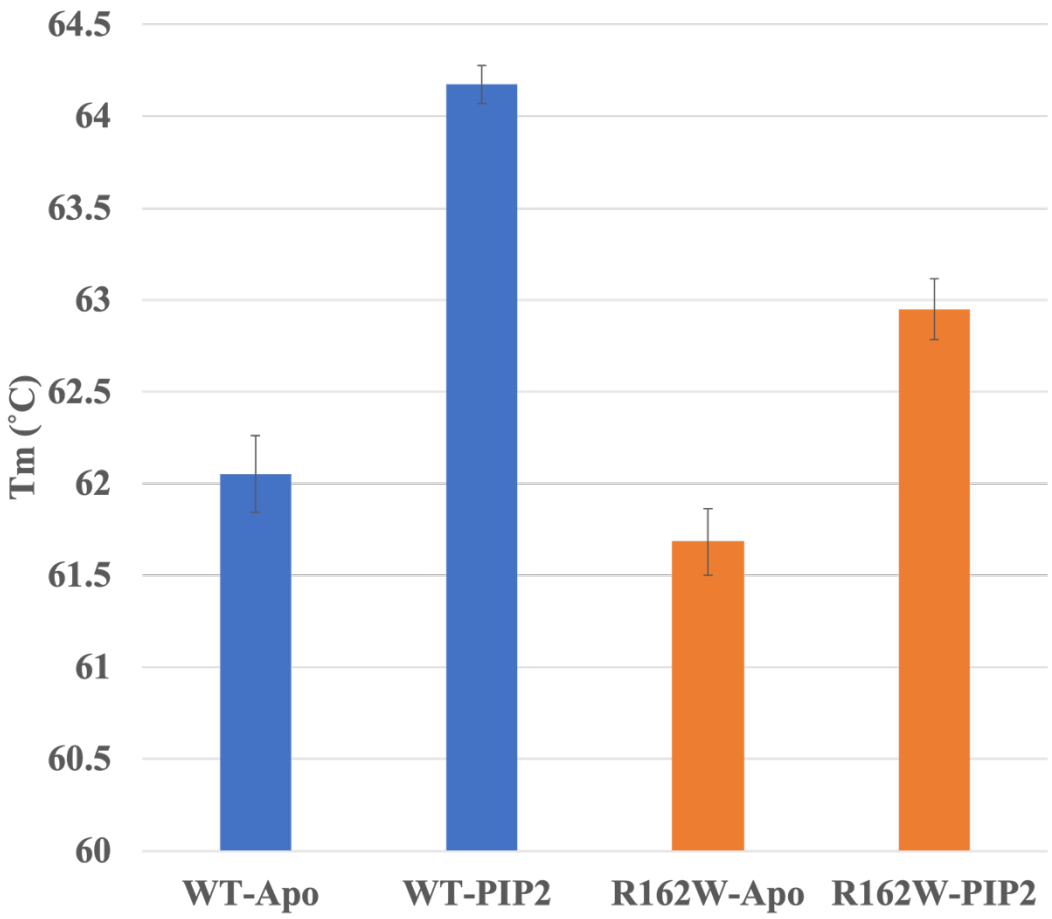

Figure 6.10. Thermal unfolding of apo Kir7.1 and Kir7.1-R162W with and without PIP_2. WT protein was analysed with and without PIP_2 present (blue). Kir7.1-R162W mutant was tested with and without the addition of PIP_2 (orange).

Each sample was tested a minimum of two independent times with error bars shown. The Tm is labelled on the y-axis.

6.8 Summary

Overall, this chapter outlined the cryo-EM analysis and characterisation of the disease-associated variant Kir7.1-R162W. A final EM map of 3.5 Å resolution was produced enabling the construction of the protein model. The Kir7.1-R162W model facilitated the investigation of residue 162 and the comparison between the apo and mutant structures. This revealed a novel constriction site at the tryptophan mutation, introducing a hydrophobic narrow region. A comparison of all three novel structures provided a comprehensive view of the channel pore constriction, shedding light on the impact of PIP_2 binding and the R162W mutation on the behaviour of the channel pore.

Chapter 7

7. Discussion and future work

7.1 Summary

Kir7.1 is a novel inward rectifying potassium channel implicated in many important processes in the human body, including the maintenance of photoreceptor cells and the onset of labour. Functional analysis has suggested the need for PIP_2 interaction with the protein for an open channel and ion conduction (Rohács et al., 2003). Several mutations in Kir7.1 have been identified in patients with SVD or LCA, two rare retinal diseases. These mutations have been linked to a loss of potassium conduction by Kir7.1 in the retinal pigment epithelium. An arginine-to-tryptophan mutation lying within the TMD-CTD linker (R162W) has been shown to be the sole mutation responsible for SVD. This position in the channel is thought to be responsible for PIP_2 binding and residues within the binding site are conserved amongst Kir channels.

The medium-high resolution structures presented in **Chapter 5** shed light on the effect of PIP_2 binding to Kir7.1 suggesting a potential mechanism of channel opening. Integrating these findings with the structural analysis of the Kir7.1-R162W mutant enhances our comprehensive understanding of Kir7.1's function and the underlying molecular mechanism of SVD.

7.2 Producing tetrameric folded Kir7.1 protein

7.2.1 WT and chimeric Kir7.1 were unsuccessfully expressed in *E. coli*

All constructs generated for expression in *E. coli* failed to produce sufficient quantities of tetrameric protein. This is likely due to human membrane proteins being notoriously difficult to express in sufficient quantities for functional and structural studies (Schlegel et al., 2014). There is a collection of other Kir channels that have been successfully expressed for structural studies using yeast and HEK cell expression systems (Hansen et al., 2011; Niu et al., 2020; Zhao and MacKinnon, 2021). However, there are no full-length human Kir channels shown to be capable of expression in *E. coli* for structural analysis. The only channel that successfully utilised *E. coli* as an expression system was the Kir3.1-bacterial chimera, which the chimera in this study was based on (Nishida et al., 2007). Although our efforts resulted in partial expression of particular chimeric constructs (**Fig. 4.3 and 4.4**), a more thorough optimisation process would be necessary to generate a sufficient quantity of protein samples suitable for structural analysis. This could involve refining the precise placement of the junction between human and bacterial proteins or implementing additional truncations to the N and C termini to enhance expression.

Given the notably more efficient expression of full-length human Kir7.1 in HEK293 cells, there was no need to pursue the optimisation of chimera expression levels in either *E. coli* or mammalian cells (**Fig. 4.5**). The utilisation of a mammalian expression system was expected to result in higher quantities of the human protein, given their capability to facilitate appropriate folding and post-translational modifications (Khan, 2013).

7.2.2 The optimisation of purification implies the occurrence of GFP dimerisation

SEC analysis revealed a chromatogram exhibiting two elution peaks, both containing Kir7.1 protein (**Fig. 4.13**). Through optimisation, the removal of the GFP tag from the C-terminus of Kir7.1 monomers led to a shift of the first elution peak to the second main tetrameric elution peak (**Fig. 4.14**). This indicates the possibility that the GFP located on the C-terminus of one tetramer might have been interacting with

the GFP tag on another tetramer, leading to the formation of larger complexes. This observation is also consistent with the NS-EM images for each peak, revealing larger particles in peak 1 compared to peak 2 (**Fig. 4.10**). Despite TEV cleavage of the GFP tag, a portion of the first peak persisted, even with increased cleavage time and TEV concentration. This persistence might stem from the tetramers' orientation while in the dimerised configuration, potentially obstructing access to the TEV cleavage site. In the future, it might prove beneficial to create a construct lacking the GFP tag in order to mitigate the initial dimerisation issue. However, it's important to note that GFP fusion tags commonly enhance protein stability and expression, warranting a thorough evaluation (Ki and Pack, 2020). For the aim of structural studies, we were able to generate a sufficient amount of GFP-cleaved, tetrameric, purified, folded Kir7.1.

7.3 The structure of Kir7.1 unveils novel features

Preliminary cryo-EM experiments failed to produce data sufficient for generating high-resolution 3D reconstructions (**Section 5.1**). This outcome is attributed in part to the presence of the graphene oxide support on the EM grids, which reduced overall contrast. Additionally, the sample required additional biochemical optimisation, detailed in **Section 4.4.5**, involving the removal of the C-terminal GFP tag to enhance the quality of the purified sample. Cryo-EM supports were also screened to determine optimal protein concentration, grid type and blotting duration (**Section 5.3**).

This is the first time the structure of Kir7.1 has been resolved. Upon comparison with its closest structurally documented relative, Kir2.2 (PDB: 3JYC), the overall typical Kir structural elements are present (**Fig. 5.6**). However, the most notable difference is the orientation of the CTD in relation to the TMD. When both structures are aligned by the TMD region, each CTD lies in a different orientation, with residue I170 in Kir7.1 lying 12 Å anticlockwise compared to L194 in Kir2.2. The implications of these dissimilar orientations remain unclear, although they could bear significance for the CTD's docking upon PIP_2 binding, an event not observed in Kir7.1.

Moreover, the G-loop region in Kir7.1 does not exhibit a constriction point in any of the cryo-EM structures (**Fig. 5.14**). Previous investigations involving GIRK2 and the Kir3.1 chimera have illuminated the role of G-loop gating influenced by PIP_2 binding (Bernsteiner et al., 2019; Li et al., 2019; Meng et al., 2012). Furthermore, the structure of Kir2.1 (PDB: 7ZDZ) showcased narrowed regions at the G-loop gate, impeding ion conduction (Fernandes et al., 2023). Kir7.1 lacks this constriction at the G-loop gate whether PIP_2 was bound to the protein or not. This raises additional inquiries regarding the G-loop's function in Kir channel gating and the possibility of subtype specificity.

7.4 Molecular mechanism of PIP_2 binding to Kir7.1

7.4.1 Absence of CTD docking to TMD

Prior structural investigations conducted on Kir2.2, Kir3.2, Kir3.4, and Kir6.2 have consistently revealed CTD docking to the TMD upon PIP_2 binding (**Section 1.3.1**) (Hansen et al., 2011; Martin et al., 2017; Niu et al., 2020). In our study with purified Kir7.1 supplemented with 1mM C8-PIP_2, no CTD docking was detected. Understanding the implications of this absence of CTD docking is challenging. It could result from sample preparation artefacts. The chosen detergent, GDN, might hinder the CTD from assuming the fully docked position. Notably, previous docked structures were achieved using DM or DDM as the purifying detergent (Hansen et al., 2011; Niu et al., 2020). Future work would involve screening alternative detergents and conducting nanodisc reconstitution of the protein to confirm that CTD docking does not occur in Kir7.1 under any sample conditions.

The final Kir7.1-PIP_2 EM map revealed unmodeled density within the PIP_2 binding site, suggesting the presence of PIP_2 in complex with Kir7.1. (**Fig. 5.9**). Placing PIP_2 into this density showed its interactions with Kir7.1. In **Fig. 5.9**, it is evident that PIP_2 engages with specific residues within Kir7.1's M1 and slide helix regions. Specifically, arginine 54, a residue highly conserved across Kir channels, forms a hydrogen bond with the 4' phosphate group (**Fig. 5.9D**). This position in Kir7.1 is a region where PIP_2 has been observed to bind in other Kir channels (Hansen et al., 2011; Niu et al., 2020). Additionally, other residues in Kir7.1 situated within 5 Å of PIP_2 include W53, W55, and R195 from one subunit, and D43 from a neighbouring

subunit (**Fig. 5.9B**). Residues W53, R195, and D43 are conserved among Kir channels and likely play a role in PIP_2 binding and channel activation. Notably, while all other Kir channels possess an arginine at position 39, Kir7.1 possesses an alanine (**Fig. 5.9D**). In Kir2.2, this arginine interacts with a leucine residue in the cytoplasmic domain, stabilising the CTD-docked conformation.

Analysis of Kir3.2 (PDB: 6XIT) reveals that arginine 77, corresponding to alanine 39 in Kir7.1, interacts with two residues in the CTD when PIP_2 is bound. In Kir3.2, the binding of PIP_2 prompts a docked conformation in each subunit (Niu et al., 2020). Arginine 77 forms interactions with glutamic acid 203 and leucine 229 in the CTD, stabilising this docked state. In the case of Kir7.1, the absence of the arginine residue in the slide helix could account for the lack of CTD docking.

7.4.2 Is the helix bundle crossing a gating mechanism in Kir7.1?

Despite the absence of CTD docking, a discernible widening of the HBC was observed. This is potentially a conformational change induced by PIP_2 binding to Kir7.1. The HBC in Kir7.1 is primarily defined by two key residues, T153 and V157 (**Fig. 5.11**), which are positioned closely enough in the apo Kir7.1 model to induce a constriction, narrowing the pore to a diameter of 3.3 Å (**Fig. 5.14**). The average diameter of a hydrated potassium ion is approximately 6.6 Å, with variations ranging from 6 to 8 Å. Comparatively, in the Kir7.1-PIP_2 model the HBC expands, with the most constricted point having a diameter of 4.8 Å.

Gating at the HBC has been discussed with various Kir channels showing that the movement of M2 helices contributes to pore widening. However, does this movement constitute an action to open the channel? Investigations into Kir6.2 channels found that access to the M2 helices was slower when the channel was in a closed state. This suggests that when the channel is closed the M2 helices prevent or slow access to the channel pore and therefore may contribute to channel gating (Phillips et al., 2003). As outlined in **Section 1.3.2**, the conserved glycine in the M2 helix is known to play a role in the hinging and splaying of the helices (Grottesi et al., 2005). Furthermore, introducing a kink into the M2 helices of the Kir3 chimera through a proline mutation, stabilised the channel's open state (Meng et al., 2016).

The introduction of this kink confirmed that the widening of the M2 helices contributed to channel activity. Our observation of the HBC widening in Kir7.1 upon PIP_2 binding strengthens the argument for the role of the HBC in Kir channel gating.

However, even upon PIP_2 binding and HBC widening, the Kir7.1-PIP_2 model possesses a channel pore too narrow for hydrated potassium conduction (**Fig. 5.14**). MD and crosslinking investigations focussed on Kirbac3.1 unveiled that the widening of the HBC is not imperative for successful K^+ conductance. This study showed that potassium traverses the HBC constriction via partial dehydration, a process offset by the tyrosine collar within the inner M2 helices of Kirbac3.1(Black et al., 2020). However, Kir7.1 does not possess a tyrosine collar, instead threonine 153 lies at this point. Threonine may locally substitute for a portion of the hydration shell of the potassium ion overcoming the narrowing of the pore. This concept has been proposed before about threonine residues at the constriction point in the nicotinic acetylcholine receptor (Villarroel et al., 1991). Alternatively, the channel may exist with a wider pore conformation physiologically, but this diameter may represent the lowest energy state of the purified protein in a detergent micelle (Zubcevic et al., 2014). Therefore, further experiments on human Kir7.1 would need to be conducted to investigate if HBC widening is playing a role in channel activation.

However, a comparison of the apo Kir7.1 and the Kir7.1-PIP_2 model confidently demonstrates a difference in the orientation of the HBC. The sole distinction between these models is the addition of C8-PIP_2, implying that the binding of PIP_2 is responsible for the dilated pore size. However, the extent to which this movement contributes to channel activation requires further investigation.

7.5 Disease-associated mutations in Kir7.1

7.5.1 R162W and snowflake vitreoretinal degeneration

Kir7.1 is highly expressed in the RPE, localising predominantly to the apical surface (**Fig. 1.6**). This localisation accounts for the substantial K^+ conductance of the apical membrane. Kir7.1 plays a crucial role in K^+ secretion into the subretinal space, maintaining Na^+/K^+ pump activity, buffering light-induced K^+ concentration changes, and regulating transepithelial K^+ transport (Gallemore et al., 1997). A mutation in *KCNJ13*, the gene encoding Kir7.1, is responsible for causing SVD. The arginine-to-tryptophan change in Kir7.1 at residue 162 results in a non-functional ion channel (Zhang et al., 2013). Previous researchers showed that the mutated protein retains successful expression, proper folding and trafficking to the plasma membrane (Pattnaik et al., 2013; Zhang et al., 2013). Our study supports this finding as Kir7.1-R162W was successfully purified from HEK293 cells producing a SEC chromatogram comparable to WT Kir7.1 (**Fig. 6.3**). We also determined the 3D structure of Kir7.1-R162W which provided the first insight into the molecular arrangement of the mutant protein.

The structure of Kir7.1-R162W confirmed that at least a portion of protein successfully formed folded tetramers. The process of cryo-EM sample preparation and image processing was effective, employing a similar approach as utilised for the WT protein (**Fig. 6.4**). The final model demonstrated a notable difference at the location of the R162W mutation. The EM map exhibited improved and more resolved density within the TMD-CTD linker, corresponding to the site of the mutation (**Fig. 6.5**). In the Kir7.1-R162W model, the tryptophan side chains are orientated inwards into the pore pathway (**Fig. 6.6B**). Whereas the arginine side chains in the WT protein point outwards away from the central pore (**Fig. 6.6C**). Analysing pore size using HOLE2 revealed that the R162W mutation introduced a novel constriction point in the protein, narrow enough to hinder the passage of a hydrated potassium ion (**Fig. 6.8**). This constriction, situated at residue 162 in Kir7.1-R162W, is characterised by hydrophobic tryptophan side chains, possessing a diameter of 2.6 Å. This results in a blockage within the channel pore, effectively hindering potassium conduction.

The established hypothesis regarding this mutation's implication in SVD was centred around its disruption of PIP_2 binding, ultimately failing to activate the channel

(Pattnaik et al., 2013; Zhang et al., 2013). However, our experiments present a novel mechanism illustrating how this mutation may impede ion conduction. Thermal unfolding analysis showed that Kir7.1-R162W presented a Tm shift when C8-PIP_2 was present in the sample, suggesting that PIP_2 may still bind to Kir7.1-R162W. From our analysis of PIP_2 binding to WT Kir7.1 (**Section 5.5.2**), it's likely that PIP_2 could still interact with the Kir7.1-R162W protein as the key residues remain unchanged. However, even if the HBC were to widen, mimicking the Kir7.1-PIP_2 model, the tryptophan side chains would still produce a narrow constriction point, impeding ion passage.

Vera et al. (2021) examined the impact of various mutations at residue 162 in Kir7.1 and demonstrated that the elimination of a positive charge at this position did not hinder channel activity. This contradicts the previous hypothesis that the R162W mutation exerts its negative effect by disrupting PIP_2 binding through the removal of the native arginine and its positive side chain. The study demonstrated that mutations to neutral residues with smaller side chains did not adversely affect channel activity. Conversely, mutations involving residues with bulkier side chains, whether neutral or positively charged, resulted in a negative impact on Kir7.1 channel activity (Vera et al., 2021). This research complements our structural analysis that shows that the R162W mutant exerts its negative impact by forming a new constriction in the channel pore.

7.5.2 Proposing implications of LCA disease mutations

The three Kir7.1 models allow us to gain insight into the protein and interpret the implications of other disease-associated mutations. LCA has been associated with several mutations within Kir7.1 that are thought to produce a non-functional channel.

7.5.2.1 Impact of early stop codon mutations

Preliminary characterisation of the disease variants indicated that Kir7.1-R166* and Kir7.1-Q219* failed to exhibit expression (**Fig. 6.2**). Both of these disease mutants introduce early stop codons into the protein sequence. Kir7.1-R166* would result in a protein lacking the entire CTD, while Kir7.1-Q219* would lack the subsequent 131 amino acids. Premature stop codons can yield various detrimental effects on protein production. Generating a truncated protein version is likely to yield a non-functional protein lacking crucial functional domains. Q219 forms interactions with L241 in the neighbouring subunit stabilising the tetrameric complex. However, in this scenario, it is possible that nonsense-mediated mRNA decay (NMD) is at play. In this mechanism, mRNAs containing premature stop codons are degraded, leading to a lack of protein expression. The absence of protein expression in both soluble and insoluble fractions suggests that the protein was either not expressed due to NMD or the truncated protein underwent degradation within the cell.

7.5.2.2 S105I and I120T fail to produce folded purified protein

Kir7.1-S105I and Kir7.1-I120T exhibited some level of expression, albeit not to the extent seen in the WT protein. Kir7.1-S105I showed a small amount of protein in the cell lysate, but none was detectable in the purified protein sample (**Fig. 6.2**). This suggests the S105I mutant may be unstable and degraded throughout the purification process. Drawing a definitive conclusion regarding the mechanism through which this mutation exerts its negative impact is challenging. Given the location of residue 105 at the start of the extracellular turret, a mutation here could disrupt its structural arrangement.

Comparably, I120T displayed detectable expression in the soluble cell lysate (**Fig. 6.2B**), however, when the purified protein sample was analysed only a small amount of Kir7.1-I120T was evident. Residue I120T lies within the selectivity filter of Kir7.1 and this mutation may have impacted channel stability, folding and/or

assembly of the channel. However, the cell lysate WB analysis shows banding of higher oligomeric weights implying potential dimer, trimer, and tetramer formation (**Fig. 6.2B**). This suggests that the issue is likely protein stability, warranting further exploration to enhance protein yield.

7.5.2.3 L241P

Conversely, Kir7.1-L241P appeared to be expressed and purified in sufficient quantities (**Fig. 6.2**). Notably, the structural examination of leucine 241 revealed that its side chain establishes interactions with leucine 226 from the same chain and glutamine 219 from an adjacent subunit. This observation implies that residue 241 contributes to the establishment of a stable tetramer structure. By introducing a proline mutation at this position in the apo Kir7.1 model, these critical interactions are disrupted. Prior research has indicated that the L241P mutation in Kir7.1 results in the prevention of channel glycosylation, a process previously found to be essential for channel function (Carrington et al., 2018). This alteration in glycosylation may be linked to the loss of channel activity attributed to this mutation. The precise manner in which this CTD mutation impacts extracellular turret glycosylation remains unclear from structural analysis alone. Further structural investigations of this mutant variant hold the potential to provide deeper insights into this manner.

7.5.2.4 T153I

Finally, the Kir7.1-T153I variant possesses a mutation within the HBC region. This protein mutant fails to conduct ions, however, it has been shown to successfully localise to the membrane (Beverley et al., 2022). Our experiments confirmed the expression and purification of Kir7.1-T153I in its tetrameric form (**Fig. 6.3**). The functional implications of this mutation were investigated by Beverley et al. (2022) and their findings revealed that the residue at position 153 must possess polar side chains but cannot be small or too large. Small side chains, such as glycine and alanine, resulted in non-functional Kir channels. The T153I mutant introduces an isoleucine residue that would narrow the pore and establish a hydrophobic environment, which could contribute to the channel's dysfunction. Our analysis, centred on PIP_2-induced HBC widening, proposes a role for threonine 153 as the most constricted point in the channel's pathway (**Section 5.5.2**). Thus, mutations

affecting this residue may influence HBC widening and subsequently impact channel conduction.

In conclusion, the experiments in this study require repeating to validate the expression levels of each disease variant. The proteins showing successful expression in folded tetrameric forms merit further investigation through additional biophysical and structural analyses. This research could provide deeper insights into the implications and mechanisms associated with these disease variants.

7.6 Future work and conclusions

Our research provides the first insight into the structure of Kir7.1 and the molecular basis of the R162W mutation linked to SVD. Previous studies have linked Kir7.1 to retinal function, particularly in the retinal pigment epithelium, and SVD has been associated with a loss of Kir7.1 activity. Our work unveils that this loss of function arises from a newly introduced channel pore constriction at residue 162. Future work would be necessary to confirm this finding. Conducting cryo-EM structural analysis of Kir7.1-R162W in the presence of PIP_2 would offer valuable insights into whether PIP_2 indeed binds to the mutant channel and if any alterations in the positioning of tryptophan 162 side chains can be observed. Structural analysis of this interaction would highlight any impact of PIP_2 binding to the mutant protein and conclude if the constriction point remains even after channel activation. By demonstrating the presence of this constriction point after channel activation, a more comprehensive understanding of the molecular basis of the R162W mutation's impact on Kir7.1 function would be achieved. Such conclusive findings would not only expand our knowledge of SVD pathogenesis but also aid the development of targeted therapeutic strategies to address this mutation.

Furthermore, the models of Kir7.1 in the apo form and the PIP_2-bound state provide a proposed mechanism of channel activation. We demonstrated that upon PIP_2 binding Kir7.1 fails to show CTD docking, which was thought to be needed for channel opening. However, we demonstrated that the HBC is widened upon PIP_2 binding even without CTD docking and this may be sufficient for at least partially activating the channel. Future experiments would begin with structural analysis of Kir7.1-PIP_2 in different sample detergents, such as DDM and nanodiscs, in order to investigate if the lack of CTD docking is a result of sample preparation. Furthermore, the availability of Kir7.1 structural models opens up the possibility of employing molecular dynamics simulations to gain deeper insights into the impact of PIP_2 binding. Through these simulations, we could explore how PIP_2 interaction influences the widening of the HBC and whether this structural alteration allows for the passage of potassium ions. By investigating the dynamic behaviour of the channel under different conditions and in the presence of PIP_2, we can refine our understanding of the functional consequences of these structural changes. This could

also be applied to the Kir7.1-R162W model to evaluate if PIP_2 induces any conformational changes to the mutant under simulation conditions. Additionally, performing mutagenesis experiments on Kir7.1, where an arginine mutation is introduced at position 39 to align it with other Kir channels, could offer insights into the role of this residue in CTD docking and this might provide an explanation for the absence of this interaction in Kir7.1.

We have successfully established a comprehensive workflow for the expression, purification, and structural analysis of Kir7.1, laying the foundation for in-depth exploration of Kir7.1 disease mutations. By cloning the disease-associated variants linked to LCA, our next steps could involve extensive characterisation through expression trials, assessment of protein folding, and tetramer formation, followed by cryo-EM experiments. While we have suggested potential consequences of these mutations, conducting further experimental investigations is crucial to advancing our understanding of LCA and its underlying mechanisms.

Our study offers the first structure of human Kir7.1. We generated three models that highlight the effect of PIP_2 binding and reveal channel pore constriction in the Kir7.1-R162W mutant linked to SVD. These findings make a significant contribution to Kir channel research, shedding light on Kir7.1's role in SVD and LCA. Our hope is that this thesis work will propel further research in the Kir7.1-SVD domain, ultimately advancing therapeutic development efforts.

Bibliography

Ambrosini, E., Sicca, F., Brignone, M.S., D'Adamo, M.C., Napolitano, C., Servettini, I., Moro, F., Ruan, Y., Guglielmi, L., Pieroni, S., Servillo, G., Lanciotti, A., Valvo, G., Catacuzzeno, L., Franciolini, F., Molinari, P., Marchese, M., Grottesi, A., Guerrini, R., Santorelli, F.M., Priori, S., Pessia, M., 2014. Genetically induced dysfunctions of Kir2.1 channels: implications for short QT3 syndrome and autism-epilepsy phenotype. Human Molecular Genetics 23, 4875–4886.

Anderson, E.J.P., Ghamari-Langroudi, M., Cakir, I., Litt, M.J., Chen, V., Reggiardo, R.E., Millhauser, G.L., Cone, R.D., 2019. Late onset obesity in mice with targeted deletion of potassium inward rectifier Kir7.1 from cells expressing the melanocortin-4 receptor. Journal of Neuroendocrinology 31, e12670.

Bai, X., McMullan, G., Scheres, S.H.W., 2015. How cryo-EM is revolutionizing structural biology. Trends in Biochemical Sciences 40, 49–57.

Baker, L.A., Rubinstein, J.L., 2010. Radiation damage in electron cryomicroscopy. Methods in Enzymology 481, 371–388.

Balthasar, N., Dalgaard, L.T., Lee, C.E., Yu, J., Funahashi, H., Williams, T., Ferreira, M., Tang, V., McGovern, R.A., Kenny, C.D., Christiansen, L.M., Edelstein, E., Choi, B., Boss, O., Aschkenasi, C., Zhang, C., Mountjoy, K., Kishi, T., Elmquist, J.K., Lowell, B.B., 2005. Divergence of melanocortin pathways in the control of food intake and energy expenditure. Cell 123, 493–505.

Bavro, V.N., De Zorzi, R., Schmidt, M.R., Muniz, J.R.C., Zubcevic, L., Sansom, M.S.P., Vénien-Bryan, C., Tucker, S.J., 2012. Structure of a KirBac potassium channel with an open bundle crossing indicates a mechanism of channel gating. Nature Structural & Molecular Biology 19, 158–163.

Bernsteiner, H., Zangerl-Plessl, E.-M., Chen, X., Stary-Weinzinger, A., 2019. Conduction through a narrow inward-rectifier K(+) channel pore. The Journal of General Physiology 151, 1231–1246.

Beverley, K.M., Shahi, P.K., Kabra, M., Zhao, Q., Heyrman, J., Steffen, J., Pattnaik, B.R., 2022. Kir7.1 disease mutant T153I within the inner pore affects K(+) conduction. American Journal of Physiology. Cell Physiology 323, C56–C68.

Black, K.A., He, S., Jin, R., Miller, D.M., Bolla, J.R., Clarke, O.B., Johnson, P.,

Windley, M., Burns, C.J., Hill, A.P., Laver, D., Robinson, C. V, Smith, B.J., Gulbis, J.M., 2020. A constricted opening in Kir channels does not impede potassium conduction. Nature Communications 11, 3024.

Bockenhauer, D., Feather, S., Stanescu, H.C., Bandulik, S., Zdebik, A.A., Reichold, M., Tobin, J., Lieberer, E., Sterner, C., Landoure, G., Arora, R., Sirimanna, T., Thompson, D., Cross, J.H., van't Hoff, W., Al Masri, O., Tullus, K., Yeung, S., Anikster, Y., Klootwijk, E., Hubank, M., Dillon, M.J., Heitzmann, D., Arcos-Burgos, M., Knepper, M.A., Dobbie, A., Gahl, W.A., Warth, R., Sheridan, E., Kleta, R., 2009. Epilepsy, ataxia, sensorineural deafness, tubulopathy, and KCNJ10 mutations. The New England Journal of Medicine 360, 1960–1970.

Campbell, M.G., Cheng, A., Brilot, A.F., Moeller, A., Lyumkis, D., Veesler, D., Pan, J., Harrison, S.C., Potter, C.S., Carragher, B., Grigorieff, N., 2012. Movies of ice-embedded particles enhance resolution in electron cryo-microscopy. Structure 20, 1823–1828.

Carrington, S.J., Hernandez, C.C., Swale, D.R., Aluko, O.A., Denton, J.S., Cone, R.D., 2018. G protein–coupled receptors differentially regulate glycosylation and activity of the inwardly rectifying potassium channel Kir7.1. Journal of Biological Chemistry 293, 17739–17753.

Chen, J., Noble, A.J., Kang, J.Y., Darst, S.A., 2019. Eliminating effects of particle adsorption to the air/water interface in single-particle cryo-electron microscopy: Bacterial RNA polymerase and CHAPSO. Journal of Structural Biology: X 1, 100005.

Cheng, C.-J., Sung, C.-C., Huang, C.-L., Lin, S.-H., 2015. Inward-rectifying potassium channelopathies: new insights into disorders of sodium and potassium homeostasis. Pediatric Nephrology 30, 373–383.

Cheng, Y., Grigorieff, N., Penczek, P.A., Walz, T., 2015. A primer to single-particle cryo-electron microscopy. Cell 161, 438–449.

Churchward, M.A., Butt, R.H., Lang, J.C., Hsu, K.K., Coorssen, J.R., 2005. Enhanced detergent extraction for analysis of membrane proteomes by two-dimensional gel electrophoresis. Proteome Science 3, 5.

Cornejo, I., Villanueva, S., Burgos, J., López-Cayuqueo, K.I., Chambrey, R., Julio-Kalajzić, F., Buelvas, N., Niemeyer, M.I., Figueiras-Fierro, D., Brown, P.D., Sepúlveda, F. V, Cid, L.P., 2018. Tissue distribution of Kir7.1 inwardly rectifying K^+ channel probed in a knock-in mouse expressing a haemagglutinin-

tagged protein. Frontiers in Physiology 9, 428.

Croll, T.I., 2018. ISOLDE: A physically realistic environment for model building into low-resolution electron-density maps. Acta Crystallographica Section D: Structural Biology 74, 519–530.

de Boer, T.P., Houtman, M.J.C., Compier, M., van der Heyden, M.A.G., 2010. The mammalian K(IR)2.x inward rectifier ion channel family: expression pattern and pathophysiology. Acta Physiologica (Oxford, England) 199, 243–256.

den Hollander, A.I., Roepman, R., Koenekoop, R.K., Cremers, F.P.M., 2008. Leber congenital amaurosis: genes, proteins and disease mechanisms. Progress in Retinal and Eye Research 27, 391–419.

Döring, F., Derst, C., Wischmeyer, E., Karschin, C., Schneggenburger, R., Daut, J., Karschin, A., 1998. The epithelial inward rectifier channel Kir7.1 displays unusual K+ permeation properties. The Journal of Neuroscience 18, 8625–8636.

Dornonville de la Cour, M., 1993. Ion transport in the retinal pigment epithelium. A study with double barrelled ion-selective microelectrodes. Acta Ophthalmologica. Supplement 1–32.

Doupnik, C.A., Davidson, N., Lester, H.A., 1995. The inward rectifier potassium channel family. Current Opinion in Neurobiology 5, 268–277.

Doyle, D.A., Cabral, J.M., Pfuetzner, R.A., Kuo, A., Gulbis, J.M., Cohen, S.L., Chait, B.T., MacKinnon, R., 1998. The structure of the potassium channel: molecular basis of K+ conduction and selectivity. Science 280, 69 LP – 77.

Dubochet, J., Adrian, M., Chang, J.J., Homo, J.C., Lepault, J., McDowall, A.W., Schultz, P., 1988. Cryo-electron microscopy of vitrified specimens. Quarterly Reviews of Biophysics 21, 129–228.

Emsley, P., Lohkamp, B., Scott, W.G., Cowtan, K., 2010. Features and development of Coot. Acta Crystallographica. Section D, Biological Crystallography 66, 486–501.

Esmaeili, Y., Bidram, E., Zarrabi, A., Amini, A., Cheng, C., 2020. Graphene oxide and its derivatives as promising In-vitro bio-imaging platforms. Scientific Reports 10, 18052.

Evans, R., O'Neill, M., Pritzel, A., Antropova, N., Senior, A., Green, T., Žídek, A., Bates, R., Blackwell, S., Yim, J., Ronneberger, O., Bodenstein, S., Zielinski, M., Bridgland, A., Potapenko, A., Cowie, A., Tunyasuvunakool, K., Jain, R., Clancy, E., Kohli, P., Jumper, J., Hassabis, D., 2021. Protein complex

prediction with AlphaFold-Multimer. bioRxiv 2021.10.04.463034.

Evans, R., O'Neill, M., Pritzel, A., Antropova, N., Senior, A., Green, T., Žídek, A., Bates, R., Blackwell, S., Yim, J., Ronneberger, O., Bodenstein, S., Zielinski, M., Bridgland, A., Potapenko, A., Cowie, A., Tunyasuvunakool, K., Jain, R., Clancy, E., Kohli, P., Jumper, J., Hassabis, D., 2022. Protein complex prediction with AlphaFold-Multimer. bioRxiv 2021.10.04.463034.

Fazzi, E., Signorini, S.G., Scelsa, B., Bova, S.M., Lanzi, G., 2003. Leber's congenital amaurosis: an update. European Journal of Paediatric Neurology 7, 13–22.

Fernandes, C.A.H., Zuniga, D., Fagnen, C., Kugler, V., Scala, R., Péhau-Arnaudet, G., Wagner, R., Perahia, D., Bendahhou, S., Vénien-Bryan, C., 2023. Cryo–electron microscopy unveils unique structural features of the human Kir2.1 channel. Science Advances 8, eabq8489.

Gallemore, R.P., Hughes, B.A., Miller, S.S., 1997. Retinal pigment epithelial transport mechanisms and their contributions to the electroretinogram. Progress in Retinal and Eye Research 16, 509–566.

Gasteiger, E., Gattiker, A., Hoogland, C., Ivanyi, I., Appel, R.D., Bairoch, A., 2003. ExPASy: The proteomics server for in-depth protein knowledge and analysis. Nucleic Acids Research 31, 3784–3788.

Ghamari-Langroudi, M., Digby, G.J., Sebag, J.A., Millhauser, G.L., Palomino, R., Matthews, R., Gillyard, T., Panaro, B.L., Tough, I.R., Cox, H.M., 2015. G-protein-independent coupling of MC4R to Kir7. 1 in hypothalamic neurons. Nature 520, 94–98.

Glaeser, R.M., 2019. How good can single-particle cryo-EM become? What remains before it approaches its physical limits? Annual Review of Biophysics 48, 45–61.

Goldmann, T., Overlack, N., Möller, F., Belakhov, V., van Wyk, M., Baasov, T., Wolfrum, U., Nagel-Wolfrum, K., 2012. A comparative evaluation of NB30, NB54 and PTC124 in translational read-through efficacy for treatment of an USH1C nonsense mutation. EMBO Molecular Medicine 4, 1186–1199.

Goldmann, T., Overlack, N., Wolfrum, U., Nagel-Wolfrum, K., 2011. PTC124-mediated translational readthrough of a nonsense mutation causing Usher syndrome type 1C. Human Gene Therapy 22, 537–547.

Grigorieff, N., 2007. FREALIGN: high-resolution refinement of single particle

structures. Journal of Structural Biology 157, 117–125.

Grottesi, A., Domene, C., Hall, B., Sansom, M.S.P., 2005. Conformational dynamics of M2 helices in KirBac channels: helix flexibility in relation to gating via molecular dynamics simulations. Biochemistry 44, 14586–14594.

Hager, N.A., McAtee, C.K., Lesko, M.A., O'Donnell, A.F., 2022. Inwardly rectifying potassium channel Kir2.1 and its "Kir-ious" regulation by protein trafficking and roles in development and disease. Frontiers in Cell and Developmental Biology.

Halbach, P., Pillers, D.-A.M., York, N., Asuma, M.P., Chiu, M.A., Luo, W., Tokarz, S., Bird, I.M., Pattnaik, B.R., 2015. Oxytocin expression and function in the posterior retina: a novel signaling pathway. Investigative Ophthalmology & Visual Science 56, 751–760.

Hansen, S.B., Tao, X., MacKinnon, R., 2011. Structural basis of PIP2 activation of the classical inward rectifier K+ channel Kir2.2. Nature 477, 495–498.

Heinz, C., Niederweis, M., 2000. Selective extraction and purification of a mycobacterial outer membrane protein. Analytical Biochemistry 285, 113–120.

Hejtmancik, J.F., Jiao, X., Li, A., Sergeev, Y. V, Ding, X., Sharma, A.K., Chan, C.-C., Medina, I., Edwards, A.O., 2008. Mutations in KCNJ13 cause autosomal-dominant snowflake vitreoretinal degeneration. The American Journal of Human Genetics 82, 174–180.

Hille, B., 1992. Ionic channels of excitable membranes (second edition). FEBS Letters 306, 277–278.

Hirose, T., Lee, K.Y., Schepens, C.L., 1974. Snowflake degeneration in hereditary vitreoretinal degeneration. American Journal of Ophthalmology 77, 143–153.

Ho, K., Nichols, C.G., Lederer, W.J., Lytton, J., Vassilev, P.M., Kanazirska, M. V, Hebert, S.C., 1993. Cloning and expression of an inwardly rectifying ATP-regulated potassium channel. Nature 362, 31–38.

Hodgkin, A.L., Keynes, R.D., 1955. The potassium permeability of a giant nerve fibre. The Journal of Physiology 128, 61–88.

Humphrey, W., Dalke, A., Schulten, K., 1996. VMD: visual molecular dynamics. Journal of Molecular Graphics 14, 27-28,33-38.

Inagaki, N., Gonoi, T., Clement, J.P. 4th, Namba, N., Inazawa, J., Gonzalez, G., Aguilar-Bryan, L., Seino, S., Bryan, J., 1995. Reconstitution of IKATP: an inward rectifier subunit plus the sulfonylurea receptor. Science 270, 1166–1170.

Ishida, T., Kinoshita, K., 2007. PrDOS: prediction of disordered protein regions from amino acid sequence. Nucleic Acids Research 35, 460–464.

Jin, T., Peng, L., Mirshahi, T., Rohacs, T., Chan, K.W., Sanchez, R., Logothetis, D.E., 2002. The βγ subunits of G proteins gate a K+ channel by pivoted bending of a transmembrane segment. Molecular Cell 10, 469–481.

Jogini, V., Jensen, M.Ø., Shaw, D.E., 2022. Gating and modulation of an inward-rectifier potassium channel. Journal of General Physiology 155, e202213085.

Jumper, J., Evans, R., Pritzel, A., Green, T., Figurnov, M., Ronneberger, O., Tunyasuvunakool, K., Bates, R., Žídek, A., Potapenko, A., Bridgland, A., Meyer, C., Kohl, S.A.A., Ballard, A.J., Cowie, A., Romera-Paredes, B., Nikolov, S., Jain, R., Adler, J., Back, T., Petersen, S., Reiman, D., Clancy, E., Zielinski, M., Steinegger, M., Pacholska, M., Berghammer, T., Bodenstein, S., Silver, D., Vinyals, O., Senior, A.W., Kavukcuoglu, K., Kohli, P., Hassabis, D., 2021. Highly accurate protein structure prediction with AlphaFold. Nature 596, 583–589.

Kano, H., Toyama, Y., Imai, S., Iwahashi, Y., Mase, Y., Yokogawa, M., Osawa, M., Shimada, I., 2019. Structural mechanism underlying G protein family-specific regulation of G protein-gated inwardly rectifying potassium channel. Nature Communications 10, 2008.

Khan, A.O., Bergmann, C., Neuhaus, C., Bolz, H.J., 2015. A distinct vitreo-retinal dystrophy with early-onset cataract from recessive KCNJ13 mutations. Ophthalmic Genetics 36, 79–84.

Khan, K.H., 2013. Gene expression in mammalian cells and its applications. Advanced Pharmaceutical Bulletin 3, 257–263.

Ki, M.-R., Pack, S.P., 2020. Fusion tags to enhance heterologous protein expression. Applied Microbiology and Biotechnology 104, 2411–2425.

Kiarash Jamali, Dari Kimanius, S.H.S., 2023. A graph neural network approach to automated model building in cryo-EM maps. The Eleventh International Conference on Learning Representations.

Koster, J.C., Permutt, M.A., Nichols, C.G., 2005. Diabetes and insulin secretion: the ATP-sensitive K+ channel (K ATP) connection. Diabetes 54, 3065–3072.

Krapivinsky, G., Medina, I., Eng, L., Krapivinsky, L., Yang, Y., Clapham, D.E., 1998. A novel inward rectifier K+ channel with unique pore properties. Neuron 20, 995–1005.

Kumar, M., Pattnaik, B.R., 2014. Focus on Kir7.1: physiology and channelopathy. Channels 8, 488–495.

Kuo, A., Gulbis, J.M., Antcliff, J.F., Rahman, T., Lowe, E.D., Zimmer, J., Cuthbertson, J., Ashcroft, F.M., Ezaki, T., Doyle, D.A., 2003. Crystal structure of the potassium channel KirBac1.1 in the closed state. Science 300, 1922–1926.

la Cour, M., Lund-Andersen, H., Zeuthen, T., 1986. Potassium transport of the frog retinal pigment epithelium: autoregulation of potassium activity in the subretinal space. The Journal of Physiology 375, 461–479.

Leal-Pinto, E., Gómez-Llorente, Y., Sundaram, S., Tang, Q.-Y., Ivanova-Nikolova, T., Mahajan, R., Baki, L., Zhang, Z., Chavez, J., Ubarretxena-Belandia, I., Logothetis, D.E., 2010. Gating of a G protein-sensitive mammalian Kir3.1 prokaryotic Kir channel chimera in planar lipid bilayers. The Journal of Biological Chemistry 285, 39790–39800.

Leduc-Nadeau, A., Lussier, Y., Arthus, M.-F., Lonergan, M., Martinez-Aguayo, A., Riveira-Munoz, E., Devuyst, O., Bissonnette, P., Bichet, D.G., 2010. New autosomal recessive mutations in aquaporin-2 causing nephrogenic diabetes insipidus through deficient targeting display normal expression in Xenopus oocytes. The Journal of Physiology 588, 2205–2218.

Lee, M.M., Ritter, R., Hirose, T., Vu, C.D., Edwards, A.O., 2003. Snowflake vitreoretinal degeneration: follow-up of the original family. Ophthalmology 110, 2418–2426.

Lehner, I., Niehof, M., Borlak, J., 2003. An optimized method for the isolation and identification of membrane proteins. Electrophoresis 24, 1795–1808.

Li, D., Jin, T., Gazgalis, D., Cui, M., Logothetis, D.E., 2019. On the mechanism of GIRK2 channel gating by phosphatidylinositol bisphosphate, sodium, and the Gβγ dimer. The Journal of Biological Chemistry 294, 18934–18948.

Liebschner, D., Afonine, P. V, Baker, M.L., Bunkóczi, G., Chen, V.B., Croll, T.I., Hintze, B., Hung, L.W., Jain, S., McCoy, A.J., Moriarty, N.W., Oeffner, R.D., Poon, B.K., Prisant, M.G., Read, R.J., Richardson, J.S., Richardson, D.C., Sammito, M.D., Sobolev, O. V, Stockwell, D.H., Terwilliger, T.C., Urzhumtsev, A.G., Videau, L.L., Williams, C.J., Adams, P.D., 2019. Macromolecular structure determination using X-rays, neutrons and electrons: recent developments in Phenix. Acta Crystallographica. Section D, Structural

Biology 75, 861–877.

Liu, C., Dalby, B., Chen, W., Kilzer, J.M., Chiou, H.C., 2008. Transient transfection factors for high-level recombinant protein production in suspension cultured mammalian cells. Molecular Biotechnology 39, 141–153.

Lourdel, S., Paulais, M., Cluzeaud, F., Bens, M., Tanemoto, M., Kurachi, Y., Vandewalle, A., Teulon, J., 2002. An inward rectifier K(+) channel at the basolateral membrane of the mouse distal convoluted tubule: similarities with Kir4-Kir5.1 heteromeric channels. The Journal of Physiology 538, 391–404.

Lüscher, C., Slesinger, P.A., 2010. Emerging roles for G protein-gated inwardly rectifying potassium (GIRK) channels in health and disease. Nature Reviews Neuroscience 11, 301–315.

Macher, B.A., Yen, T.-Y., 2007. Proteins at membrane surfaces—a review of approaches. Molecular BioSystems 3, 705–713.

MacKinnon, R., 1995. Pore loops: an emerging theme in ion channel structure. Neuron 14, 889–892.

MacKinnon, R., 2003. Potassium channels. FEBS Letters 555, 62–65.

MacKinnon, R., Miller, C., 1989. Mutant potassium channels with altered binding of charybdotoxin, a pore-blocking peptide inhibitor. Science 245, 1382 LP – 1385.

Madeira, F., Pearce, M., Tivey, A.R.N., Basutkar, P., Lee, J., Edbali, O., Madhusoodanan, N., Kolesnikov, A., Lopez, R., 2022. Search and sequence analysis tools services from EMBL-EBI in 2022. Nucleic Acids Research 50, W276—W279.

Marmorstein, A.D., Finnemann, S.C., Bonilha, V.L., Rodriguez-Boulan, E., 1998. Morphogenesis of the retinal pigment epithelium: toward understanding retinal degenerative diseases. Annals of the New York Academy of Sciences 857, 1–12.

Martin, G.M., Yoshioka, C., Rex, E.A., Fay, J.F., Xie, Q., Whorton, M.R., Chen, J.Z., Shyng, S.-L., 2017. Cryo-EM structure of the ATP-sensitive potassium channel illuminates mechanisms of assembly and gating. eLife 6, e24149.

Mayer, M.P., Bukau, B., 2005. Hsp70 chaperones: cellular functions and molecular mechanism. Cellular and Molecular Life Sciences 62, 670–684.

McCloskey, C., Rada, C., Bailey, E., McCavera, S., van den Berg, H.A., Atia, J., Rand, D.A., Shmygol, A., Chan, Y.-W., Quenby, S., Brosens, J.J., Vatish, M., Zhang, J., Denton, J.S., Taggart, M.J., Kettleborough, C., Tickle, D., Jerman, J.,

Wright, P., Dale, T., Kanumilli, S., Trezise, D.J., Thornton, S., Brown, P., Catalano, R., Lin, N., England, S.K., Blanks, A.M., 2014. The inwardly rectifying K^+ channel Kir7.1 controls uterine excitability throughout pregnancy. EMBO Molecular Medicine 6, 1161–1174.

Meng, X.-Y., Liu, S., Cui, M., Zhou, R., Logothetis, D.E., 2016. The molecular mechanism of opening the helix bundle crossing (HBC) gate of a Kir channel. Scientific Reports 6, 29399.

Meng, X.-Y., Zhang, H.-X., Logothetis, D.E., Cui, M., 2012. The molecular mechanism by which PIP2 opens the intracellular G-loop gate of a Kir3.1 channel. Biophysical Journal 102, 2049–2059.

Mesirca, P., Marger, L., Toyoda, F., Rizzetto, R., Audoubert, M., Dubel, S., Torrente, A.G., DiFrancesco, M.L., Muller, J.C., Leoni, A.-L., Couette, B., Nargeot, J., Clapham, D.E., Wickman, K., Mangoni, M.E., 2013. The G-protein–gated K+ channel, IKACh, is required for regulation of pacemaker activity and recovery of resting heart rate after sympathetic stimulation. Journal of General Physiology 142, 113–126.

Min, L., Choe, L.H., Lee, K.H., 2015. Improved protease digestion conditions for membrane protein detection. Electrophoresis 36, 1690–1698.

Morales, E.S., Parcerisa, I.L., Ceccarelli, E.A., 2019. A novel method for removing contaminant Hsp70 molecular chaperones from recombinant proteins. Protein science : a Publication of the Protein Society 28, 800–807.

Mountjoy, K.G., Mortrud, M.T., Low, M.J., Simerly, R.B., Cone, R.D., 1994. Localization of the melanocortin-4 receptor (MC4-R) in neuroendocrine and autonomic control circuits in the brain. Molecular Endocrinology 8, 1298–1308.

Nakamura, N., Suzuki, Y., Sakuta, H., Ookata, K., Kawahara, K., Hirose, S., 1999. Inwardly rectifying K+ channel Kir7.1 is highly expressed in thyroid follicular cells, intestinal epithelial cells and choroid plexus epithelial cells: implication for a functional coupling with Na+,K+-ATPase. The Biochemical Journal 342 (Pt 2, 329–336.

Nishida, M., Cadene, M., Chait, B.T., MacKinnon, R., 2007. Crystal structure of a Kir3.1-prokaryotic Kir channel chimera. The EMBO Journal 26, 4005–4015.

Nishida, M., MacKinnon, R., 2002. Structural basis of inward rectification: cytoplasmic pore of the G protein-gated inward rectifier GIRK1 at 1.8 Å resolution. Cell 111, 957–965.

Niu, Y., Tao, X., Touhara, K.K., MacKinnon, R., 2020. Cryo-EM analysis of PIP2 regulation in mammalian GIRK channels. eLife 9, e60552.

Noble, A.J., Wei, H., Dandey, V.P., Zhang, Z., Tan, Y.Z., Potter, C.S., Carragher, B., 2018. Reducing effects of particle adsorption to the air–water interface in cryo-EM. Nature Methods 15, 793–795.

Nogales, E., Scheres, S.H.W., 2015. Cryo-EM: A unique tool for the visualization of macromolecular complexity. Molecular Cell 58, 677–689.

Nudelman, I., Glikin, D., Smolkin, B., Hainrichson, M., Belakhov, V., Baasov, T., 2010. Repairing faulty genes by aminoglycosides: Development of new derivatives of geneticin (G418) with enhanced suppression of diseases-causing nonsense mutations. Bioorganic & Medicinal Chemistry 18, 3735–3746.

O'Donnell, B.M., Mackie, T.D., Subramanya, A.R., Brodsky, J.L., 2017. Endoplasmic reticulum-associated degradation of the renal potassium channel, ROMK, leads to type II Bartter syndrome. The Journal of Biological Chemistry 292, 12813–12827.

O'M. B., J., 1982. Review: Ionic hydration in chemistry and biophysics. Journal of Solution Chemistry 11, 221–222.

Ogden, C.L., Carroll, M.D., Fryar, C.D., Flegal, K.M., 2015. Prevalence of obesity among adults and youth: United States, 2011-2014. NCHS Data Brief 1–8.

Ollmann, M.M., Wilson, B.D., Yang, Y.K., Kerns, J.A., Chen, Y., Gantz, I., Barsh, G.S., 1997. Antagonism of central melanocortin receptors in vitro and in vivo by agouti-related protein. Science (New York, N.Y.) 278, 135–138.

Orlova, E. V, Saibil, H.R., 2011. Structural analysis of macromolecular assemblies by electron microscopy. Chemical Reviews 111, 7710–7748.

Papanikolaou, M., Lewis, A., Butt, A.M., 2019. Glial and neuronal expression of the inward rectifying potassium channel Kir7.1 in the adult mouse brain. Journal of Anatomy 235, 984–996.

Pape, T., Wintermeyer, W., Rodnina, M. V, 2000. Conformational switch in the decoding region of 16S rRNA during aminoacyl-tRNA selection on the ribosome. Nature Structural Biology 7, 104–107.

Partiseti, M., Collura, V., Agnel, M., Culouscou, J.-M., Graham, D., 1998. Cloning and characterization of a novel human inwardly rectifying potassium channel predominantly expressed in small intestine. FEBS Letters 434, 171–176.

Passmore, L.A., Russo, C.J., 2016. Specimen reparation for high-resolution cryo-

EM. Methods Enzymology 579, 51–86.

Pattnaik, B.R., Shahi, P.K., Marino, M.J., Liu, X., York, N., Brar, S., Chiang, J., Pillers, D.-A.M., Traboulsi, E.I., 2015. A novel KCNJ13 nonsense mutation and loss of Kir7.1 channel function causes Leber Congenital Amaurosis (LCA16). Human Mutation 36, 720–727.

Pattnaik, B.R., Tokarz, S., Asuma, M.P., Schroeder, T., Sharma, A., Mitchell, J.C., Edwards, A.O., Pillers, D.-A.M., 2013. Snowflake vitreoretinal degeneration (SVD) mutation R162W provides new insights into Kir7.1 ion channel structure and function. PLOS ONE 8, e71744.

Pegan, S., Arrabit, C., Zhou, W., Kwiatkowski, W., Collins, A., Slesinger, P.A., Choe, S., 2005. Cytoplasmic domain structures of Kir2.1 and Kir3.1 show sites for modulating gating and rectification. Nature Neuroscience 8, 279–287.

Penczek, P.A., 2010. Resolution measures in molecular electron microscopy. Methods in Enzymology 482, 73–100.

Perez-Roustit, S., Marquette, V., Bocquet, B., Kaplan, J., Perrault, I., Meunier, I., Hamel, C.P., 2017. Leber congenital amaurosis with large retinal pigment clumps caused by compound heterozygous mutations KCNJ13. Retinal Cases & Brief Reports 11, 221–226.

Peters, M., Ermert, S., Jeck, N., Derst, C., Pechmann, U., Weber, S., Schlingmann, K.P., Seyberth, H.W., Waldegger, S., Konrad, M., 2003. Classification and rescue of ROMK mutations underlying hyperprostaglandin E syndrome/antenatal Bartter syndrome. Kidney International 64, 923–932.

Pettersen, E.F., Goddard, T.D., Huang, C.C., Couch, G.S., Greenblatt, D.M., Meng, E.C., Ferrin, T.E., 2004. UCSF Chimera--a visualization system for exploratory research and analysis. Journal of Computational Chemistry 25, 1605–1612.

Pettersen, E.F., Goddard, T.D., Huang, C.C., Meng, E.C., Couch, G.S., Croll, T.I., Morris, J.H., Ferrin, T.E., 2021. UCSF ChimeraX: Structure visualization for researchers, educators, and developers. Protein Science : a Publication of the Protein Society 30, 70–82.

Phillips, L.R., Enkvetchakul, D., Nichols, C.G., 2003. Gating dependence of inner pore access in inward rectifier K+ channels. Neuron 37, 953–962.

Pini, J., Giuliano, S., Matonti, J., Gannoun, L., Simkin, D., Rouleau, M., Bendahhou, S., 2018. Osteogenic and chondrogenic master genes expression is dependent on the Kir2.1 potassium channel through the bone morphogenetic protein pathway.

Journal of Bone and Mineral Research : The Official Journal of the American Society for Bone and Mineral Research 33, 1826–1841.

Prisant, M.G., Williams, C.J., Chen, V.B., Richardson, J.S., Richardson, D.C., 2020. New tools in MolProbity validation: CaBLAM for CryoEM backbone, UnDowser to rethink “waters,” and NGL Viewer to recapture online 3D graphics. Protein Science 29, 315–329.

Punjani, A., Rubinstein, J.L., Fleet, D.J., Brubaker, M.A., 2017. cryoSPARC: algorithms for rapid unsupervised cryo-EM structure determination. Nature Methods 14, 290–296.

Punjani, A., Zhang, H., Fleet, D.J., 2020. Non-uniform refinement: adaptive regularization improves single-particle cryo-EM reconstruction. Nature Methods 17, 1214–1221.

Ramsden, C.M., Nommiste, B., Lane, A.R., Carr, A.-J.F., Powner, M.B., Smart, M.J.K., Chen, L.L., Muthiah, M.N., Webster, A.R., Moore, A.T., Cheetham, M.E., Da Cruz, L., Coffey, P.J., 2017. Rescue of the MERTK phagocytic defect in a human iPSC disease model using translational readthrough inducing drugs. Scientific Reports 7.

Rifkin, R.A., Moss, S.J., Slesinger, P.A., 2017. G Protein-gated potassium channels: a link to drug addiction. Trends in Pharmacological Sciences 38, 378–392.

Rohács, T., Lopes, C.M.B., Jin, T., Ramdya, P.P., Molnár, Z., Logothetis, D.E., 2003. Specificity of activation by phosphoinositides determines lipid regulation of Kir channels. Proceedings of the National Academy of Sciences 100, 745–750.

Rosenthal, P.B., Henderson, R., 2003. Optimal determination of particle orientation, absolute hand, and contrast loss in single-particle electron cryomicroscopy. Journal of Molecular Biology 333, 721–745.

Roux, B., MacKinnon, R., 1999. The cavity and pore helices in the KcsA K^+ channel: electrostatic stabilization of monovalent cations. Science 285, 100 LP – 102.

Russo, C.J., Passmore, L.A., 2016. Ultrastable gold substrates: Properties of a support for high-resolution electron cryomicroscopy of biological specimens. Journal of Structural Biology 193, 33–44.

Sadja, R., Smadja, K., Alagem, N., Reuveny, E., 2001. Coupling Gβγ-dependent activation to channel opening via pore elements in inwardly rectifying

potassium channels. Neuron 29, 669–680.

Sanchez-Garcia, R., Gomez-Blanco, J., Cuervo, A., Carazo, J.M., Sorzano, C.O.S., Vargas, J., 2021. DeepEMhancer: a deep learning solution for cryo-EM volume post-processing. Communications Biology 4, 874.

Scheres, S.H.W., 2012. RELION: Implementation of a Bayesian approach to cryo-EM structure determination. Journal of Structural Biology 180, 519–530.

Scheres, S.H.W., 2014. Beam-induced motion correction for sub-megadalton cryo-EM particles. eLife 3, e03665.

Scheres, S.H.W., Chen, S., 2012. Prevention of overfitting in cryo-EM structure determination. Nature Methods 9, 853–854.

Schlegel, S., Hjelm, A., Baumgarten, T., Vikström, D., de Gier, J.-W., 2014. Bacterial-based membrane protein production. Biochimica et Biophysica Acta (BBA) - Molecular Cell Research 1843, 1739–1749.

Scholl, U.I., Choi, M., Liu, T., Ramaekers, V.T., Häusler, M.G., Grimmer, J., Tobe, S.W., Farhi, A., Nelson-Williams, C., Lifton, R.P., 2009. Seizures, sensorineural deafness, ataxia, mental retardation, and electrolyte imbalance (SeSAME syndrome) caused by mutations in KCNJ10. Proceedings of the National Academy of Sciences of the United States of America 106, 5842–5847.

Schwarz, N., Carr, A.-J., Lane, A., Moeller, F., Chen, L.L., Aguilà, M., Nommiste, B., Muthiah, M.N., Kanuga, N., Wolfrum, U., Nagel-Wolfrum, K., da Cruz, L., Coffey, P.J., Cheetham, M.E., Hardcastle, A.J., 2015. Translational read-through of the RP2 Arg120stop mutation in patient iPSC-derived retinal pigment epithelium cells. Human Molecular Genetics 24, 972–986.

Sergouniotis, P.I., Davidson, A.E., Mackay, D.S., Li, Z., Yang, X., Plagnol, V., Moore, A.T., Webster, A.R., 2011. Recessive mutations in KCNJ13, encoding an inwardly rectifying potassium channel subunit, cause leber congenital amaurosis. The American Journal of Human Genetics 89, 183–190.

Shahi, P.K., Hermans, D., Sinha, D., Brar, S., Moulton, H., Stulo, S., Borys, K.D., Capowski, E., Pillers, D.-A.M., Gamm, D.M., Pattnaik, B.R., 2019. Gene augmentation and readthrough rescue channelopathy in an iPSC-RPE model of congenital blindness. American Journal of Human Genetics 104, 310–318.

Shieh, C.-C., Coghlan, M., Sullivan, J.P., Gopalakrishnan, M., 2000. Potassium channels: molecular defects, diseases, and therapeutic opportunities.

Pharmacological Reviews 52, 557 LP – 594.

Sigworth, F.J., 2016. Principles of cryo-EM single-particle image processing. Microscopy (Oxford, England) 65, 57–67.

Smart, O.S., Neduvelil, J.G., Wang, X., Wallace, B.A., Sansom, M.S.P., 1996. HOLE: A program for the analysis of the pore dimensions of ion channel structural models. Journal of Molecular Graphics 14, 354–360.

Strauss, O., 2005. The retinal pigment epithelium in visual function. Physiological Reviews 85, 845–881.

Tao, X., Avalos, J.L., Chen, J., MacKinnon, R., 2009. Crystal structure of the eukaryotic strong inward-rectifier K^+ channel Kir2.2 at 3.1 Å resolution. Science 326, 1668–1674.

Tateno, T., Nakamura, N., Hirata, Y., Hirose, S., 2006. Role of C-terminus of Kir7.1 potassium channel in cell-surface expression. Cell Biology International 30, 270–277.

Tempel, B.L., Papazian, D.M., Schwarz, T.L., Jan, Y.N., Jan, L.Y., 1987. Sequence of a probable potassium channel component encoded at Shaker locus of Drosophila. Science 237, 770 LP – 775.

Thumann, G., 2001. Development and cellular functions of the iris pigment epithelium. Survey of Ophthalmology 45, 345–354.

Toms, M., Dubis, A.M., Lim, W.S., Webster, A.R., Gorin, M.B., Moosajee, M., 2019. Missense variants in the conserved transmembrane M2 protein domain of KCNJ13 associated with retinovascular changes in humans and zebrafish. Experimental Eye Research 189, 107852.

Vera, E., Cornejo, I., Niemeyer, M.I., Sepúlveda, F. V, Cid, L.P., 2021. Altered phosphatidylinositol regulation of mutant inwardly rectifying K+ Kir7.1 channels associated with inherited retinal degeneration disease. The Journal of Physiology 599, 593–608.

Villarroel, A., Herlitze, S., Koenen, M., Sakmann, B., 1991. Location of a threonine residue in the alpha-subunit M2 transmembrane segment that determines the ion flow through the acetylcholine receptor channel. Proceedings Biological sciences 243, 69–74.

Waterhouse, A., Bertoni, M., Bienert, S., Studer, G., Tauriello, G., Gumienny, R., Heer, F.T., de Beer, T.A.P., Rempfer, C., Bordoli, L., Lepore, R., Schwede, T., 2018. SWISS-MODEL: homology modelling of protein structures and

complexes. Nucleic Acids Research 46, W296–W303.

Welling, P.A., Ho, K., 2009. A comprehensive guide to the ROMK potassium channel: form and function in health and disease. American Journal of Physiology. Renal Physiology 297, F849-63.

Whorton, M.R., MacKinnon, R., 2011. Crystal structure of the mammalian GIRK2 K+ channel and gating regulation by G proteins, PIP2, and sodium. Cell 147, 199–208.

Wickman, K., Nemec, J., Gendler, S.J., Clapham, D.E., 1998. Abnormal heart rate regulation in GIRK4 knockout mice. Neuron 20, 103–114.

Williams, C.J., Headd, J.J., Moriarty, N.W., Prisant, M.G., Videau, L.L., Deis, L.N., Verma, V., Keedy, D.A., Hintze, B.J., Chen, V.B., Jain, S., Lewis, S.M., Arendall, W.B. 3rd, Snoeyink, J., Adams, P.D., Lovell, S.C., Richardson, J.S., Richardson, D.C., 2018. MolProbity: More and better reference data for improved all-atom structure validation. Protein Science : a Publication of the Protein Society 27, 293–315.

Yang, D., Pan, A., Swaminathan, A., Kumar, G., Hughes, B.A., 2003. Expression and localization of the inwardly rectifying potassium channel Kir7.1 in native bovine retinal pigment epithelium. Investigative Ophthalmology & Visual Science 44, 3178–3185.

Yang, D., Zhang, X., Hughes, B.A., 2008. Expression of inwardly rectifying potassium channel subunits in native human retinal pigment epithelium. Experimental Eye Research 87, 176–183.

Zhang, W., Zhang, X., Wang, H., Sharma, A.K., Edwards, A.O., Hughes, B.A., 2013. Characterization of the R162W Kir7.1 mutation associated with snowflake vitreoretinopathy. American Journal of Physiology. Cell Physiology 304, 440–449.

Zhao, C., MacKinnon, R., 2021. Molecular structure of an open human K_{ATP} channel. Proceedings of the National Academy of Sciences 118, e2112267118.

Zhou, Y., Morais-Cabral, J.H., Kaufman, A., MacKinnon, R., 2001. Chemistry of ion coordination and hydration revealed by a K+ channel–Fab complex at 2.0 Å resolution. Nature 414, 43–48.

Zivanov, J., Nakane, T., Forsberg, B.O., Kimanius, D., Hagen, W.J.H., Lindahl, E., Scheres, S.H.W., 2018. New tools for automated high-resolution cryo-EM structure determination in RELION-3. eLife 7, e42166.

Zubcevic, L., Bavro, V.N., Muniz, J.R.C., Schmidt, M.R., Wang, S., De Zorzi, R., Venien-Bryan, C., Sansom, M.S.P., Nichols, C.G., Tucker, S.J., 2014. Control of KirBac3.1 potassium channel gating at the interface between cytoplasmic domains. The Journal of Biological Chemistry 289, 143–151.

Appendix

	Apo Kir7.1	Kir7.1-PIP_2	Kir7.1-R162W
Data collection and processing			
Magnification	130,000X	130,000X	130,000X
Voltage (kV)	300	300	300
Electron exposure (e^-/Å)	31.9	31.9	31.89
Defocus range (μM)	1.2-2.7	1.2-2.7	1.2-2.4
Pixel size (Å)	0.65	0.65	0.65
symmetry imposed	C4	C4	C4
Initial particle images (no.)	5, 871, 876	8, 821, 241	3, 093, 422
Final particle images (no.)	382, 328	556, 510	140, 275
Map resolution (Å)	3.54	3.29	3.51
FSC threshold	0.143	0.143	0.143
Refinement			
Map sharpening *B* factor ($Å^2$)	-206.6	-194	-177.4
Model composition			
Non-hydrogen atoms	17098	9264	16704
Protein residues	1156	1196	1132
ligands	2	8	4
B factors ($Å^2$)			
Protein	52.82	82.73	26.06
Ligand	39.45	163.42	24.94
R.m.s. deviations			
Bond lengths (Å)	0.003	0.003	0.003
Bond angles (°)	0.558	0.517	0.527
Validation			
MolProbity score	1.52	1.78	1.91
Clashscore	5.62	7.92	9.35
Poor rotamers (%)	0	0.73	0
Ramachandran plot			
Favored (%)	0	0.34	0
Allowed (%)	3.36	4.75	6.32
Disallowed (%)	96.64	94.92	93.68
Model			
CC_mask	0.76	0.79	0.76
CC_volume	0.73	0.77	0.71
Mean CC for ligands	0.74	0.61	0.82

Appendix 1. Model validation statistics. Molprobity validation statistics from Phenix for each model.